ANALYSIS OF CRACK INITIATION AND PROPAGATION IN SOLID ROCKET MOTOR NOZZLE THROATS

A THESIS SUBMITTED TO
THE GRADUATE SCHOOL OF NATURAL AND APPLIED SCIENCES
OF
MIDDLE EAST TECHNICAL UNIVERSITY

BY

BARIŞ NİGAR

IN PARTIAL FULFILLMENT OF THE REQUIREMENTS
FOR
THE DEGREE OF MASTER OF SCIENCE
IN
MECHANICAL ENGINEERING

NOVEMBER 2019

Approval of the thesis:

ANALYSIS OF CRACK INITIATION AND PROPAGATION IN SOLID ROCKET MOTOR NOZZLE THROATS

submitted by **BARIŞ NİGAR** in partial fulfillment of the requirements for the degree of **Master of Science in Mechanical Engineering Department, Middle East Technical University** by,

Prof. Dr. Halil Kalıpçılar
Dean, Graduate School of **Natural and Applied Sciences**

Prof. Dr. M. A. Sahir Arıkan
Head of Department, **Mechanical Engineering**

Assist. Prof. Dr. Sezer Özerinç
Supervisor, **Mechanical Engineering, METU**

Assoc. Prof. Dr. Demirkan Çöker
Co-Supervisor, **Aerospace Engineering, METU**

Examining Committee Members:

Prof. Dr. Suat Kadıoğlu
Mechanical Engineering, METU

Assist. Prof. Dr. Sezer Özerinç
Mechanical Engineering, METU

Assoc. Prof. Dr. Hüsnü Dal
Mechanical Engineering, METU

Assoc. Prof. Dr. Demirkan Çöker
Aerospace Engineering, METU

Assist. Prof. Dr. Ömer Music
Mechanical Engineering, TED University

Date: 28.11.2019

I hereby declare that all information in this document has been obtained and presented in accordance with academic rules and ethical conduct. I also declare that, as required by these rules and conduct, I have fully cited and referenced all material and results that are not original to this work.

Name, Surname: Barış Nigar

Signature:

ABSTRACT

ANALYSIS OF CRACK INITIATION AND PROPAGATION IN SOLID ROCKET MOTOR NOZZLE THROATS

Nigar, Barış
Master of Science, Mechanical Engineering
Supervisor: Assist. Prof. Dr. Sezer Özerinç
Co-Supervisor: Assoc. Prof. Dr. Demirkan Çöker

November 2019, 89 pages

Graphite is a widely used material in high temperature structural applications due to its high melting point and its mechanical strength and integrity at elevated temperatures. However, rocket nozzles made of graphite are subjected to very high temperatures and pressures that cause cracking and eventual failure. This thesis investigates the reasons of failure and explores design alternatives to overcome this problem. The experimental part of the thesis includes compression tests, tensile tests and fracture toughness tests on Mersen-2020 graphite. Compression and tensile tests showed a bimodular response. Fracture toughness tests involved Single Edge Notch Bend (SENB) specimens and demonstrated the brittle nature of graphite. Based on experimentally measured materials behavior of graphite, a two-dimensional finite element model investigated the crack propagation behavior. The analyses were done in three steps. The first step was the computational fluid dynamics analysis of the flow through the nozzle. Using the results of this step, second step predicted the temperature variations within the nozzle. The final and most extensive part of the modeling consisted of Extended Finite Element Method applied on the nozzle geometry experiencing thermal stresses based on the analysis in the second step. The results show that the cracks are mostly mode II cracks induced by the compressive stresses next to the flow surface of the nozzle. Within only 5 seconds, these cracks result in graphite pieces breaking off, which adversely affects the flow dynamics of the nozzle. The change in the flow directly impacts the desired thrust force and results in an unreliable performance. As the final part of the analysis, the thesis considered some alternative nozzle designs that utilize a segmented geometry consisting of individual graphite parts. Several geometries were analyzed for their crack propagation behavior. The results show that careful segmentation of the nozzle relieves the stresses in critical regions and delay the failure. The thesis provides insight into the mechanisms of failure in graphite rocket nozzles and presents a design approach for superior and more reliable performance.

Keywords: Graphite, Fracture, Crack propagation, Extended finite element analysis, Rocket nozzle

ÖZ

KATI YAKITLI ROKET MOTOR BOĞAZLARINDA ÇATLAK OLUŞUMU VE İLERLEMESİ ANALİZİ

Nigar, Barış
Yüksek Lisans, Makina Mühendisliği
Tez Danışmanı: Dr. Öğr. Üyesi Sezer Özerinç
Ortak Tez Danışmanı: Doç. Dr. Demirkan Çöker

Kasım 2019, 89 sayfa

Grafit, nükleer reaktörler ve roket lüleleri gibi yüksek sıcaklık uygulamalarında yaygın olarak kullanılan bir malzemedir. Bu uygulamalar açısından grafitin temel avantajları yüksek erime noktası ve yüksek sıcaklıklarda mekanik mukavemeti ve bütünlüğü koruyabilmesidir. Grafitten yapılmış lüleler, çok yüksek sıcaklıklara ve basınçlara maruz kaldığından çatlak oluşumu ve buna bağlı hasar yaygın olarak görülmektedir. Bu tezin amacı, söz konusu çatlak oluşumu ve parça kopmasının nedenlerini araştırmak ve bu sorunun üstesinden gelmek için tasarım alternatiflerini incelemektedir. Tezin deneysel kısmı Mersen-2020 grafit üzerinde gerçekleştirilen basma testleri, çekme testleri ve kırılma tokluğu testlerini içermektedir. Basma ve çekme testlerinde bimodüler davranış görülmüştür. Kırılma tokluğu testleri Tek Kenar Çentik Bükme (TKÇB) numuneleri ile yapılmıştır ve grafitin kırılgan yapıda olduğu doğrulanmıştır. Grafitin deneysel olarak ölçülen malzeme özelliklerine dayanarak, iki boyutlu bir sonlu elemanlar modeli ile çatlak ilerleme davranışı incelenmiştir. Analizler üç adımda yapılmıştır. İlk adım, lüledeki akışın hesaplamalı akışkanlar dinamiği ile analizidir. Bu adımın sonuçlarını kullanarak, ikinci adımda lüle içindeki sıcaklık değişimleri öngörülmüştür. Modellemenin son ve en kapsamlı kısmında, ikinci aşamada elde edilen sıcaklık değişimlerinin yol açtığı termal gerilimler ve buna bağlı çatlak oluşumu ve ilerlemesi, Genişletilmiş Sonlu Elemanlar Yöntemi ile ele alınmıştır. Analiz sonucunda, çatlakların, lülenin akış yüzeyine bitişik bölgedeki sıkıştırma gerilmelerinin neden olduğu mod II çatlaklar olduğu belirlenmiştir. Sadece 5 saniye içerisinde bu çatlaklar grafit parçalarının kopmasına neden olmakta ve lülenin akış dinamiklerini olumsuz etkilemektedir. Akıştaki değişim, hedeflenen itme kuvvetini doğrudan etkilemekte ve güvenilir olmayan bir performansa yol açmaktadır. Analizler kapsamında son olarak çok sayıda grafit parçasından oluşan tasarım alternatifleri ele alınmıştır. Analiz sonuçları, lülenin küçük parçalara bölünmesinin kritik bölgelerdeki gerilmeleri azalttığını ve lülenin hasarını geciktirdiğini göstermektedir. Sonuç olarak tez, grafit roket lülelerdeki hasar oluşumu mekanizmaları hakkında önemli bilgiler sunmuş ve daha güvenilir ve yüksek performanslı lüleler için bir tasarım yaklaşımı ortaya koymuştur.

Anahtar Kelimeler: Grafit, Kırılma, Çatlak ilerlemesi, Genişletilmiş sonlu elemanlar analizi, Roket lüleleri

To My Family and My Wife

ACKNOWLEDGEMENTS

I would like to thank my advisor Assist. Prof. Dr. Sezer Özerinç of Mechanical Engineering at METU and my co-advisor Assoc. Prof. Dr. Demirkan Çöker of Aerospace Engineering at METU. I will be always deeply thankful to them for their continuous support, and professional guidance throughout the process of this thesis.

I also would like to thank to my colleague Serhan Dönmez for his technical support during this study, and Burçin Kaygusuz for her valuable contributions.

I am grateful to lead engineers Dr. Levent Ünlüsoy and Funda Aksu Denli for their encouragement and patience when I needed most.

I would like to thank ROKETSAN for its support in this study.

Finally, I want to express my deepest gratitude to my parents, brothers and my wife for their endless support and continuous encouragement from the beginning to the end of this study. This study would not be possible without them. Thank you so much.

TABLE OF CONTENTS

ABSTRACT v
ÖZ vii
ACKNOWLEDGEMENTS x
TABLE OF CONTENTS xi
LIST OF TABLES xv
LIST OF FIGURES xvi

CHAPTERS

1. INTRODUCTION 1
  1.1. Solid Propellant Rocket Motors 1
  1.2. Materials used in Nozzles 3
  1.3. Reasons of Failure of Rocket Nozzles 3
  1.4. Previous Work on the Failure of Graphite Nozzles 4
  1.5. Problem Definition 12
  1.6. Proposed Methods and Models 12
2. EXPERIMENTAL CHARACTERIZATION OF GRAPHITE 13
  2.1. Introduction 13
  2.2. Thermal Tests 13
  2.3. Mechanical Tests 16
    2.3.1. Tensile Tests 16
    2.3.2. Compression Tests 18
    2.3.3. Fracture Toughness Tests 22

3. MODELING OF CRACK PROPAGATION USING EXTENDED FINITE ELEMENT METHOD 33

3.1. Linear Elastic Fracture Mechanics (LEFM) 33

3.1.1. Fracture Modes 33

3.1.2. Stress Intensity Factor 34

3.1.3. Fracture Toughness 34

3.2. Extended Finite Element Method (XFEM) 35

3.2.1. Enrichment 36

3.2.2. Cohesive Segment Method and Phantom Nodes 39

3.2.3. XFEM Based Traction-Separation Cohesive Behavior 40

3.2.3.1. Damage Initiation 41

3.2.3.2. Level Set Method 41

3.3. Verification of the Modeling Approach 42

3.3.1. The SENB Specimen Three Point Bending Test 42

3.3.1.1. Problem Description 42

3.3.1.2. Geometry and Model 42

3.3.1.3. Material 44

3.3.1.4. Results and Discussion 48

3.3.2. Crack Propagation in an Asymmetrically Notched Beam 50

3.3.2.1. Problem Description 50

3.3.2.2. Geometry and Model 50

3.3.2.3. Results and Discussion 52

4. CRACK INITIATION AND PROPAGATION ANALYSIS OF A GRAPHITE THROAT 53

4.1. Supporting Analysis: CFD and Heat Transfer Analysis of the Nozzle 54
  4.1.1. CFD Analysis 54
    4.1.1.1. Methodology 54
    4.1.1.2. Geometry and Modeling 54
    4.1.1.3. Results and Discussion 56
  4.1.2. Finite Element Transient Heat Transfer Analysis 57
    4.1.2.1. Methodology 57
    4.1.2.2. Geometry and Modeling 57
    4.1.2.3. Results and Discussion 59
4.2. XFEM Analysis of Crack Initiation and Propagation 61
    4.2.1.1. Methodology 61
    4.2.1.2. Geometry and Modeling 61
4.3. Results and Discussions 67
  4.3.1. Analysis of the Monolithic Design 68
    4.3.1.1. Monolithic Design: Case I - Bonded Interface 68
    4.3.1.2. Monolithic Design: Case II - Contact Interface 70
  4.3.2. Partitioned Designs 72
    4.3.2.1. Design-1 Overview 72
    4.3.2.2. Design-1 with No Gap 73
    4.3.2.3. Design-1 with Gap 75
  4.3.3. Design-2 Overview 76
    4.3.3.1. Design-2: No Gap 76
    4.3.3.2. Design-2: with Gap 78
5. CONCLUSIONS AND FUTURE WORK 81

5.1. Conclusions 81

5.2. Future Work 82

REFERENCES 85

LIST OF TABLES

TABLES

Table 2.1. Compression Test Specimen Type and Size 18

Table 2.2. Coefficients of g(a/W). 25

Table 2.3. Linearization constants for tests. 26

Table 2.4. Mean and standard deviation values of K_{IC}, G_{IC}, J_{IC} of test results. 28

Table 2.5. Mean and standard deviation values of K_{IC}, G_{IC}, J_{IC} in Bhushan's study. 28

Table 4.1. Input parameters of flow analysis. 55

Table 4.2. Thermal properties of graphite as a function of temperature. 58

Table 4.3. Thermal properties of Silica Phenolic as a function of temperature, table taken from [9]. 58

LIST OF FIGURES

FIGURES

Figure 1.1. Flow chart of design sequence, figure taken from [2]............................. 2
Figure 2.1. Change of specific heat of graphite with increasing temperature........... 14
Figure 2.2. Change of coefficient of thermal expansion of graphite with increasing temperature.. 15
Figure 2.3. Change of thermal conductivity of graphite with increasing temperature. 15
Figure 2.4. Change of thermal diffusivity of graphite with increasing temperature. 16
Figure 2.5. Tension test stress-strain curves for longitudinal and transverse directions at room temperature.. 17
Figure 2.6. Linearized tension test stress-strain curves of longitudinal and transverse directions.. 18
Figure 2.7. Stress-strain curves of loaded specimens.. 19
Figure 2.8. Elastic modulus- strain (%) graphs of compression test specimens. 20
Figure 2.9. Behavior of compressive strength against temperature, figure taken from [27].. 20
Figure 2.10. Linear regression results of compressive stress-strain data of four compression test specimens.. 21
Figure 2.11. A photograph of fracture toughness test setup................................... 22
Figure 2.12. Load-displacement curves of fracture toughness tests........................ 23
Figure 2.13. A microscope image of cracked specimen. 24
Figure 2.14. The crack propagation on SENB specimen in fracture toughness test. 24
Figure 2.15. Critical stress intensity factors of fracture toughness tests and comparison with Bhushan's results. 26
Figure 2.16. Linearized load-displacement curves.. 27
Figure 2.17 Compliance-displacement values of fracture toughness test specimens. 28

Figure 2.18. Crack extension-displacement values of fracture toughness test specimens. 29
Figure 2.19. Strain energy release rate (SERR)-displacement values of fracture toughness test specimens. 29
Figure 2.20. Strain energy release rate (SERR)-crack extension values of fracture toughness test specimens. 30
Figure 2.21. Critical J-Integral and SERR comparison, figure taken from [22]. 31
Figure 2.22. Critical J-Integral and SERR comparison. 31
Figure 3.1. Schematic view of fracture modes a) Mode I, b) Mode II, c) Mode III, figure taken from [24]. 33
Figure 3.2. Schematic view of fracture toughness variation with thickness, figure taken from [5]. 35
Figure 3.3. Schematic view of initiation of crack between elements, figure taken from [36]. 36
Figure 3.4. Schematic view of enrichment of nodes, figure taken from [36]. 38
Figure 3.5 Illisturation of polar and n-t coordinates for a smooth crack, figure taken from [36]. 39
Figure 3.6. Schematic view of phantom node principle, figure taken from [36]. 40
Figure 3.7. Representation of a nonplanar crack in three dimensions by two orthogonal surface, figure taken from [36]. 42
Figure 3.8. Free body diagram of the SENB specimen geometry in D7779 standard, figure taken from [29]. 43
Figure 3.9. Time-displacement curve applied to FEA model. 43
Figure 3.10. The FEA model illustration. 44
Figure 3.11. Flow chart for evaluation of stress fields, figure taken from [22]. 45
Figure 3.12. Process of crack initiation criterion in UDMGINI subroutine. 46
Figure 3.13. Mohr-circle representation of Mohr-Coulomb failure criterion. 47
Figure 3.14. Stress field of SENB specimen in FEA model during loading. 49
Figure 3.15. The crack propagation on SENB specimen in FEA model during loading. 49

Figure 3.16. Load-displacement curves of FEA model and experiment. 50
Figure 3.17. Geometry of asymmetrically notched beam, figure taken from [37]. ... 51
Figure 3.18. The FEA model with boundary and loading conditions. 51
Figure 3.19. The crack propagation on asymmetrically notched specimen. 52
Figure 4.1. Schematic view of analysis procedure of rocket motor nozzle analysis. 54
Figure 4.2. Flow field mesh structure of solid propellant rocket nozzle. 55
Figure 4.3 Pressure distribution through normalized length of flow surface through "t". 56
Figure 4.4. Plane 55 element used in transient heat transfer analysis in APDL, figure taken from [42]. 59
Figure 4.5. Meshed geometry for heat transfer analysis. 59
Figure 4.6. Temperature contours for a) 1 second b) 5 seconds c) 10 seconds d)14 seconds. 60
Figure 4.7. Temperature on surface t and surface s for time frames of 1 second, 5 seconds, 10 seconds, and 14 seconds. 60
Figure 4.8. a) Isometric and b) axisymmetric view of rocket nozzle throat in thermomechanical finite element model. 62
Figure 4.9. Illustration of elastic modulus change of ATJ graphite with rising temperature, figure taken from [26]. 63
Figure 4.10. Schematic view of the boundary conditions of the model. The arrows indicate the magnitude of pressure over the nozzle surface. 64
Figure 4.11. Schematic view of the axisymmetric model showing the details of the mesh. 65
Figure 4.12. Mesh convergence graph of thermomechanical model. 65
Figure 4.13 Illustration of monolithic design model according to interface definition between throat and isolator jacket. 66
Figure 4.14. Friction coefficient comparison against temperature, figure taken from [16]. 67
Figure 4.15. Illustration of thermal expansion of throat in radial direction along normalized length of depth. 68

Figure 4.16. Contour view of principal stress distribution and detail crack view of bonded joint model from different regions on throat part. 69
Figure 4.17. Contour view of principal stress distribution and detail crack view of contact joint model from different regions on throat part (70% of fully converged solution). 70
Figure 4.18. Contour view of principal stress distribution and detail crack view of contact interface model from different regions on throat part (fully converged solution). 71
Figure 4.19. a) A crack propagates parallel to surface (B) and a crack propagates downward to railway (A). b) Catastrophic failure of railway due to break off a large piece of railway, figure taken from [46]. 72
Figure 4.20. Nozzle with circumferential crack in graphite section and segmenting graphite throat into rings to prevent thermal cracks, figure taken from [2]. 72
Figure 4.21 Illustration of design-1 throat model according to gap size between segments of throat parts 73
Figure 4.22. Principal stress distribution and detailed crack view of design-1 with no gap. 74
Figure 4.23. Principal stress distribution and detailed crack view of straight-partitioned model with gap. 75
Figure 4.24. Illustration of design-2 throat model according to gap size between segments of throat parts. 76
Figure 4.25. Principal stress distribution and detailed crack view of design-2 model with no gap. 77
Figure 4.26. Principal stress distribution and detailed crack view of design-2 model with gap. 78

CHAPTER 1

INTRODUCTION

In rocket applications, all sub-systems are designed for a single operation in most cases. The ultimate mission of all sub-systems is to make aircraft delivered the payload to the intended location. Hence, in all auxiliary systems, simpler and cheaper parts are preferred as long as the integrity of the system is maintained. One of these sub-systems is the propulsion system which provides the required thrust force for the aircraft until it reaches to the desired position.

In missile applications, propulsion systems are called rocket motors, mainly consisting of a motor case, an oxidizer, a propellant, and a nozzle with support structures including an insulator and structural parts. Ignition of the fuel by the help of oxidizer produces sufficient thrust force to the rocket by the expansion of the exhaust products in a convergent-divergent nozzle.

Rocket motors are generally classified according to the fuel and oxidizer type. In the literature, main categories include liquid propellants, solid propellants and solid-liquid (hybrid) propellants [1]. In this study, a solid-propellant rocket motor nozzle is investigated.

1.1. Solid Propellant Rocket Motors

In a solid propellant rocket motor, highly pressurized combustion product gases provide thrust force to the rocket by converting the chemical energy into kinetic energy, through the ignition of the solid fuel in the combustion chamber. The exhaust gases are discharged through a converging-diverging nozzle so that the flow generated by the aerodynamic nozzle surface provides the required performance needed for the predetermined flight range. Because of its critical role, nozzle design has a high priority for rocket motor research. A NASA Technical Report [2], discusses the main considerations for the design of a nozzle in detail. The design sequence includes the co-operation of many disciplines towards a final product that can successfully complete the mission. Figure 1.1 shows a flowchart of the nozzle design sequence [2].

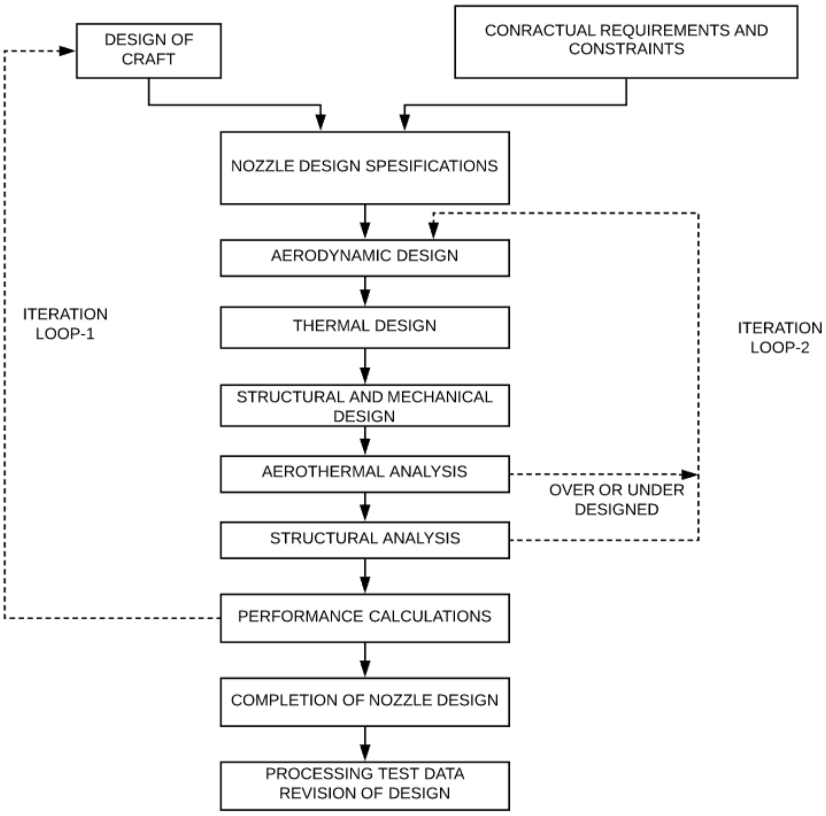

Figure 1.1. Flow chart of design sequence, figure taken from [2].

In the flowchart, determination of the design specifications is the first step. According to those specifications, geometrical design and material selection are considered. In the design procedure, three phases, which are aerodynamic design, thermal design, and structural design, are completed. Once the nozzle is designed according to requirements including envelope restrictions, cost and weight; an analyst uses examines all critical parts for their accuracy and function. Among these, structural analysis is check to make sure that the craft will keep its structural integrity during the mission.

Solid propellant rocket motor nozzles operate in harsh environments due to the high thermal and pressure loads. As a result, nozzle throats suffer from cracking during combustion. Another NASA technical report [3] mentions that nozzle throats made of a range of different materials were damaged due to erosion and/or cracking.

This thesis will investigate the structural analysis of the nozzle. Analyses follow the road map provided by Lapp and Quesada [4] which consists of aerodynamic analysis, thermal analysis, thermomechanical analysis, and mechanical analysis.

1.2. Materials used in Nozzles

Material selection for the solid rocket motor nozzle is critical. To preserve structural integrity, six different materials are commonly preferred as throat material in the literature [2]. These are reinforced Plastics, polycrystalline graphite, pyrolytic graphite, refractory metals, carbon-carbon composites, and ceramics. Among these materials the first four materials are commonly used in rocket applications, whereas carbon composites are preferred for high-level applications. Ceramics are less common as they are more vulnerable to thermal shock.

Reinforced plastics are generally used in thermal liners and inserts. They are strong and temperature resistant materials. On the other hand, polycrystalline graphite is a material available in bulk form, and provides low cost, high erosion resistance and it tends to get tougher with increasing temperature. Since it is relatively low strength compared to reinforced plastics and refractory metals, it is not used in advanced applications.

For harsh conditions, throat insert can also be made of graphite pieces and washers made of better-grained materials [5]. These insert materials need to have low thermal conductivity to prevent thermal stress and strains through the part.

1.3. Reasons of Failure of Rocket Nozzles

In combustion chambers of rocket motors, highly pressurized combustion products and the high-temperature flow cause erosion and cracking through nozzle parts.

Cracking occurs due to thermal stresses and it may cause severe local erosions around a cracked region and larger amounts of material loss due to the ongoing combustion. This type of failure usually takes place at early stages of operation, when the flow is very hot but deeper regions of the throat are still cold, resulting in large thermal stresses [3].

NASA experimentally tested refractory metals, refractory compounds, graphite, and reinforced plastics for thermal stress cracking and nozzle erosion [3]. Refractory metals, graphite, and fiber-reinforced plastics suffered from nozzle erosion and refractory compounds were mostly damaged by thermal cracking. In summary, none of the materials showed an ultimate performance for all types of tests but some were considered more appropriate for specific requirements.

1.4. Previous Work on the Failure of Graphite Nozzles

The objective of this thesis study is to analyze the structural integrity of solid rocket motor nozzles made by graphite materials under high pressure and temperature loads. Previous work in the literature are mostly related to analyzing the material behavior and thermomechanical behavior of solid rocket motor nozzles, and failure mechanisms of brittle materials like graphite.

Lapp and Quesada [4] presented a road map for the Finite Element Analysis of a solid rocket motor nozzle. In the study, the analysis steps were classified as aerodynamic analysis, thermal analysis, thermomechanical analysis, and mechanical analysis. In aerodynamic analysis step, two-phase flow was solved based on the Euler-Lagrange method. Thermal analysis iterations were done using MARC. In the analysis, radiation and convection were taken into consideration for boundary conditions. Erosion parameters were calculated based on chemical reactions and mass conservation principles. The thermomechanical analysis was done for five different times corresponding to motor ignition, maximum chamber pressure, maximum thermal gradients, an intermediate time on pressure curve, and maximum heating of parts during firing. In the structural analysis, bonding is modeled with gap elements allowing relative motion between the surfaces and by considering friction behavior.

Gomaa and Huang [6] studied thermo-mechanical analysis of a steel- composite rocket nozzle using ANSYS. Firstly, they validated the approximation with a simple case, then they analyzed the nozzle under internal and external thermal loads. A sample problem, stress analysis of a hollow cylinder, has been solved analytically and ANSYS and the results have been compared. The analytical and FEM solutions for different sizes have an agreement on results with small error percentages. Thermo-mechanical analysis of rocket nozzle has been done in two steps, in the first step, a transient heat transfer analysis has been applied to obtain temperature loads through structure depending on time; in the second step, a mechanical analysis has been made to get stress distribution on the structure. As a result of the study, it is seen that thermal loads have a great effect on stress distribution on the rocket nozzle.

Wang et al. [7], prepared a paper exploring the fracture process of the glass window exposed to fire based on the finite element method. He adopted probabilistic and deterministic approaches in his study. He evaluated the stress distribution on glass by maximum Principal stress criterion, maximum Von-Mises stress criterion, maximum shear stress criterion, and Coulomb-Mohr criterion to determine crack initiation. Moreover, he assessed the crack propagation for mixed-mode behavior based on SIFs (Stress Intensity Factor) and energy release rates, SIF-Based maximum circumferential stress criterion, maximum principal stress and CTOA (Crack Tip Opening Angle). The results were compared with experiments and it is concluded that experimental results are closer to results of criteria based on SIFs, energy release rates, maximum principal stresses, and SIF based maximum circumferential stress. According to the study, probabilistic approaches predict the location of crack initiation better than numeric solutions and maximum shear stress criteria predict no failure for given loads so it can be abandoned. Also, the mixed-mode criteria based on SIF, energy release rate, maximum principal stress, and SIF-based maximum circumferential stress criterion agreed with experimental results quite well in terms of crack propagation.

Yu and Crane [8], prepared an article about the analysis method for assessment of Solid Rocket Booster (SRB) design. In the method, the subsequently coupled thermal-mechanical finite element model was adopted. The model differs from previous studies by adding details of Adhesive bond lines, assembly threads and motor case attachments. According to the study, it is crucial to model mesh density through the thickness of the adhesive bond line, temperature-dependent behavior of materials, interaction between motor case and closure and time-dependent thermal loads. The results showed that mesh refinement and detailing of the analysis model improved stress predictions on graphite throat surface.

Sun et al. [9], studied the thermo-structural response of graphite throat by finite element analysis without taking consideration of chemical and mechanical ablation processes. Sun, established an axisymmetric model with all parts of a motor case. Thermal loads were obtained from a 1D flow code and then he applied them to the mechanical model in ANSYS. The results were presented by providing mesh independency and time step independency and according to them, maximum compressive stresses were reached in the radial direction due to thermal gradient through the throat part and it continued to increase as time progressing. The results were also compared with experimental data and in the experiments, locations of crack initiations were seen at an angle of 45°. The analysis model is a simplified method but it shows stress distribution on the throat surface reaches a critical level in the early stages of firing.

Liu et al. [10] studied on Nuclear–grade graphite for its material properties at elevated temperatures. They observed that the strength and toughness of graphite increases as temperature increases on the contrary to the common behavior of other materials. They attributed this behavior relaxation of residual stresses and closure of nano-size cracks with rising temperatures. According to researchers, two toughening mechanisms, intrinsic being materials inherent resistance against microstructural damage, and extrinsic mechanism acting on crack wake, mutually compete with each other. Bridging in crack wake contributes to extrinsic toughening, and as temperature increases, even particle size gets smaller, and more bridging regions emerge and increases the steepness of R-curves resulting in higher toughness.

Gope et al. [11] studied analysis of crack initiation angles with various biaxial loads by using FEM in his paper. The results are assessed and compared with the determinant of stress tensor criterion (DET criterion) and minimum strain energy (SED) theory. SED criterion is important for it is the only criterion showing the dependence of crack initiation angle on material properties. In the analysis, a 2D FEM model was established where the crack tip radius is 0.001 of crack length in ANSYS. The crack tip is modeled with quadratic elements with mid-side nodes placed at the quarter points. The FEM results post-processed with SED and DET were compared with analytical results. It is showed that the results were in good agreement with theoretical and experimental results. Under compressive loads, due to friction and non-inclusion of closing mechanism, results show inconsistency with empirical and theoretical results.

Mehta et al. [12], carried-out a coupled thermo-structured analysis of a graphite insert in a rocket nozzle by solving axisymmetric transient anisotropic heat conduction equation with temperature-dependent thermal properties. The heat conduction problem is solved by using the Galerkin method. The method is validated by ANSYS software. Pressure distribution was applied on the inner surface of the nozzle. According to the results, the nozzle inner surface is under the effect of compressive stresses. Stress direction changed from compressive to tensile through the outer region. In this study, a numerical method was developed to investigate the thermo-structural analysis of a rocket nozzle by solving an axisymmetric, transient, anisotropic heat conduction equation with temperature-dependent material properties.

Kim et. al. [13], investigated thermal shock phenomena which are important to select appropriate throat material due to rapidly high-temperature change occurring. The study material is selected as ATJ Graphite, a common rocket nozzle throat material. In the study, a laser beam is applied to a graphite disc to generate crack initiation and propagation, and then thermal shock resistance and thermal shock fracture toughness were assessed by changing the thickness of the specimen. Thermal shock resistance and thermal shock fracture toughness were calculated by Sato's formula [9]. In the results, it was seen that cracks occurred in the transition region from compressive to tensile stress where temperature values lower than the laser influence area. As the temperature difference between low and high-temperature regions increased, thermal stress values went upward.

Kumar et al. [14], made a parametric study on varying thermal expansion coefficient of C-C type structures in terms of fiber orientation variations. In his paper, he emphasized the necessity of thermo-mechanical analysis and he offered a method to make it. Materials used in a solid propellant rocket motor were described in detail and the behavior of thermal isolator and throat materials were explained under operational conditions. Four load cases which are initial configuration with maximum mechanical and thermal loads, maximum temperature grade through the throat, maximum performing structural load, and maximum temperature soak situation, were mentioned as critical for thermal structural analysis. The maximum pressure load obtained from CFD results is applied on the nozzle surface as constant. As a result of Kumar's work, thermal stresses are more critical in comparison with stresses by causes of structural loads.

Sivakumar and Maji [15], prepared an article based on crack propagation in rocks, a quite brittle material, by using the extended finite element method approach with a cohesive zone model in ABAQUS software. For crack propagation, traction separation law was included to define shear traction and crack displacements across the crack tip. The experiments were done with gypsum which is a brittle rock material, and inclined flaws were intentionally included in the specimens during casting. Uniaxial compression tests were performed varying flaw size and inclination angle. Afterward, the numerical model was established by embracing maximum principle stress criteria as crack initiation criteria. The model was slowly loaded as in the experiment and crack shapes were post-processed and results were in a good agreement with experimental values.

Liu et.al [16], investigated the sensitivity of the coefficient of friction between carbon-based materials and phenolic materials in solid rocket motor nozzles. A finite element model with the thermal-structural couple model was prepared and the results were validated with experiments. Firstly, sensitivity analyses were done for friction coefficient versus displacement, contact gap, contact, and Von-Mises stresses. It was seen that the friction coefficient had a remarkable effect on stress and deformation variation on contact regions. In the experiments, the friction coefficient was measured between 100°C and 500°C with 100°C increments with and without glue. It was found that the friction coefficient decreases with increasing temperature and it varies from 0.48 to 0.18 for glued specimens. In the study, it is concluded that the friction coefficient between throat materials affects the stress distribution and deformation highly so its contribution and sensitivity cannot be ignored for healthy results in finite element solutions.

Phongthanapanich and Dechaumphai [17], developed a finite element method with adaptive Delaunay triangulation working as a mesh generator algorithm to solve crack propagation problems. Mesh algorithm is used for node creation, smoothing and adaptive remeshing by generating small-sized mesh near stress intensity regions and coarser mesh away from stress intensity regions. The results were validated with test data and they had a high similarity for a center cracked plate, single edge cracked plate and single edge cracked with three holes. Each case was validated also by analytical results with a very close approximation. The study is a good source for the validation of FEM results and also having an informative explanation for the crack propagation mechanism.

Strauss and Cullen [18], edited a study made by ASTM to be a reference for the fractography method a failure analysis procedure investigating crack surfaces of materials. In the book, widely seen fracture types were presented by various cases. One of these cases was a sintered tungsten rocket nozzle liner and the cause of failure was suspected from thermal stresses at early stages of firing test when tensile stresses reached maximum due to high rate heating. Crack was initiated from the outer surface of the case and propagation stopped by reaching of crack near to transition region from tensile to compressive stresses. In the book, photos of fracture surfaces were placed so that the visualization of fracture were enabled for researchers. The study is quite valuable to be a guide for the fracture mechanism of materials for different/similar types of loadings and different types of materials.

Nambu and Enoki [19], published a paper about the evaluation of flaws inside porous graphite specimens by using a method named Acoustic emission. Analytical relations and experiments were used to evaluate mechanical properties, Weibull variables and R-curve values of graphite specimens. In the experiments, four-point bending tests for fracture toughness and loading-unloading tests were conducted by using a three-point bending test to obtain R-curves. In an analytical approach, two models were adopted. In the first model, random micro-cracks were generated by no interaction with each other and stress was found with usage of Weibull Distribution. In the second model, cracks are focused on one point and propagate very rapidly for a certain value of stress.

Fernández-Canteli et al. [20], prepared a study about a tension test named Modified Compact Test used for determining fracture energy of concrete. However, the test method has not been recognized as a valid test for fracture energy determination yet, the results were consistent with analytical and numerical results. The test procedure was simulated in ABAQUS and ATENA commercial finite element codes. The researcher used a correction method to decrease numerical errors in the solution and the correct results of finite element solutions were quite consistent with experimental results. Moreover, the effect of modeling techniques on fracture energy was argued.

Burchell et al. [21], published a study about the fracture toughness test of nuclear graphite grades. He followed ASTM D 7779 Standard Test Method for the Determination of Fracture Toughness of Graphite at Ambient Temperature. Different grades of graphite were tested and critical stress intensity factors for mode 1 were recorded and compared based on their grades. As a result of the study, it was found that fine-grained graphite tended to be more brittle. Similarly, coarser graded graphite tended to show more micro cracking even they were weaker than fine graded ones in terms of strength. Moreover, one of the major results of the study was that critical stress intensity factors varied by 50% for one type of specimen in the experiments.

Bhushan and Panda [22], published a study about the bi-modularity behavior of graphite material and its effect on fracture toughness (K_{IC}), critical J-integral (J_{IC}) and critical strain energy release rate (G_{IC}). By tensile and compression tests they determined the bi-modularity index (Ratio of Tensile Elastic Modulus to Compressive Elastic Modulus). To determine the fracture parameters, (K_{IC}), (J_{IC}), (G_{IC}), a 3-point bending test was done by the following methodology in ASTM D7779 Standard. The test results were evaluated by the Weibull method to guess the mechanical behavior of graphite. According to findings, failure probability is highly affected by stress state of test specimens. Especially for critical strain energy release rate and critical J-integral test values, significant differences were seen. This difference was attributed to the bi-modularity effect of graphite by considering its highly brittle behavior. The main conclusion from the study is that the SERR criterion is more valid than critical J integral value since it is directly related to load-displacement data.

Gross and Srawley [23], published a technical note to share results of a comparison between a boundary value collocation procedure applied to William stress function and a three-point bending test. The test procedure repeated for the different span to width ratio to calibrate the procedure for Stress intensity factor. In the analytic solution, William stress function was satisfied by a harmonic relation and boundary conditions through the crack and stress components were obtained by considering symmetry conditions. According to results, three-point bending values for equality dependent on geometry, loading, and SIF, were lower than pure bending values in the literature but as the span to width, the ratio increases the difference got smaller. It can be concluded that there is a limit for geometrical parameters in a three-point bending test to measure fracture toughness for healthy results.

1.5. Problem Definition

In a combustion chamber, after the ignition of the propellant; temperature and pressure rise quickly. The surface temperature of flow-facing parts reaches to 2000 K and above. As the parts of the rocket farther away from the flow are still at room temperature, a large temperature gradient occurs within the nozzle. This temperature gradient results in a thermal expansion gradient, causing large stresses. These stresses eventually cause crack initiation and propagation, putting the integrity of the nozzle under risk. In this thesis, a generic nozzle configuration has been investigated to gain insight into the failure behavior of graphite nozzles.

1.6. Proposed Methods and Models

To simulate the rocket nozzle behavior under high thermal and pressure loads, a series of experiments and finite element simulations were done. Firstly, to correctly model the material properties of graphite, thermal and structural material experiments were performed. Secondly, operational conditions were determined to define the boundary conditions of the problem. To obtain these conditions, flow and thermal simulations were run, since acquiring data from a rocket combustion chamber through experimentation is not feasible. Thirdly, a finite element analysis model was established based on the results of material characterization experiments, flow simulations, and thermal simulations to investigate fracture behavior of solid rocket motor nozzle under operational conditions.

CHAPTER 2

EXPERIMENTAL CHARACTERIZATION OF GRAPHITE

2.1. Introduction

Assessment of fracture behavior of graphite material requires determination of mechanical properties such as elastic modulus, tensile-compressive strength, fracture toughness and thermal properties such as thermal conductivity, thermal diffusivity, and heat capacity. All of these properties were determined by mechanical and thermal tests for Mersen-2020 graphite.

In this chapter, mechanical tests and thermal tests are explained and results are presented.

2.2. Thermal Tests

Thermal expansion coefficient and thermal conductivity are the key parameters that affect the thermal stresses in a structure [24]. Therefore, systematic experiments were performed for this purpose.

Thermal tests were made by ROKETSAN. The results, which are used in the subsequent simulations are summarized in this section for the completeness of the chapter.

Thermal conductivity, thermal diffusivity, density, thermal expansion, and heat capacity tests were conducted at temperatures in the range of 20°C – 2000°C. In measurements of specific heat, NIST (Material Measurement Laboratory) is used as a reference. Test results were reported with 200 °C increments.

Thermal expansion tests were handled with high-temperature resistant tools. In the tests, the graphite samples with 6 mm diameter and 20 mm length were heated under helium atmosphere linearly with a dilatometer up to 2000 °C at a rate of 10 °C/min. The test device was calibrated using a commercial graphite specimen. Thermal results are provided in Figure 2.1, Figure 2.2, Figure 2.3, and Figure 2.4. According to the figures, specific heat and coefficient of thermal expansion of graphite increase with increasing temperature. The increase in specific heat is very drastic up to about 1500 K, and then it becomes almost stable. The increase in the coefficient of thermal expansion is also sharp up to about 1000 K, then it also becomes mostly stable. On the other hand, thermal conductivity and thermal diffusivity decrease sharply with increasing temperature.

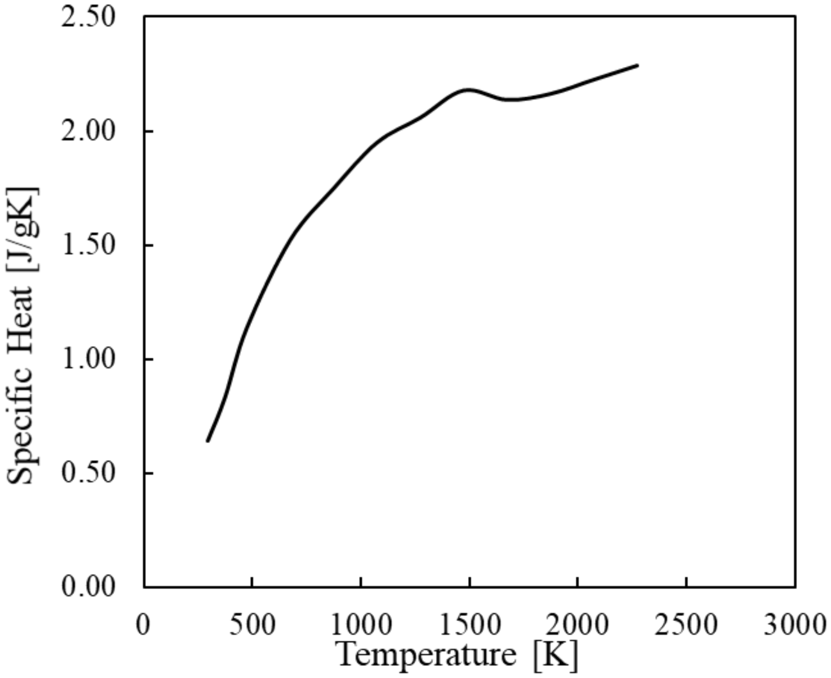

Figure 2.1. Change of specific heat of graphite with increasing temperature.

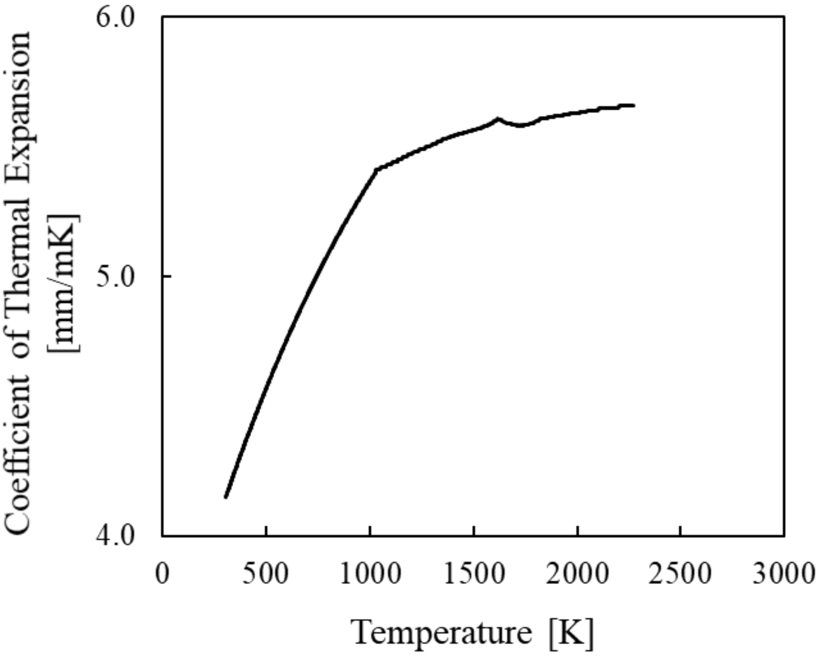

Figure 2.2. Change of coefficient of thermal expansion of graphite with increasing temperature.

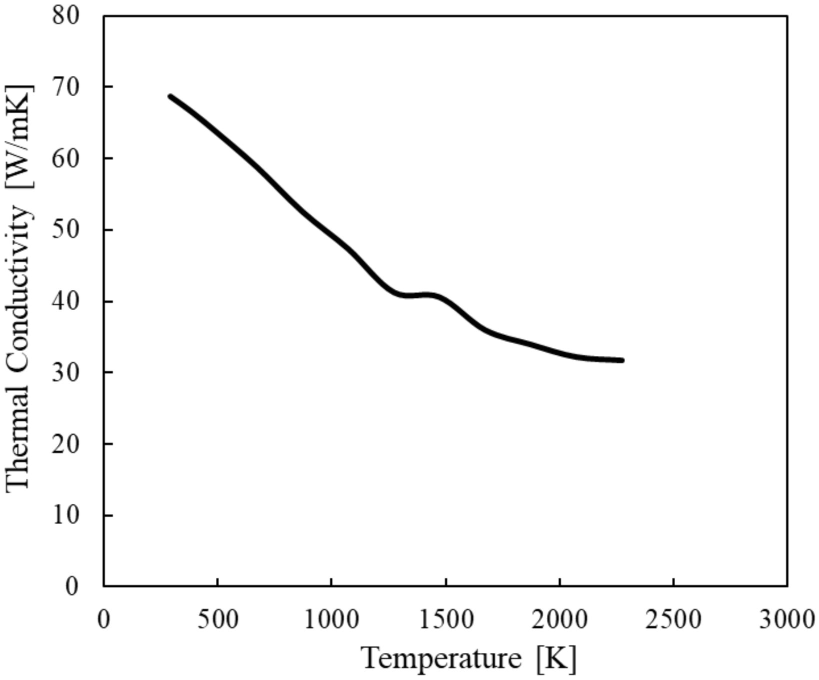

Figure 2.3. Change of thermal conductivity of graphite with increasing temperature.

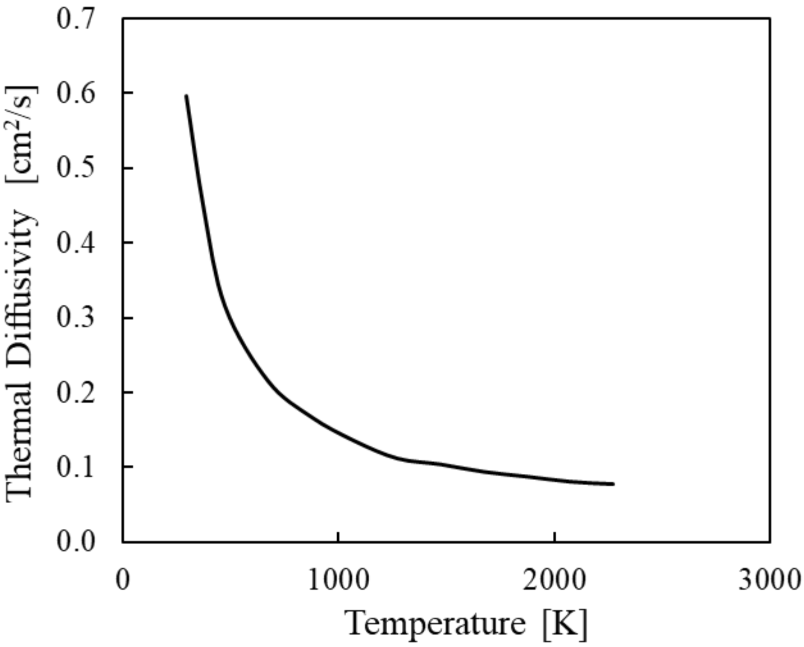

Figure 2.4. Change of thermal diffusivity of graphite with increasing temperature.

2.3. Mechanical Tests

Tensile, compressive and fracture toughness tests were conducted for the determination of mechanical properties of graphite. In the next sections, each test will be explained and results will be presented.

2.3.1. Tensile Tests

Tensile tests were made by ROKETSAN and results were used as input properties for Finite Element Simulations.

Tensile tests were done in a mechanical testing machine for different temperatures with a stain rate of 10^{-5} s^{-1}. Six specimens were tested and stress-strain curves were recorded. Three specimens were extracted from a long cylinder block such that their loading axis coincides with the longitudinal axis of the cylinder. The other three specimens were extracted in a transverse direction. This approach aimed at investigating the possible anisotropy in the structural properties. According to results, graphite has tensile structural properties that are close to each other for both longitudinal and transverse directions. For brittle materials, tensile tests are extremely hard since gripping should be done with caution. Any high-stress point may lead to premature fracture during testing. The stress-strain curves for transverse and longitudinal directions are presented in Figure 2.5.

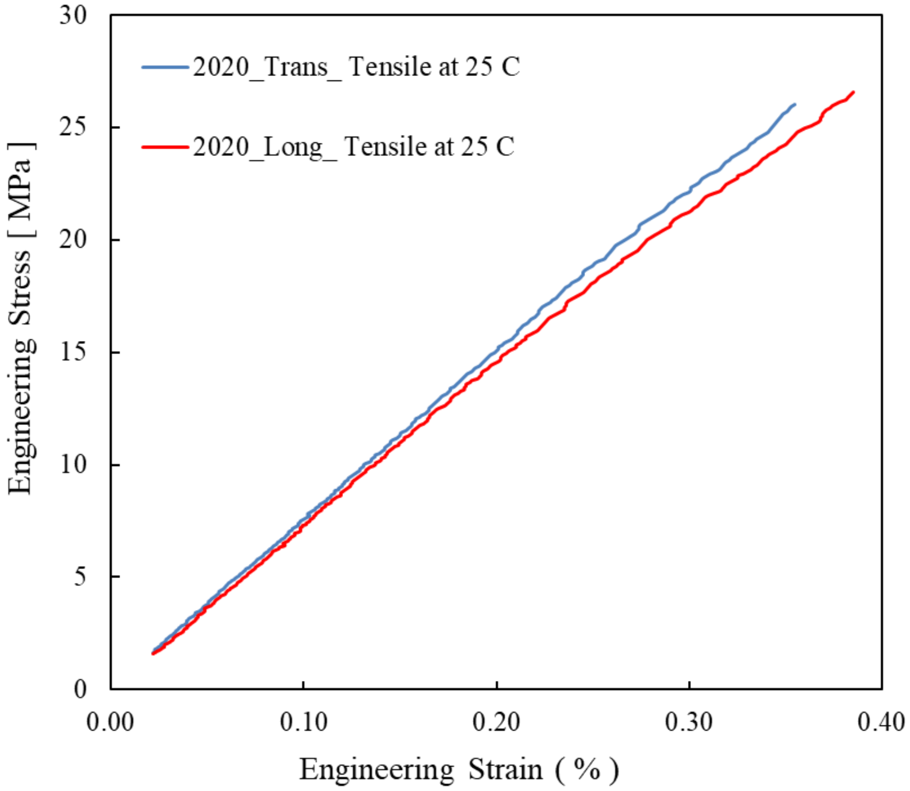

Figure 2.5. Tension test stress-strain curves for longitudinal and transverse directions at room temperature.

In the results of tensile tests, there are slight variations in the stress-strain behavior. By means of least-squares method, experimental data was linearized and elastic modulus was found as 7.15 GPa, and ultimate tensile strength was found as about 25 MPa. These experimental results are used as input material data to the Finite Element Simulations. The linearized stress-strain curve is provided in Figure 2.6.

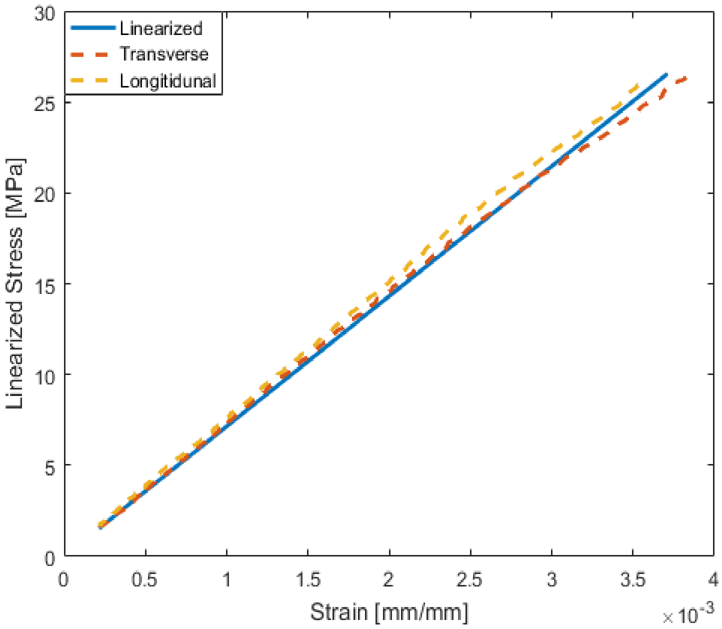

Figure 2.6. Linearized tension test stress-strain curves of longitudinal and transverse directions.

2.3.2. Compression Tests

Compression Tests were done by ROKETSAN in the material characterization laboratory. The results were used as input data for the Finite Element Analysis.

Compression tests performed in a Gleeble testing machine. Four specimens were tested by displacement control. The specimen size was based on ASTM C 695 Standard [25]. Test specimen properties are shown in Table 2.1.

Table 2.1. *Compression Test Specimen Type and Size*

Specimen	**Length**	**Diameter**	**Quantity**
Cylinder	20 [mm]	10 [mm]	4

Stress-strain curves of loaded specimens are provided in Figure 2.7. The main objective of tests was obtaining stress-strain curve which is used for determining compressive elastic modulus and compressive strength of graphite. In Figure 2.7, graphite shows a softening behavior as strain increases. The maximum compressive strength varies between 110 MPa and 120 MPa. Figure 2.8 shows the elastic modulus change with strain. Elastic modulus decreases with increasing strain. The minimum elastic modulus is about 5000 MPa and the maximum elastic modulus is about 17000 MPa. In [26], it is stated that the stress-strain behavior of polycrystalline graphite is non-linear under compression and plastic deformation may be introduced at very low strain values. Furthermore, the stress-strain behavior of polycrystalline graphite differs in tension and compression.

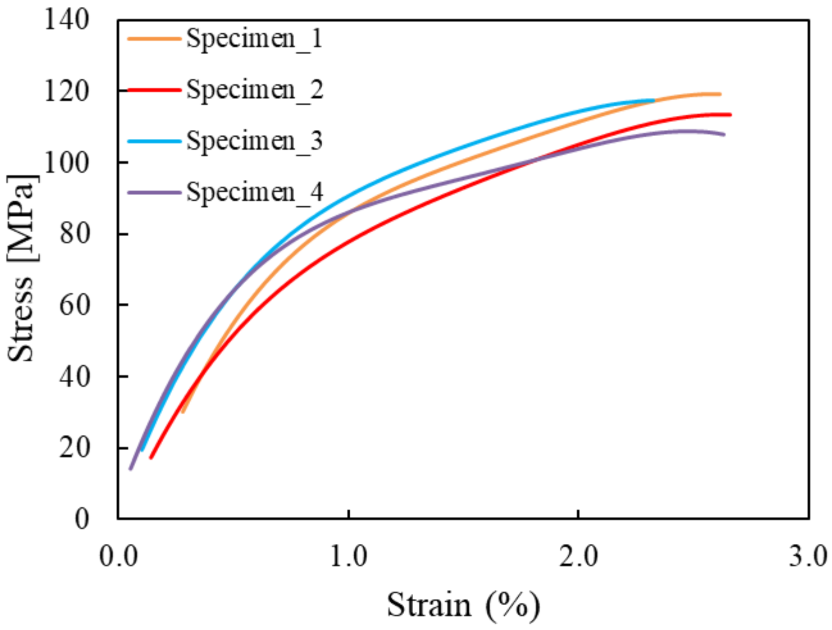

Figure 2.7. Stress-strain curves of loaded specimens.

In a test study [27], the temperature dependency of graphite strength was measured by conducting compressive tests. In the compression tests, cylindrical specimens were compressed with an apparatus attached to copper electrodes used for heating the specimen. The strength of graphite was measured at the temperatures from 20 °C to about 2000 °C. The variation of compressive strength with increasing temperature is demonstrated in Figure 2.9.

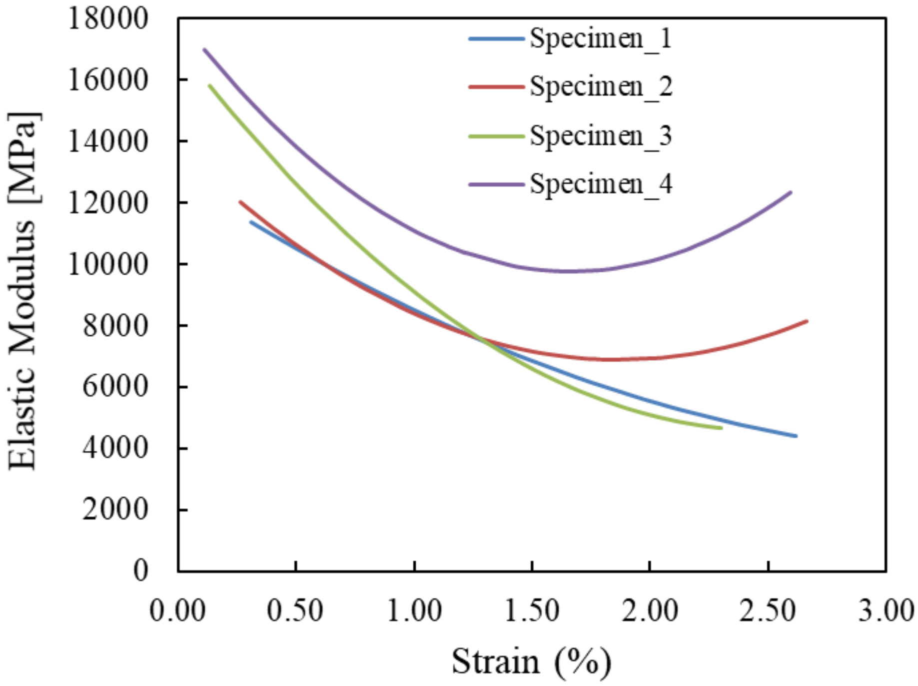

Figure 2.8. Elastic modulus- strain (%) graphs of compression test specimens.

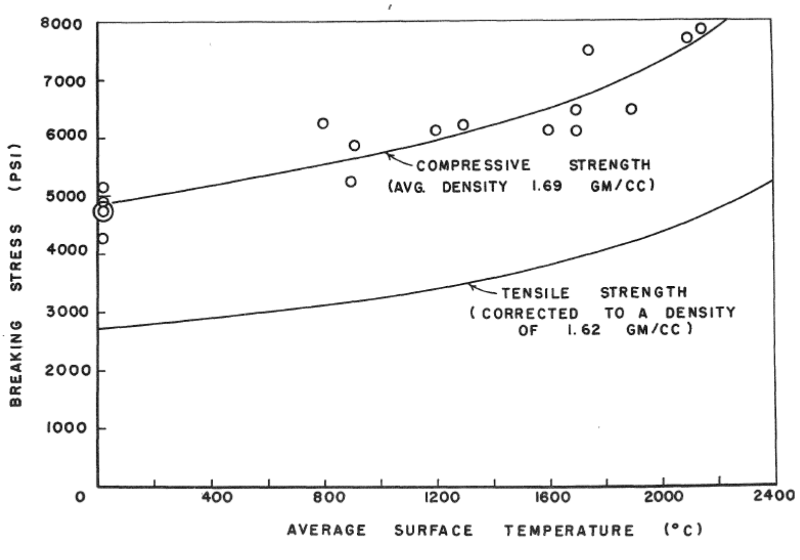

Figure 2.9. Behavior of compressive strength against temperature, figure taken from [27].

Since the compressive tests were made in room temperature, strength value is considered to be independent of temperature in the finite element modeling. Since strength improves with temperature, this is an assumption on the safe side.

Bhushan et al. [22] calculated compressive elastic modulus from linearized compressive stress-strain data following the procedure mentioned in ASTM E111 standard [28]. In this way, it is easier to follow differences in elastic modulus of each specimen. In [26], it is mentioned that stress-strain behavior of polycrystalline graphite shows different behavior under tension and compression. Bhushan [22] relates this behavior with bimodularity (different stress-strain behavior under tension and compression) of polycrystalline graphite. For this purpose, elastic modulus of polycrystalline graphite for tension and compression were calculated separately by using linearly regressed data of experimental results.

Stress-strain data was linearized with least-square method and it is provided in Figure 2.10. Average elastic modulus for linearized compressive data is found as 5.6 GPa. Hence bimodularity index (ratio of tensile modulus to compressive modulus) is found as 1.27.

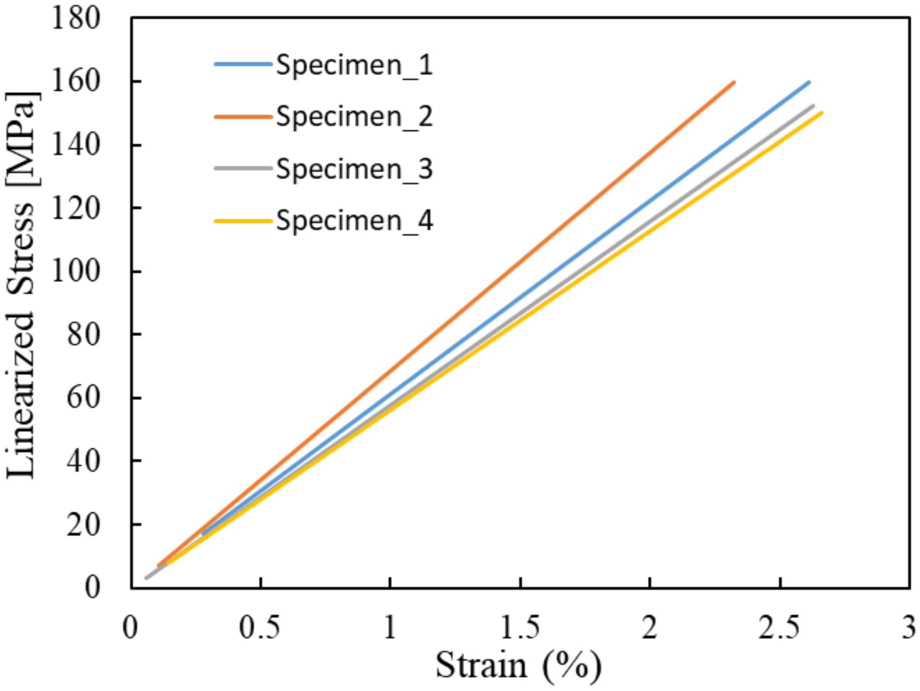

Figure 2.10. Linear regression results of compressive stress-strain data of four compression test specimens.

2.3.3. Fracture Toughness Tests

Fracture toughness tests were conducted in RÜZGEM laboratories in the Aerospace Engineering Department of Middle East Technical University with three points bending test setup.

In fracture toughness tests, ASTM D7779 standard [29] have been used. Each specimen has dimensions of 200 mm x 20 mm x 15 mm. The specimens were notched by using EDM. Each notch has a nominal length of 8 mm. The width is 0.5 mm with a 30° V-notch at the tip with a radius of 0.1 mm. Span length was arranged as 160 mm by using 10 mm diameter cylindrical supports. The span to width ratio (S/W) was calculated as 8. The sample geometry dimensions can be found in [29]. Test setup is composed of an Autograph AGS-J testing machine, two roller supports and one roller to load the specimen as shown in Figure 2.11 below.

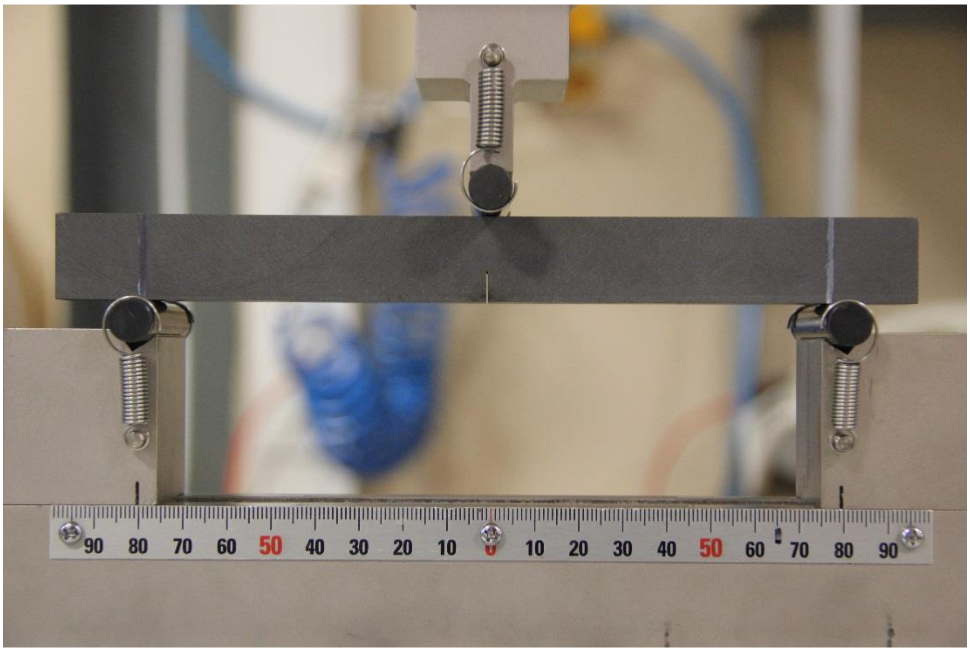

Figure 2.11. A photograph of fracture toughness test setup

In the testing procedure, the samples were loaded with 0.5 mm/min. Loading rates were applied as slow as possible to avoid vibrational effects. ASTM 7779 Standard suggests a displacement rate of 0.1 mm/min but the minimum rate of the test setup was higher than this value.

In fracture tests, four specimens were aligned and loaded very carefully, force-displacement curves were recorded, and photographs were taken to observe crack propagation for each test. Except for the first test, all specimens were loaded until fracture occurred. In the first specimen, a crack was allowed to propagate but then the loading was stopped to investigate the propagated crack under a microscope. Load-displacement curves of fracture toughness tests are provided in Figure 2.12.

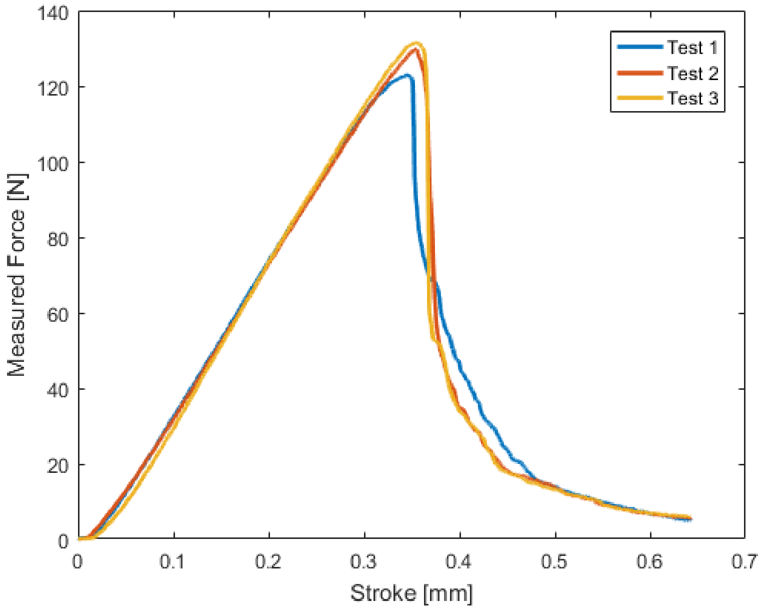

Figure 2.12. Load-displacement curves of fracture toughness tests.

During the loading of the SENB samples, it was observed that crack propagated in a stable fashion; there was no dynamic fracture sign such as rapid cracking or branching of cracks. A microscope image of a crack can be seen in Figure 2.13. Microscope images show that a successful crack was obtained from the test. In Figure 2.14, crack propagation can be observed. The crack propagated slowly in all specimens through the loading point in a straight path. A crack angle of almost zero means the crack direction is parallel to the loading direction. This is a typical result of Mode-I crack propagation.

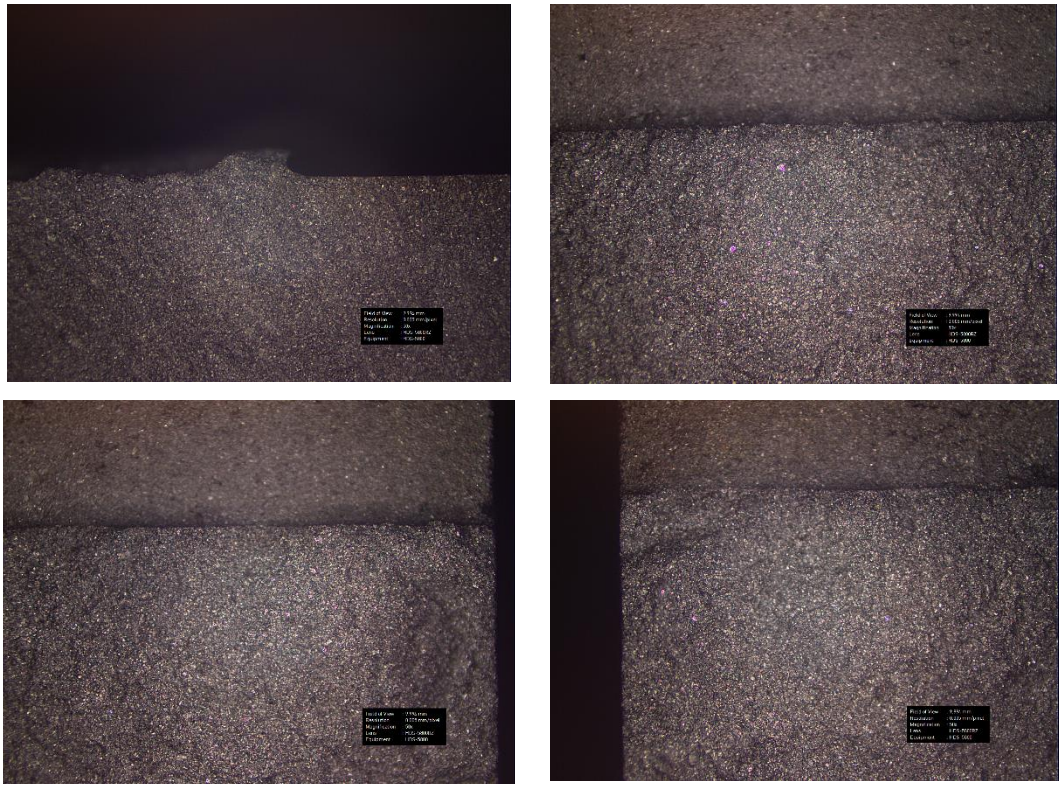

Figure 2.13. A microscope image of cracked specimen.

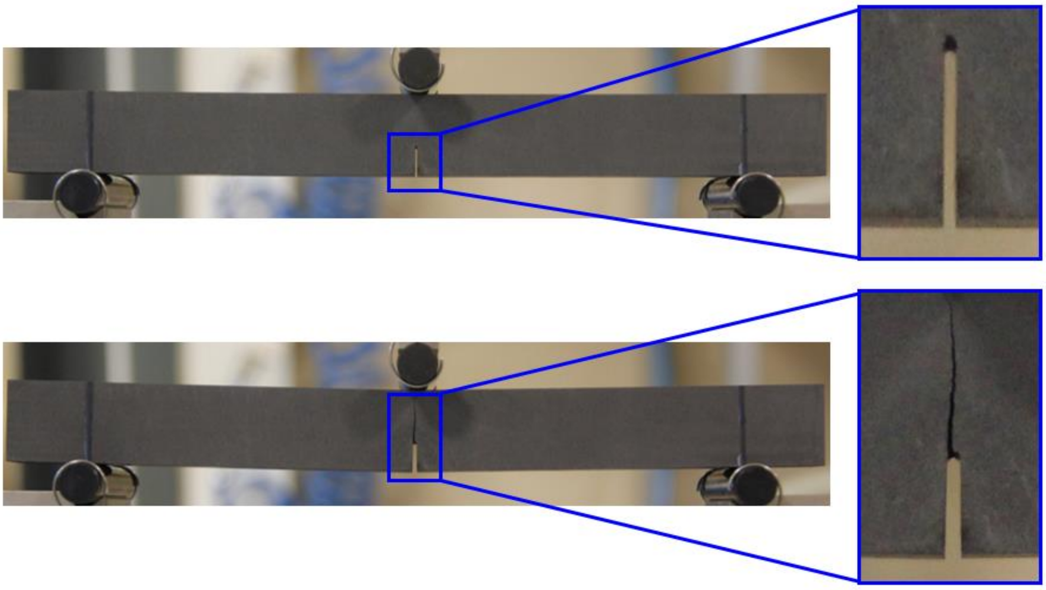

Figure 2.14. The crack propagation on SENB specimen in fracture toughness test.

According to [29], load displacement curves of fracture tests exhibit a quasi-stable crack growth resistance behavior. Dynamic and stable crack types, are also shown in [29]. For three-point flexure test *S/W* is recommended to be $5 \leq \frac{S}{W} \leq 10$ and it is 8, and *a/W* is recommended to be $0.35 \leq \frac{a}{W} \leq 0.6$ where it is 0.4 in this study. Hence, equation (2.1) can be used to calculate fracture toughness. In equation (2.1), P_{max} N is the peak load in the load-displacement curve of test specimen and *B* is the depth of the specimen.

$$K_{IC} = g\left[\frac{P_{max} * S * 10^{-6}}{B * W^{\frac{3}{2}}}\right]\left[\frac{3\left[\frac{a}{W}\right]^{\frac{1}{2}}}{2\left[1-\frac{a}{W}\right]^{\frac{3}{2}}}\right] \tag{2.1}$$

Where g is a function of (*a/W*);

$$g = A_0 + A_1\left(\frac{a}{W}\right) + A_2\left(\frac{a}{W}\right)^2 + A_3\left(\frac{a}{W}\right)^3 + A_4\left(\frac{a}{W}\right)^4 + A_5\left(\frac{a}{W}\right)^5 \tag{2.2}$$

Table 2.2. *Coefficients of g(a/W).*

	S/W				
	5	**6**	***7***	***8***	***10***
A₀	1.9109	1.9230	1.9322	1.9381	1.9472
A₁	-5.1552	-5.1389	-5.1007	-5.0947	-5.0247
A₂	12.688	12.6194	12.3621	12.3861	11.8954
A₃	-19.5736	-19.5510	-19.0071	-19.2142	-18.0635
A₄	15.9377	15.9841	15.4677	15.7747	14.5986
A₅	-5.1454	-5.1736	-4.9913	-5.1270	-4.6896

By putting P_{max} into equation (2.1) K_{IC} values were obtained and plotted in Figure 2.15.

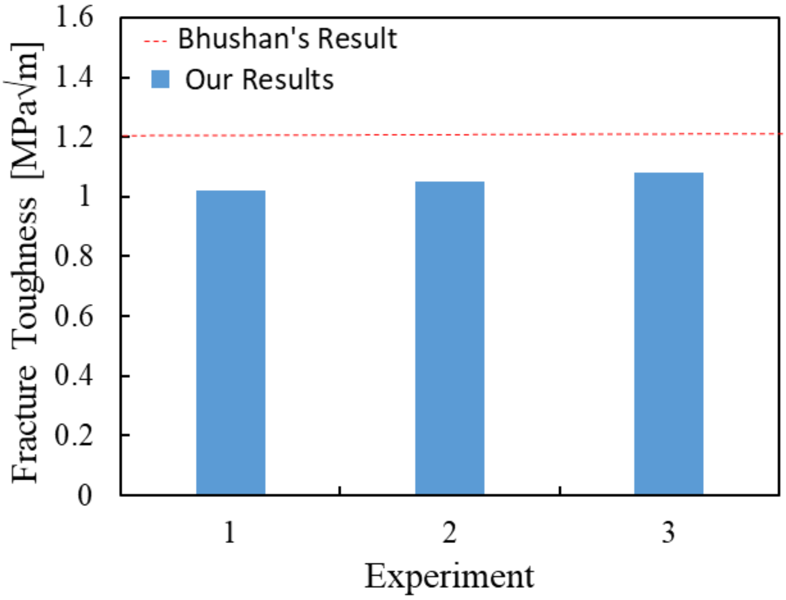

Figure 2.15. Critical stress intensity factors of fracture toughness tests and comparison with Bhushan's results.

In the calculation of G_{IC} load vs. displacement data in each point, at the beginning of tests, an initial nonlinearity was observed, and data was linearized by using linear regression method. The straight line obtained was used for the calculation of G_{IC}. The linear equation is given as follows:

$$y = a_0 + a_1 x \tag{2.3}$$

a_0 and a_1 values are given in Table 2.3.

Table 2.3. *Linearization constants for tests.*

	a_0	a_1
Test_1	5.9	315.4
Test_2	-6.87	394.35
Test_3	-11.65	419.34

Equation (2.3) is changed into the form of $y = a_1 x$ so that the straight line initiates from the origin. To do this, the straight line was shifted. Linearized load-displacement curves are provided in Figure 2.16. By using linearized values, compliance and crack extension can be calculated for each test.

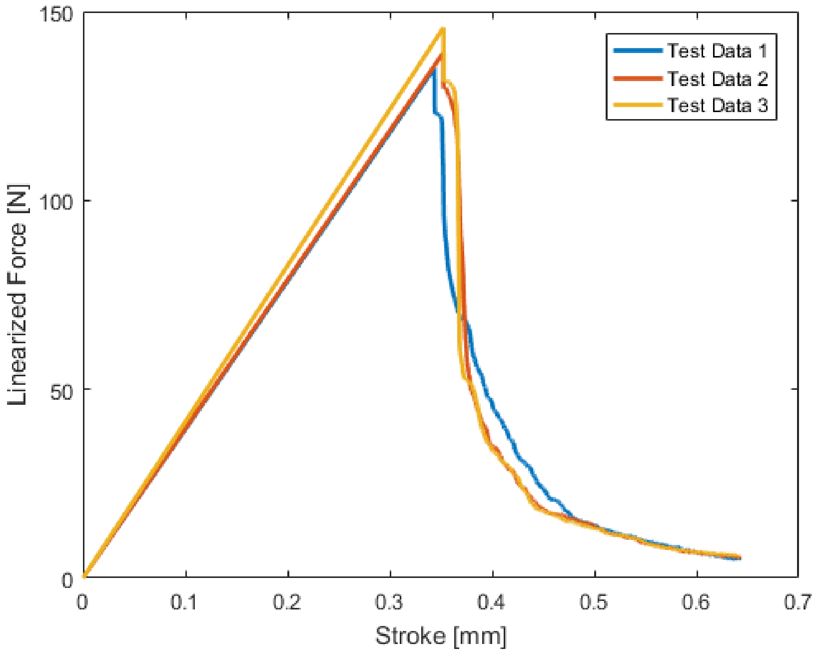

Figure 2.16. Linearized load-displacement curves.

$$C_n = \frac{D_n}{P_n} \tag{2.4}$$

$$a_n = a_{n-1} + \left[\frac{W-a_{n-1}}{2} * \left(\frac{C_n - C_{n-1}}{C_{n-1}}\right)\right] \tag{2.5}$$

D_n is displacement value for point n, P_n is force value for point n, a_0 is the initial crack length. Using the results of equation (2.4) and equation (2.5) strain energy release rate, $G(a_n)$ is evaluated for each data point n by the equation (2.6).

$$G(a_n) = \frac{P^2}{2B}\frac{C_n}{C_{n-1}}\frac{a_n}{a_{n-1}} \tag{2.6}$$

The SERR vs. Δa plot is expected to decrease as crack propagates till fracture. The maximum SERR point is called as G_{IC} for that particular experiment. Mean and standard deviations for each specimen for this study and Bhushan’s study are presented in Table 2.4 and Table 2.5.

Table 2.4. *Mean and standard deviation values of K_{IC}, G_{IC}, J_{IC} of test results.*

K_{IC} [MPa√m]		G_{IC} [J/m^2]		J_{IC} [J/m^2]	
Mean	*STD*	*Mean*	*STD*	*Mean*	*STD*
1.0815	0.0419	271.9337	13.8931	120.5344	9.3717

Table 2.5. *Mean and standard deviation values of K_{IC}, G_{IC}, J_{IC} in Bhushan's study.*

K_{IC} [MPa√m]		G_{IC} [J/m^2]		J_{IC} [J/m^2]	
Mean	*STD*	*Mean*	*STD*	*Mean*	*STD*
1.2055	0.1418	207.851	45.6365	168.7984	37.4834

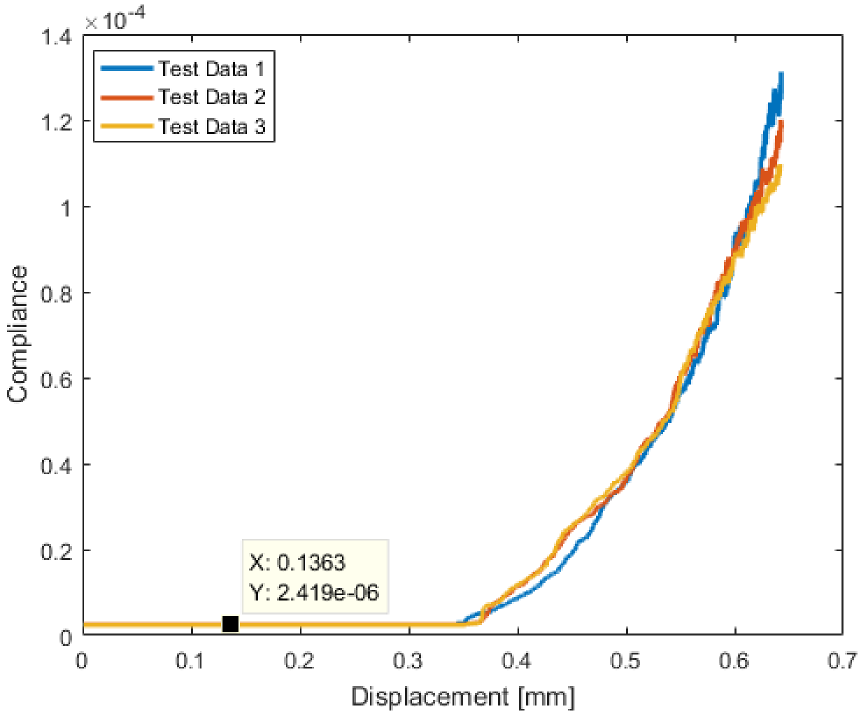

Figure 2.17. Compliance-displacement values of fracture toughness test specimens.

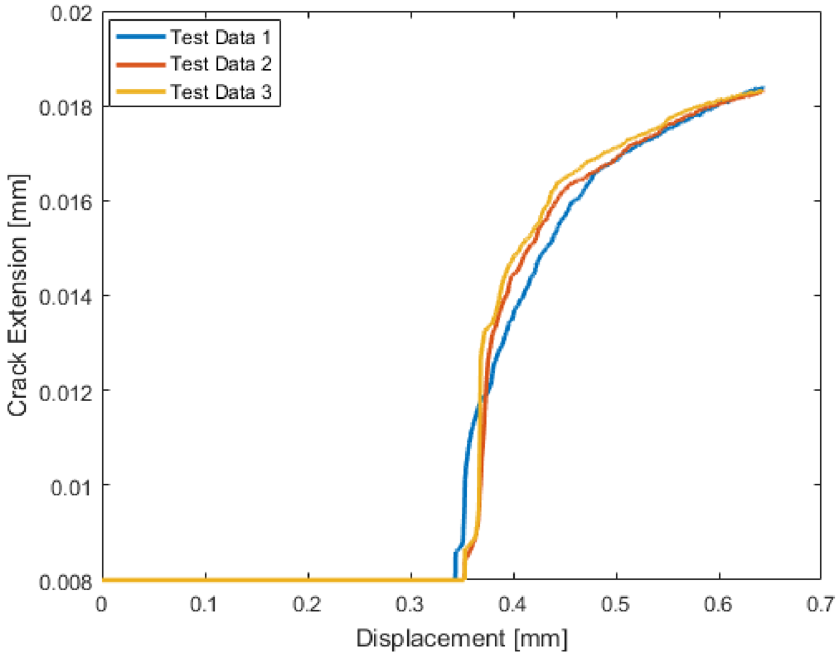

Figure 2.18. Crack extension-displacement values of fracture toughness test specimens.

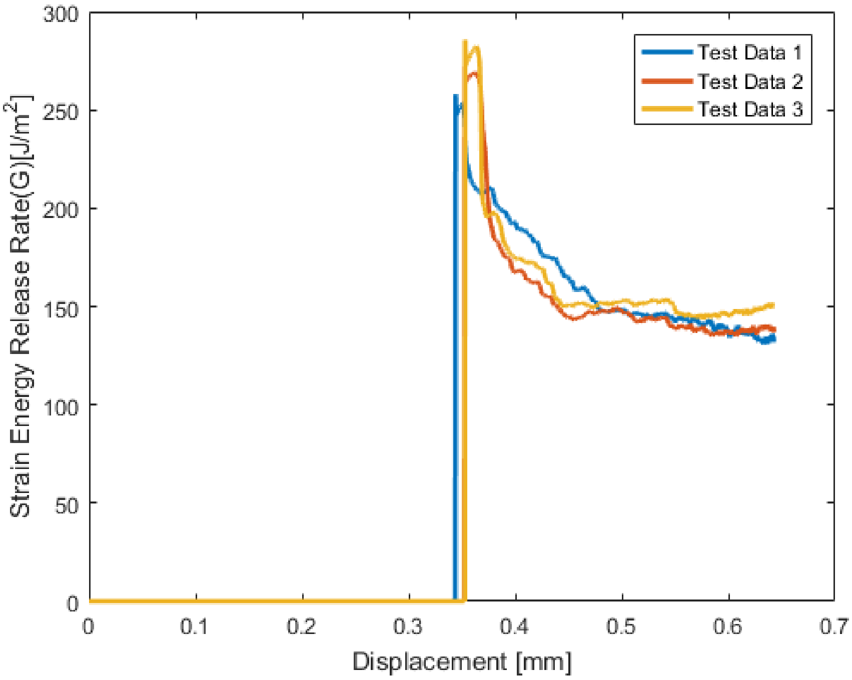

Figure 2.19. Strain energy release rate (SERR)-displacement values of fracture toughness test specimens.

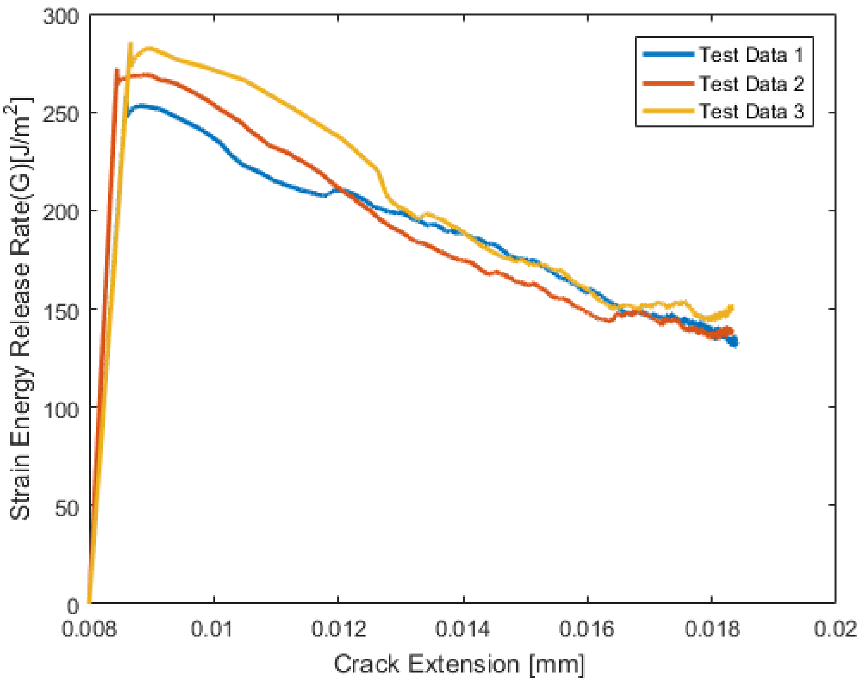

Figure 2.20. Strain energy release rate (SERR)-crack extension values of fracture toughness test specimens.

The fracture parameters presented in Figure 2.17, Figure 2.18, Figure 2.19, and Figure 2.20 are calculated from D7779 Standard. Compliance is inverse slope of load displacement curve and it starts to increase after crack initiates. Before crack initiation, its value is almost zero. Moreover, SERR decreases as crack extension increases. It is the result of the decrease in stiffness due to crack extension.

In brittle materials with no plastic deformation, *J*- Integral values are equal to SERR and J_{IC} is calculated from the following expression for plain strain case:

$$J_{IC} = \frac{(1-\nu^2)K_{IC}}{E} \tag{2.7}$$

Bhushan et al. [22] found that, for bimodular materials showing different stress-strain performance in tension and compression, J_{IC} and G_{IC} are different. They conducted thirty SENB tests with graphite material and calculate the values of J_{IC} and G_{IC} and compared the results in Figure 2.21. These parameters characterized crack propagation and they should have same values in theory for unimodular materials.

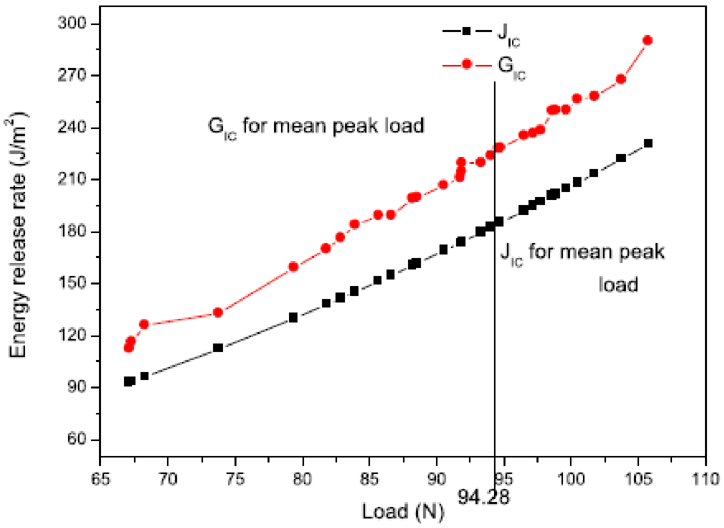

Figure 2.21. Critical J-Integral and SERR comparison, figure taken from [22].

In our case, J_{IC} and G_{IC} values were also different; J_{IC} and G_{IC} comparison is shown in Figure 2.22. In such cases, Bhushan suggests to use G_{IC} value. The reason is that J_{IC} values are calculated from peak loads of the experiment. On the other hand, G_{IC} values are calculated from whole experimental data so it has more reliability.

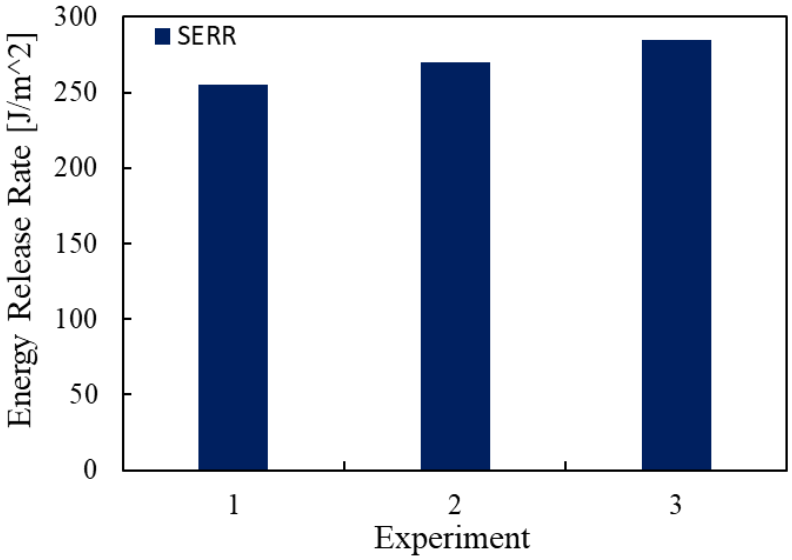

Figure 2.22. Critical J-Integral and SERR comparison.

CHAPTER 3

MODELING OF CRACK PROPAGATION USING EXTENDED FINITE ELEMENT METHOD

3.1. Linear Elastic Fracture Mechanics (LEFM)

3.1.1. Fracture Modes

Three independent movement known as fracture modes illustrated in Figure 3.1 were mentioned in [24]. Distinct fracture modes named as mode I, mode II and mode III and combinations of them describe failure mechanism in a part.

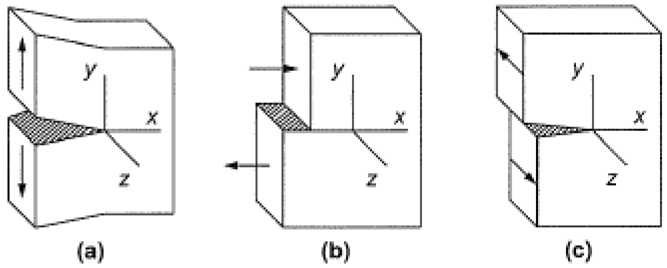

Figure 3.1. Schematic view of fracture modes a) Mode I, b) Mode II, c) Mode III, figure taken from [24].

In mode 1, known as opening mode, motion is perpendicular to the crack plane and symmetric for the upper and lower side.

In mode 2, known as sliding mode, motion is parallel to crack plane and, upper and lower parts slides on each other. This motion causes a shear crack on the part and no out of plane deformation is observed in this mode.

In mode 3, known as tearing mode, motion is transverse to the crack plane and, upper and lower parts slide over each other. This motion causes out-of-plane shear mode on the part.

3.1.2. Stress Intensity Factor

In linear elastic materials, stress field on the crack tip is characterized by Stress Intensity Factor (SIF) and it is used as a fracture parameter especially in brittle materials due to very little plastic deformation. The parameter is used to predict crack growth by comparing with fracture toughness of the material. SIF depends on applied stress, crack size and location, and size of geometry. Stresses are given in terms of SIFs as in equation (3.1).

$$\begin{aligned} \sigma_{yy} &= \frac{K_I}{\sqrt{2\pi x}} + O(\sqrt{x}), \sigma_{xy} = \sigma_{yz} = 0 \\ \sigma_{xy} &= \frac{K_{II}}{\sqrt{2\pi x}} + O(\sqrt{x}), \sigma_{yy} = \sigma_{yz} = 0 \\ \sigma_{yz} &= \frac{K_{III}}{\sqrt{2\pi x}} + O(\sqrt{x}), \sigma_{yy} = \sigma_{xy} = 0 \end{aligned} \tag{3.1}$$

SIFs can be calculated by using various analytical/numerical methods for a given crack problem. In equation (3.1), K_I, K_{II}, K_{III} are SIFs for opening, sliding and tearing fracture modes. In most failure types, Mode-I is the dominant fracture mode [30]. When a polar coordinate system (r, θ) is placed at the crack tip, the stress field solution near the crack tip can be calculated by using K_1 with equation (3.2) where r is the distance from crack tip to stress field.

$$\begin{aligned} \sigma_{xx} &= \frac{K_1}{\sqrt{2\pi r}} \cos\left(\frac{1}{2}\right)\theta(1 - \sin\left(\frac{1}{2}\right)\theta \sin\left(\frac{3}{2}\right)\theta \\ \sigma_{yy} &= \frac{K_1}{\sqrt{2\pi r}} \cos\left(\frac{1}{2}\right)\theta(1 + \sin\left(\frac{1}{2}\right)\theta \sin\left(\frac{3}{2}\right)\theta \\ \sigma_{xy} &= \frac{K_1}{\sqrt{2\pi r}} \sin\left(\frac{1}{2}\right)\theta \cos\left(\frac{1}{2}\right)\theta \cos\left(\frac{3}{2}\right)\theta \end{aligned} \tag{3.2}$$

3.1.3. Fracture Toughness

Fracture toughness is the resistance of a material against a crack extension. It is a material property determined by the experiment. According to the linear elasticity theory, the stress field is inversely proportional to the square root of a distance of crack tip. Irwin proposed when the stress intensity reaches a critical value which is fracture toughness of the material, crack extension occurs. In reality, a crack tip is surrounded by a fracture process zone in which material damage and plastic deformation exist

[31]. In this process zone, the LEFM solution is not used but outside of this region, the LEFM solution is more accurate for a certain range of *r*.

Fracture toughness is highly dependent on temperature change; by assumption of constant temperature, the fracture toughness variation with thickness is showed as in the Figure 3.2.

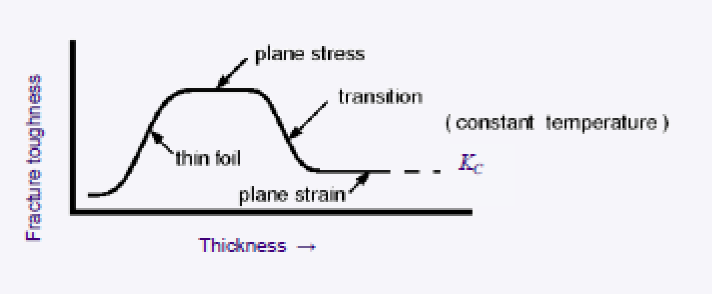

Figure 3.2. Schematic view of fracture toughness variation with thickness, figure taken from [5].

Usually, plain strain value is the value obtained from fracture toughness experiments however, if specimen thickness is small, fracture toughness value is somewhere between plane stress and plane strain values. Apart from thickness and temperature change, fracture toughness is also dependent on the crack extension. When fracture toughness is a function of crack extension, it is called a resistance curve and the resistance curve is stable for brittle materials in case of no plastic deformation.

3.2. Extended Finite Element Method (XFEM)

XFEM is developed by Belytschko in 1999 [5]. It is enlargement of the traditional finite element method using partition operation as crack paths. As opposed to the traditional approach, XFEM allows the existence of discontinuities in an element by adding extra degrees of freedom by using special displacement functions. Previously, the virtual crack closure method and cohesive zone modeling were used to predict crack propagation but these modeling methods were unable to model discretionary crack propagation since crack growth was limited with boundaries of the elements and the crack path should have been predetermined before crack initiation [32]. Traditional methods also needed to remesh at the crack tip. On the other hand, to model fracture in bulk materials, XFEM allows a crack to be present in an interior element so that crack initiates and propagates in a solution dependent path as independent of mesh. This feature makes it popular because of not being needed to refresh the mesh and also specifying a prior path for a crack extension. For stationary cracks, to enhance the convergence rate, XFEM uses singular crack tip enrichment functions. Moreover, the technique enables to predict critical flaw size to find load carrying capacity for cracked parts in linear and nonlinear analysis. In consideration of solving FEM problems with discontinuities in geometry (cracks), it is essential to determine displacement jump across the crack surfaces. XFEM uses two methods which are cohesive zone modeling (CZM) and virtual crack closure technique (VCCT) for deciding the distance between crack faces. Also, to locate the discontinuity, it uses a level set method (LSM). These concepts will be explained in the following parts.

3.2.1. Enrichment

XFEM enriches the discontinuous fields and near tip asymptotic fields of finite element methods by extra functions called as "enrichment functions". It was introduced by Belytschko and Black [33] based on the partition of unity method of Babuska and Melenk [34]. The method is explained in the study of Belytschko et al. [35] by using a 2D model consisting of four elements.

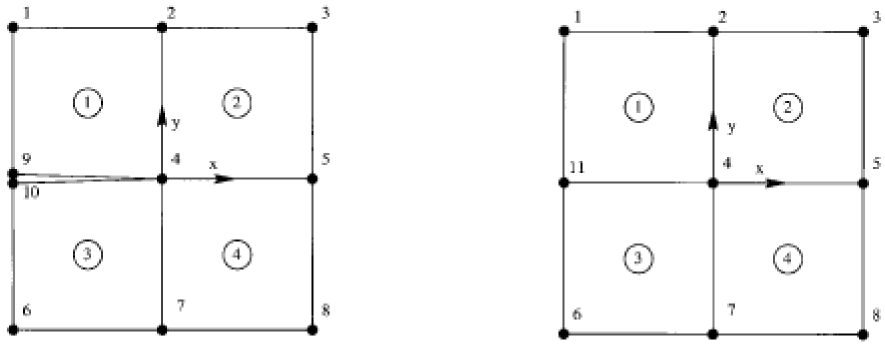

a) Finite element mesh near a crack tip

b) Regular mesh without a crack

Figure 3.3. Schematic view of initiation of crack between elements, figure taken from [36].

$$u^h(x) = \sum_{i=1}^{10} u_i N_i(x) \qquad (3.3)$$

where u_i is displacement at node I and N_i is the associated shape function.

a and b are defined as

$$a = \frac{u_9+u_{10}}{2}, b = \frac{u_9-u_{10}}{2} \tag{3.4}$$

u_9 and u_{10} can be expressed in terms of a and b,

$$u_9 = a + b, u_{10} = a - b \tag{3.5}$$

By replacing u_9 and u_{10} in terms of a and b;

$$u^h(x) = \sum_{i=1}^{8} u_i N_i(x) + a\big(N_9(x) + N_{10}(x)\big) + b\big(N_9(x) + N_{10}(x)\big)H(x) \tag{3.6}$$

H(x) is the Heaviside function representing displacement jump across crack surfaces and it is defined in local coordinate system where it is placed into crack tip, as;

$$H(x) = \begin{cases} 1 \; if \; (x - x^*).n \geq 0 \\ -1 \; otherwise, \end{cases} \tag{3.7}$$

Where x is a gauss point, and x^* is the nearest point to x on the crack and n is normal to the crack in outward direction at point x^* in Figure 3.5. .

H(x) is 1 on element 1 and -1 on element 3. $N_9(x) + N_{10}(x)$ is replaced by $N_{11}(x)$ and a by u_{11}, then the approximation will be;

$$u^h(x) = \sum_{i=1}^{8} \underbrace{u_i N_i(x) + u_{11}(N_{11}(x))}_{\text{Classic Finite Element}} + \underbrace{b(N_{11}(x))H(x)}_{\text{Discontinuous Enrichment}} \tag{3.8}$$

In the above equation crack is modeled by an interface between two adjacent elements. If the case is opposite, appropriate nodes and associated enrichment functions are selected. If there will be an enrichment for a node is determined so far as its shape function support is cut by crack interior.

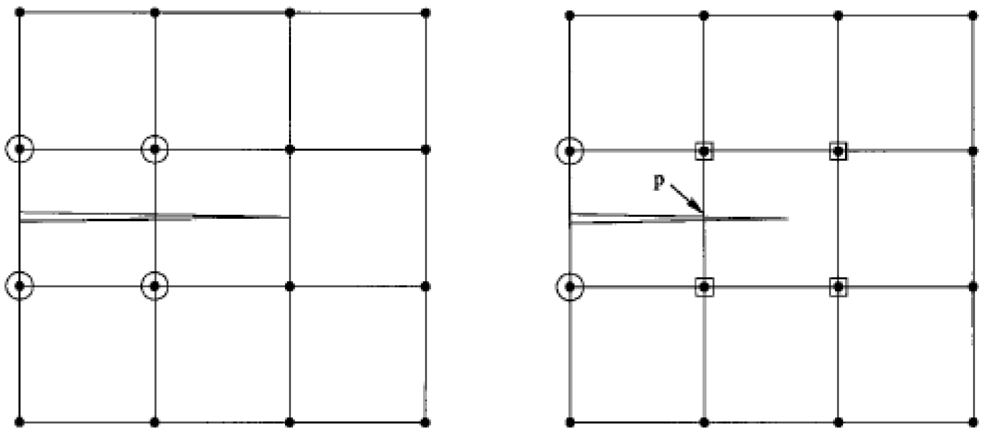

a) Circle nodes are enriched b) Circle and square nodes are enriched

Figure 3.4. Schematic view of enrichment of nodes, figure taken from [36].

For a more general case, the crack does not adjust with element edges or even does not coincide with edges, discontinuity cannot be expressed sufficiently by the Heaviside function. Circle nodes are enriched by jump functions however; the crack tip is not modeled. Hence, squared nodes are enriched with asymptotic crack tip functions with the technique introduced by Belytschko [32] is described as;

$$u^h(x) = \sum_{i\epsilon I} u_i N_i(x) + \sum_{j\epsilon J} b_j N_j(x) H(x) + \sum_{k\epsilon K} N_k \left(\sum_1^4 c_k^l F_l\,(x)\right) \tag{3.9}$$

Where J is circled nodes and K is squared nodes. Crack tip asymptotic functions $F_l(x)$ are presented as;

$$\{F_l(r,\theta)\} := \left\{\sqrt{r}\sin\left(\frac{\theta}{2}\right), \sqrt{r}\cos\left(\frac{\theta}{2}\right), \sqrt{r}\sin\left(\frac{\theta}{2}\right)\sin(\theta), \sqrt{r}\cos\left(\frac{\theta}{2}\right)\cos(\theta)\right\} \tag{3.10}$$

In which *(r,θ)* are the local polar coordinates at the crack tip. This equation is valid for crack with one crack tip.

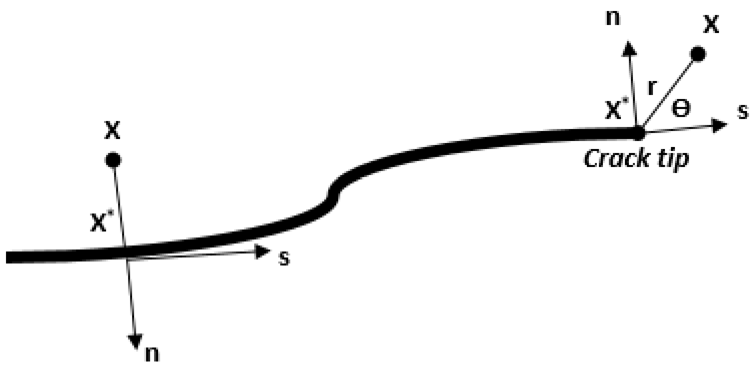

Figure 3.5 Illustration of polar and n-t coordinates for a smooth crack, figure taken from [36].

3.2.2. Cohesive Segment Method and Phantom Nodes

In the classical finite element method, modeling a crack tip is a hard job since the singularity needs tracking of crack propagation location. Hence, to solve moving cracks can be modeled with a cohesive segment and phantom nodes method which is an approach dependent on traction separation law. The cohesive approach can be used for both brittle and ductile materials to simulate crack growth.

In the phantom node approach, imaginary nodes are placed on original nodes to simulate discontinuity of cracked elements. Hence, there exist two nodes, one phantom and one original, on each node location for a cracked element. When the element is cut with crack phantom nodes and original nodes are separated and element splits into two parts. From this point, phantom nodes do not have to move together with original nodes since cohesive strength between nodes becomes zero. An illustration of phantom nodes is shown in Figure 3.6.

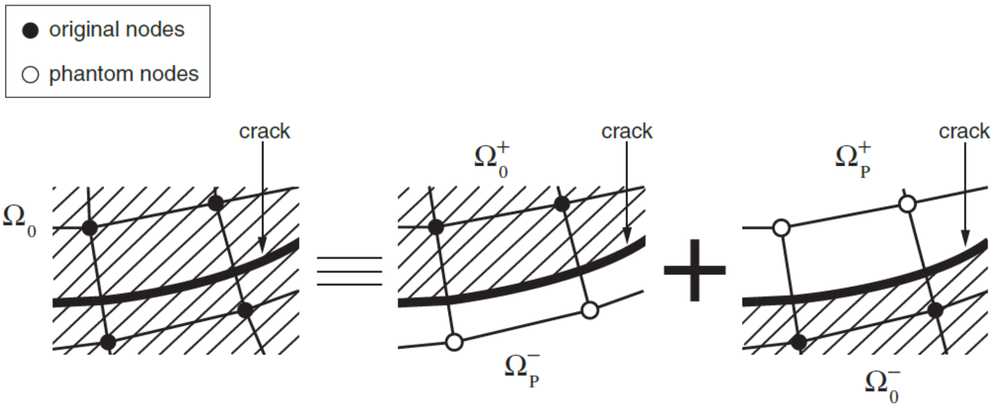

Figure 3.6. Schematic view of phantom node principle, figure taken from [36].

It is an effective method to model multiple cracks in solid parts and exhibits no mesh dependency in case the mesh is sufficiently refined.

3.2.3. XFEM Based Traction-Separation Cohesive Behavior

In ABAQUS XFEM, the behavior of cohesive elements and surface-based cohesive behavior are extended to the linear elastic traction-separation model, damage initiation criterion and damage evolution law [33]. In the linear elastic traction-separation model, for crack initiation and evolution linear elastic behavior which is written in terms of elastic constitutive matrix relating normal and shear stresses to normal and shear separations. $\boldsymbol{t_n}$ and $\boldsymbol{t_s}$ which are normal and shear tractions can be written in the form of equation (3.11).

$$[\boldsymbol{t}] = \begin{bmatrix} \boldsymbol{t_n} \\ \boldsymbol{t_s} \end{bmatrix} = [\boldsymbol{K}][\boldsymbol{\delta}] = \begin{bmatrix} \boldsymbol{K_{nn}} & \boldsymbol{0} \\ \boldsymbol{0} & \boldsymbol{K_{ss}} \end{bmatrix} \begin{bmatrix} \boldsymbol{\delta_n} \\ \boldsymbol{\delta_s} \end{bmatrix} \tag{3.11}$$

for 2D analyses. In this formulation, normal and shear tractions are decoupled terms so they don’t contribute any cohesive force to each other. $\boldsymbol{K_{nn}}$ and $\boldsymbol{K_{ss}}$ (stiffness values in normal and shear directions) are calculated from elastic material properties.

$$\boldsymbol{\delta} = \frac{\boldsymbol{t}}{\boldsymbol{K}} \quad \textit{where}\ \boldsymbol{K} = \frac{\boldsymbol{E}}{\boldsymbol{L}} \tag{3.12}$$

3.2.3.1. Damage Initiation

In ABAQUS, multiple damage initiation criteria can be defined as an accurate representation of the material model. When the criterion is met, material damage is initiated within the element. A couple of initiation criteria are provided by ABAQUS such as Maximum Nominal Stress Criterion (MAXS), Maximum Nominal Strain Criterion (MAXE), Quadratic Nominal Stress (QUADS), and Quadratic Nominal Strain (QUADE) [36]. Except for those, user-defined damage initiation criterion is allowed to define by UDMGINI subroutine [37]. User-subroutine enables one to define more than one failure criterion for the same analysis.

3.2.3.2. Level Set Method

In ABAQUS, Level Set Method and XFEM work together. Level Set Method is used to describe crack geometry discontinuity since mesh generation is not needed to conform to crack geometry. The level set method is a powerful numerical method to track surface motion. The crack geometry is tracked with the help of two nearly orthogonal signed distance functions. One of the functions define the crack surface (ϕ), the second one is used to construct an orthogonal surface (ψ) so crack can be tracked by intersecting of these two surfaces. In the Figure 3.7, n^+ shows positive normal direction and m^+ shows positive normal to crack front.

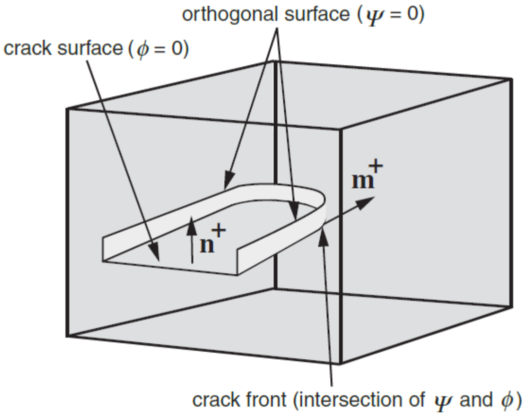

Figure 3.7. Representation of a nonplanar crack in three dimensions by two orthogonal surface, figure taken from [36].

3.3. Verification of the Modeling Approach

Aim of this section is to verify FEA Modeling method with experimental data and analytical solution of simple geometries in context of fracture mechanics.

3.3.1. The SENB Specimen Three Point Bending Test

3.3.1.1. Problem Description

In this study, it is aimed to verify analysis modeling method with XFEM and written subroutines to determine crack initiation and propagation of a SENB (Single Edged Notched Beam) specimen in three-point bending loading conditions. In order to analyze the problem XFEM Cohesive based approach was used. A two-dimensional model was setup and loaded in Mode-I by displacement taken from fracture toughness experiment in chapter 2. The results were compared with experimental data.

3.3.1.2. Geometry and Model

A SENB geometry taken from ASTM D7779 Standard Test Method for Determination of Fracture Toughness of Graphite at Ambient Temperature [29] was studied. The specimen is shown in Figure 3.8, with a length of 200 mm and width, W, of 20 mm. The initial crack length, *a*, is 8mm and thickness of the specimen is 15 mm. Span which is the length between two roller supports, S, is taken as 160 mm and *S/W* ratio is taken as eight.

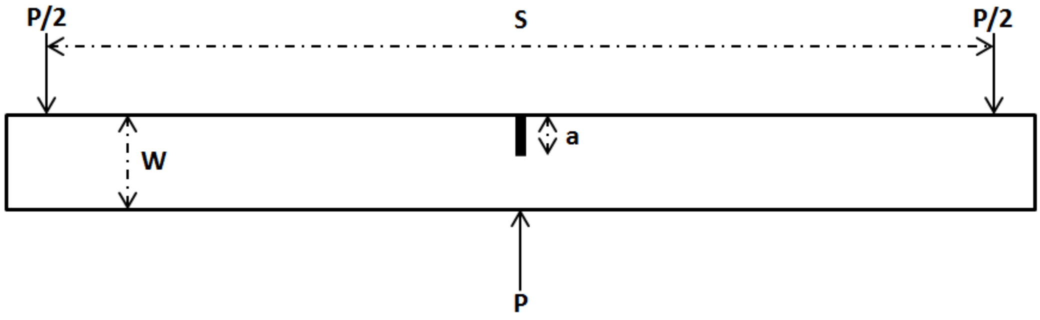

Figure 3.8. Free body diagram of the SENB specimen geometry in D7779 standard, figure taken from [29].

The applied time displacement curve is shown in Figure 3.9. The maximum displacement is given as about 0.6 mm. Displacement controlled loading provides better convergence than load controlled loading. Model mesh size was determined with a series of mesh convergence analyses with different element sizes. A static solution step is defined with a time of loading duration.

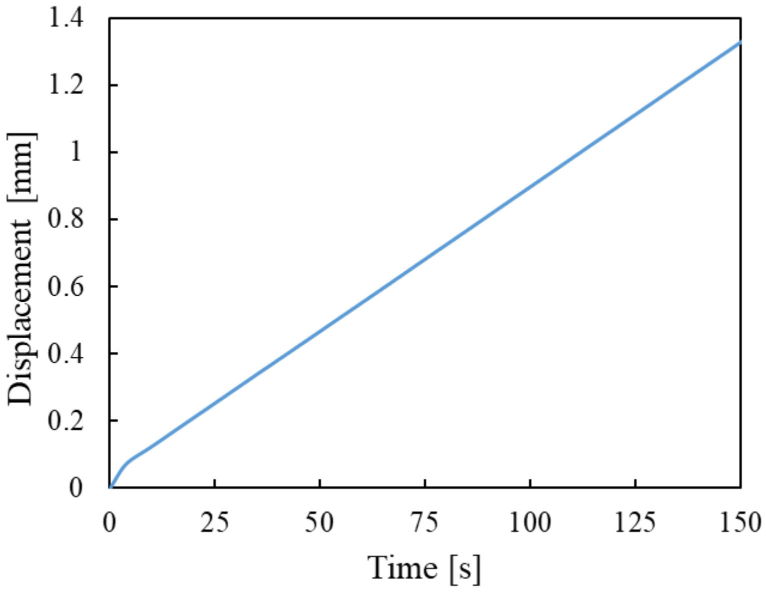

Figure 3.9. Time-displacement curve applied to FEA model.

The FEA model shown in Figure 3.10, has 28160 linear plain strain hex elements. The enriched region having a finer mesh than the surrounding region is shown with a red dashed frame. Rigid supports have been constrained from two translation-DOF (Degree of Freedom) and one rotational-DOF around a plane normal axis. For crack modeling, XFEM was used with USDFLD subroutine enabling changing elastic modulus value concerning sign of stress field and strain value of compression data.

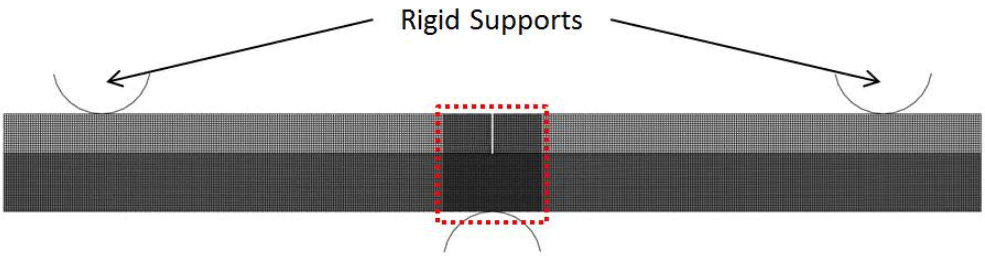

Figure 3.10. The FEA model illustration.

3.3.1.3. Material

Material properties of graphite were defined with data obtained from material characterization experiments in chapter 2. In this simulation, only the elastic properties of the material were used. The elastic properties are dependent on three independent variables, stress sign, strain value, and temperature but in this simulation, temperature dependency was ignored since experiments were done at room temperature.

According to tensile and compressive mechanical tests, while graphite shows a linear stress-strain relation in the tensile test, its behavior in compressive tests is nonlinear, and it is softened with increasing strain. Hence, in the compressive stress field, strain value is a field parameter for elastic modulus. To implement the effect of strain value and stress sign two field parameters were defined in input files. One of parameter controls the stress sign and other parameter controls strain value. Bhushan made a similar approach to model D7779 Standard fracture toughness test only considering stress sign effect. They established a 3D crack analysis model to simulate the fracture toughness test. They used the same geometry with D7779 Standard and applied the mean peak load. For crack analysis, they used the contour integral method defining twelve contour lines. Their results are quite consistent with experimental data. The flow chart used in [22] is displayed in Figure 3.11 with an addition showed in red frame. In a similar way, graphite was modeled by considering softening effect under compression with a generated USDFLD subroutine. In the subroutine, elastic modulus of graphite is determined according to average value of principal stresses. If the average is lower than zero then compressive elastic modulus will be used else, tensile elastic modulus will. Furthermore, compressive elastic modulus is defined as a function of strain. Hence, present strain value enables the subroutine to use corresponding elastic modulus to take softening behavior of graphite under compression.

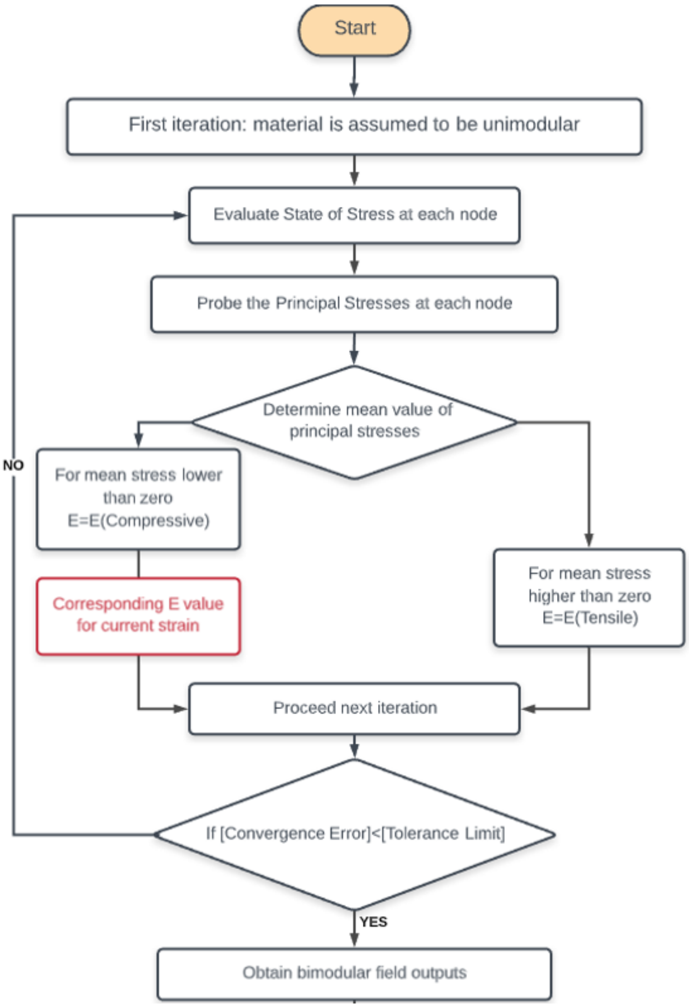

Figure 3.11. Flow chart for evaluation of stress fields, figure taken from [22].

The crack initiation was modeled by using Mohr-Coulomb (MC) failure criterion and maximum principle stress criterion. For this purpose, ABAQUS UDMGINI subroutines [37] were used. Figure 3.12 demonstrates working principle of UDMGINI subroutine used to evaluate crack initiation in throat part during thermo-mechanical analysis. When the average of principal stress is compressive, Mohr-Coulomb criterion was applied, and when the average is tensile, maximum principle stress criterion was used. The failure index (FI) for negative average principal stresses is showed with equation (3.13) and FI for positive average principal stresses is shown with equation (3.14).

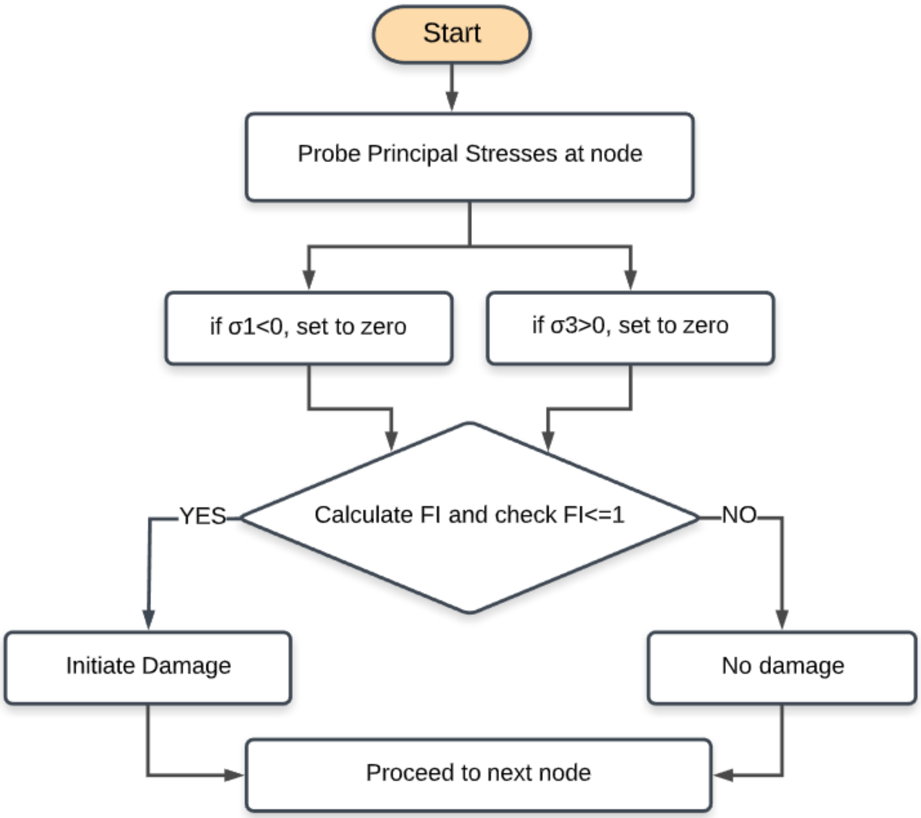

Figure 3.12. Process of crack initiation criterion in UDMGINI subroutine.

Mohr-Coulomb criterion aims at detecting mode II type cracks whereas maximum principle stress criterion predicts mode I type cracks.

According to MC criterion, maximum shear stress is the driving load for failure. Because of this, maximum and minimum principal stresses determine the behavior. The MC criterion is given by:

$$FI = \frac{\tau}{c - \sigma \, tan\phi} \leq 1 \tag{3.13}$$

where τ is shear strength, σ is normal stress, c is cohesion yield stress of material, ϕ is material friction angle and, FI is the failure index. When the right hand side of equation (3.13) reaches the shear strength, crack is initiated. The same criterion can be expressed as a function of maximum and minimum principal stresses (σ_3, σ_1) as follows.

$$f(\sigma_1, \sigma_3) = (\sigma_1 - \sigma_3) + (\sigma_1 + \sigma_3) sin\phi - 2c \, cos\phi = 0 \tag{3.14}$$

Furthermore, c and ϕ are related to tensile and compressive strength as:

$$\sigma_t = 2c \, \frac{cos\phi}{1 + sin\phi} \tag{3.15}$$

$$\sigma_c = 2c \, \frac{cos\phi}{1 - sin\phi} \tag{3.16}$$

A schematic representation of MC is provided in Figure 3.13.

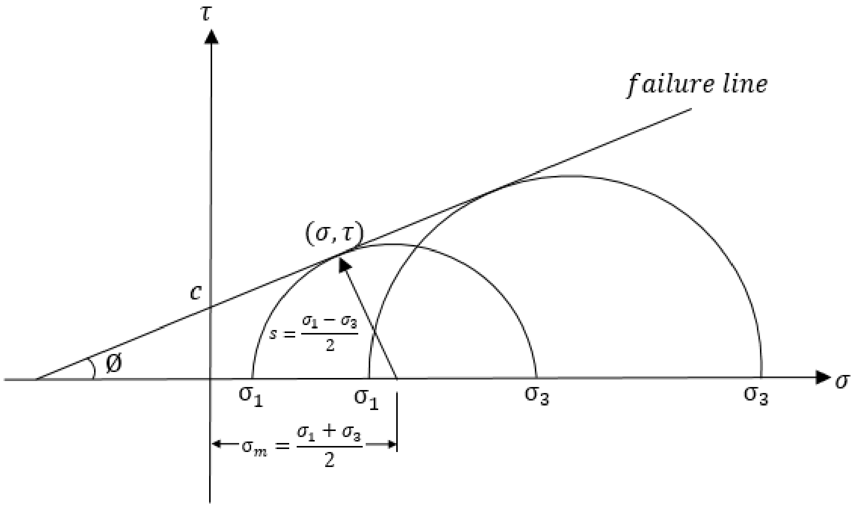

Figure 3.13. Mohr-circle representation of Mohr-Coulomb failure criterion.

The maximum principle stress criterion starts a crack when maximum normal stress for a stress element reaches to the tensile strength of the material. Its formulation is as follows:

$$FI = \frac{<\sigma_1>}{S_t} \leq 1 \qquad (3.17)$$

$< \sigma_1 >$ is the magnitude of maximum principle tensile stress and it is only considered if the stress is tensile. S_t is the tensile strength of the material and FI is the failure index.

Crack evolution was modeled using Benzeggagh-Kenane (BK) fracture criterion which is a correlation between mixed mode critical fracture energies of mode I, II and III. This model is effective for isotropic materials with identical first and second shear fracture energies [5], such as graphite. BK criterion is defined as:

$$G_n^C + (G_s^C - G_n^C)\left\{\frac{G_S}{G_T}\right\}^{\eta} = G_C \qquad (3.18)$$

Where

$$G_S = G_s + G_t \qquad (3.19)$$

$$G_T = G_n + G_s \qquad (3.20)$$

G_s and $G_t$are the first and second shear mode energies, respectively; and G_n is the normal mode fracture energy. η is a material parameter.

3.3.1.4. Results and Discussion

The stress field of loaded specimen is shown in Figure 3.14. The first figure shows onset of crack initiation. At the notch tip, principal stresses increase besides, tensile and compressive stress fields emerge with increasing loading. The second figure shows propagated crack state. Tensile stresses propagate with the crack tip till fracture. Apart from crack tip region, stress sign does not change through loading.

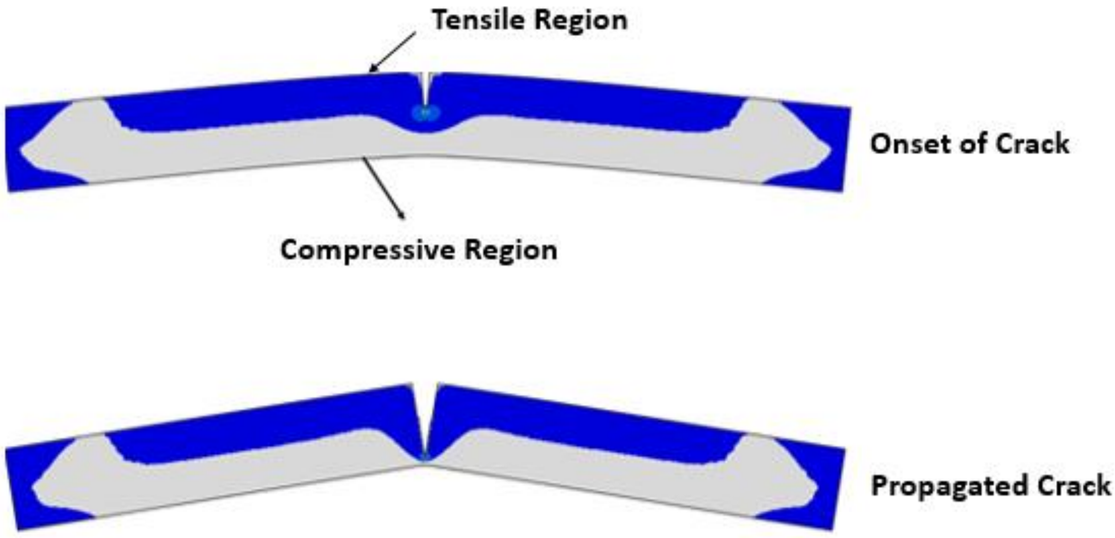

Figure 3.14. Stress field of SENB specimen in FEA model during loading.

In Figure 3.15, progression of crack is shown with detailed views of cracked region. Crack flows a straight path as in the fracture toughness experiments.

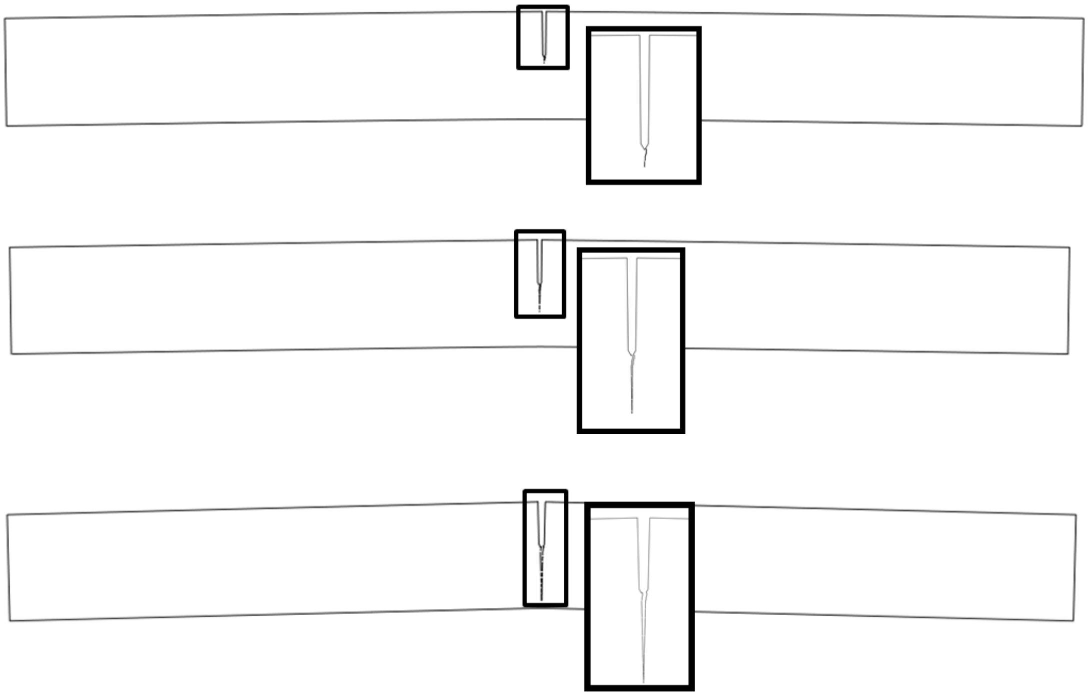

Figure 3.15. The crack propagation on SENB specimen in FEA model during loading.

The load displacement curve for analysis have been obtained in loading direction and provided in Figure 3.16. Also, analysis results were compared with experimental data and they well agreed with. It can be seen from load-displacement curve.

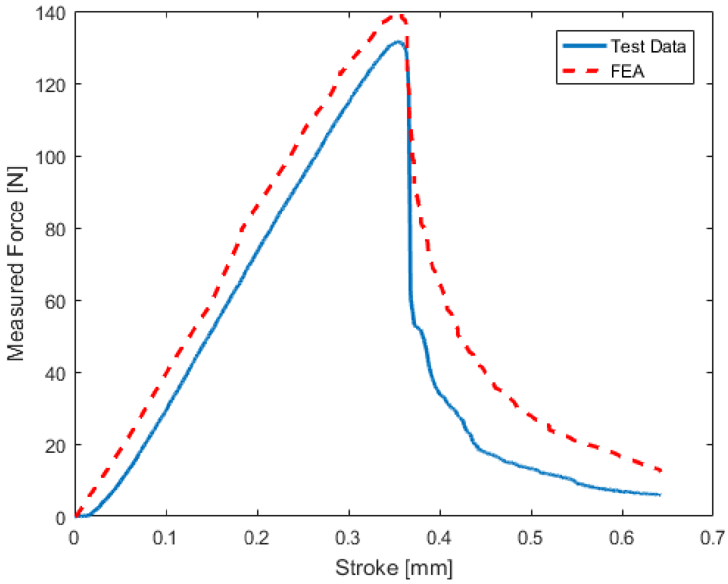

Figure 3.16. Load-displacement curves of FEA model and experiment.

3.3.2. Crack Propagation in an Asymmetrically Notched Beam

3.3.2.1. Problem Description

In this study, it is aimed to illustrate crack propagation in an asymmetrically notched beam with a displacement controlled loading. The solution was obtained using the XFEM module with a USDFLD subroutine. The geometry was taken from [38] where the same geometry was used for observing crack propagation.

3.3.2.2. Geometry and Model

An asymmetrically notched simply supported beam is loaded from mid-point of top edge. A displacement boundary condition in loading direction was defined. The geometry is provided in Figure 3.17. Initial crack length is 19 mm, span is 203.2 mm, width is 76.2 mm, thickness 25.4 mm, and total length of the specimen is 228.6 mm.

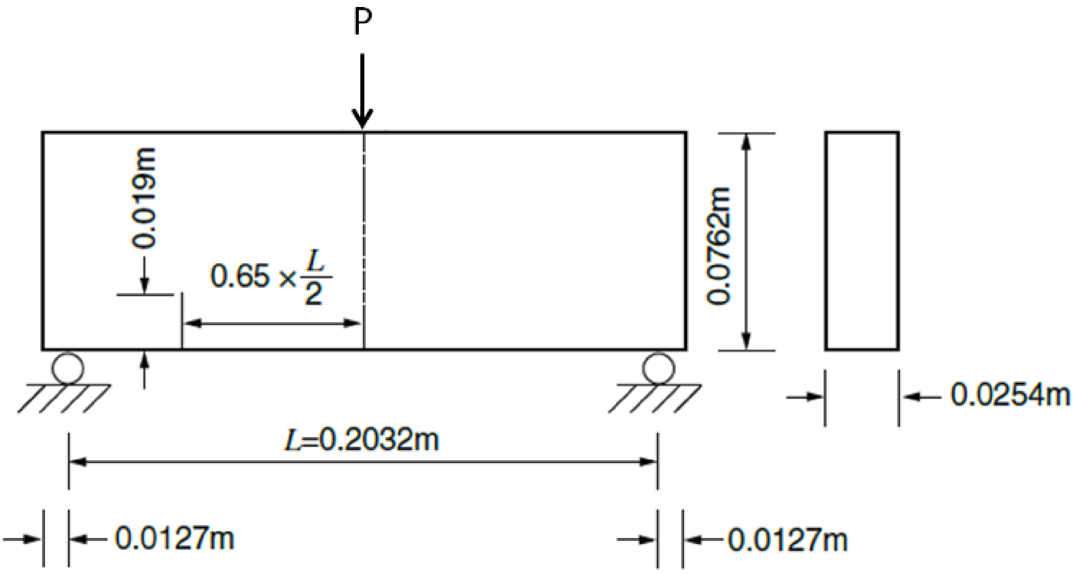

Figure 3.17. Geometry of asymmetrically notched beam, figure taken from [37].

The material properties were selected as same with previous section 3.3.1.3 SENB specimen three-point bending analysis model.

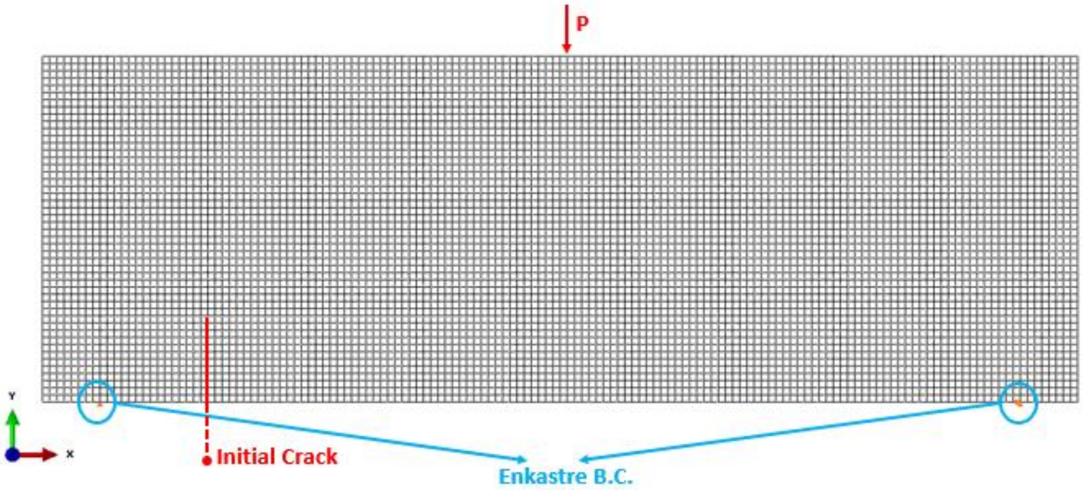

Figure 3.18. The FEA model with boundary and loading conditions.

The FEA model is shown in Figure 3.18 with boundary conditions and generated mesh. About 6900 linear reduced hex plane strain elements were used. The boundary conditions were defined at nodal points. The geometry is held from two bottom points constraining translational and rotational DOFs. 1mm displacement was applied from midpoint on top surface. Maximum principle stress criterion was used for crack initiation and power law was used for damage evolution criterion. Fracture parameters are same with SENB Fracture toughness test model.

3.3.2.3. Results and Discussion

The crack propagation is presented in Figure 3.19 with discrete visuals. The propagation angle of the crack is calculated as 63° which is a good value when compared with John's and Shah's experiment where it was found as 60° [38].

The load condition is a mixed-mode loading, therefore crack propagation will no longer be a straight line. According to Erdogan and Sih [39], crack propagation will be dependent on maximum tangential stress. The crack direction is found by

$$\theta = \cos^{-1}\left(\frac{3K_2^2+\sqrt{K_1^4+8K_1^2K_2^2}}{K_1^2+9K_2^2}\right) \tag{3.21}$$

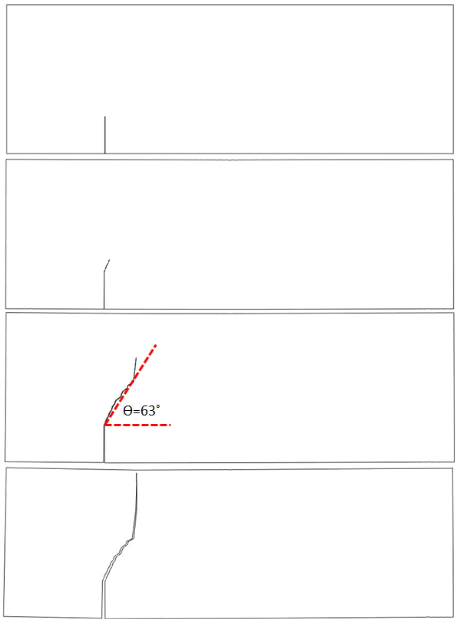

Figure 3.19. The crack propagation on asymmetrically notched specimen.

CHAPTER 4

CRACK INITIATION AND PROPAGATION ANALYSIS OF A GRAPHITE THROAT

The main objective of the study is to gain insight into the structural behavior of the throat. To analyze this structural behavior, first, the fluid flow and the heat transfer aspects of the system should be solved, as the boundary loads and thermal stresses depend on these.

This problem is a coupled one as the fluid mechanics, heat transfer and structural aspects affect each other. However, a fully coupled numerical analysis requires an impractical amount of computational effort and would result in a highly unstable system in terms of convergence. Therefore, in this work, we analyzed the three parts individually, but updated the boundary conditions iteratively until all three parts are in agreement.

A flowchart of the analysis procedure is shown in Figure 4.1. In the first step, the flow was determined by computational fluids dynamics (CFD). The boundary conditions for the CFD analysis comes from the operating conditions of the rocket. CFD results provide the pressure and heat flux on the inner surface of the throat, as a function of axial position. The heat flux distributions constitute the boundary conditions for the second step of the process, which is the transient heat transfer analysis. This analysis solves for the temperature distribution over the nozzle as a function of position and time, T(x,r,t). In the final step, the pressure distribution obtained from the first step and the temperature distribution obtained from the second step were used to perform the structural analysis. Pressure distribution acted as a distributed boundary load on the system and the temperature distribution allowed the calculation of thermal stress induced by thermal expansion.

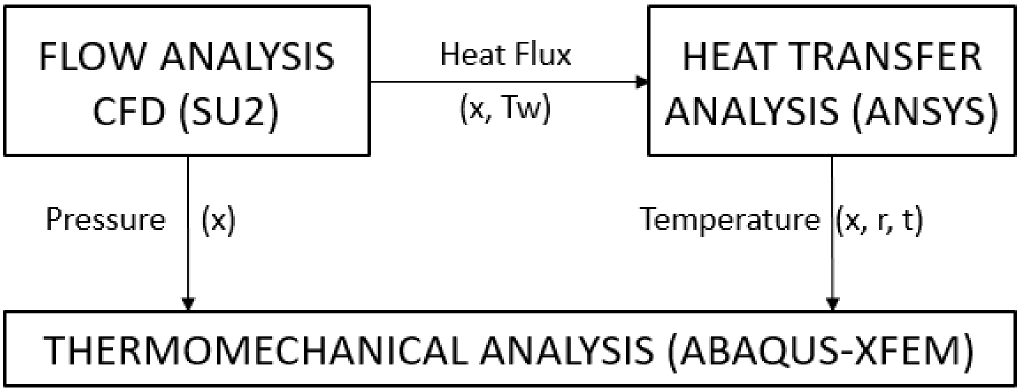

Figure 4.1. Schematic view of analysis procedure of rocket motor nozzle analysis.

4.1. Supporting Analysis: CFD and Heat Transfer Analysis of the Nozzle

CFD analyses and transient heat transfer analysis are required as an input for the thermomechanical structural analysis which is main the subject of this thesis. The analysis was conducted at ROKETSAN by Serhan Donmez [40] and is summarized here for completeness.

4.1.1. CFD Analysis

4.1.1.1. Methodology

The Stanford University Unstructured (SU^2), an open source code [41] is used for the simulations, owing to its capability of solving compressible turbulent flows. A finer mesh is used around the throat region where the flow and temperature gradients are maximum. The gas mixture was modeled as ideal gas mixture and flow was assumed as compressible and viscous with no slip boundary conditions. CFD solution employed Navier-Stokes equations. [41].

4.1.1.2. Geometry and Modeling

Figure 4.2 shows the model domain and the mesh with 1,300,000 unstructured elements. The pressure and temperature boundary conditions at the inlet were 3560 K and 7 MPa, respectively. These values correspond to the steady-state conditions and come from a detailed analysis of the combustion process which is beyond the scope of this thesis.

In the actual operation of the nozzle, the throat temperature gradually increases as a result of the heat flux from the hot flow. The associated heating of the wall temperature will limit the heat flux into the nozzle through convection and radiation. Since a transient coupling of the CFD analysis to the thermal conduction analysis of the whole rocket assembly is not computationally feasible; instead, the flow is repeatedly solved for 5 different wall temperatures ranging from 300 K to 3300 K. This way, the heat flux on the throat inner surface was determined for several wall temperatures, corresponding to the increasing temperature of the throat over time.

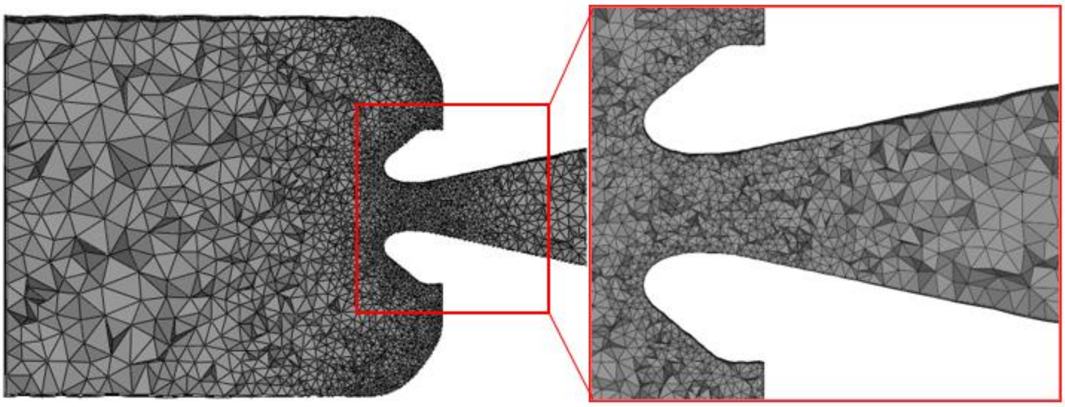

Figure 4.2. Flow field mesh structure of solid propellant rocket nozzle.

The flow boundary conditions were given by considering a combustion chamber of a rocket motor. The input parameters are given in the *Table 4.1*.

Table 4.1. *Input parameters of flow analysis.*

Inlet Temperature [K]	**Inlet Pressure [MPa]**	**Wall Temperature [K]**
3560	7	Ramped in between 300 - 3330 [K]

4.1.1.3. Results and Discussion

The pressure distribution over normalized t distance is presented in Figure 4.3. There is an almost linear variation of pressure value starting from tip of the throat to the end. At the entrance of the throat, where flow speed is minimum, pressure reaches its maximum value, and then it decreases as flow moves over the throat surface. This is expected because in nozzles, highest temperature and pressure occur at stagnation points.

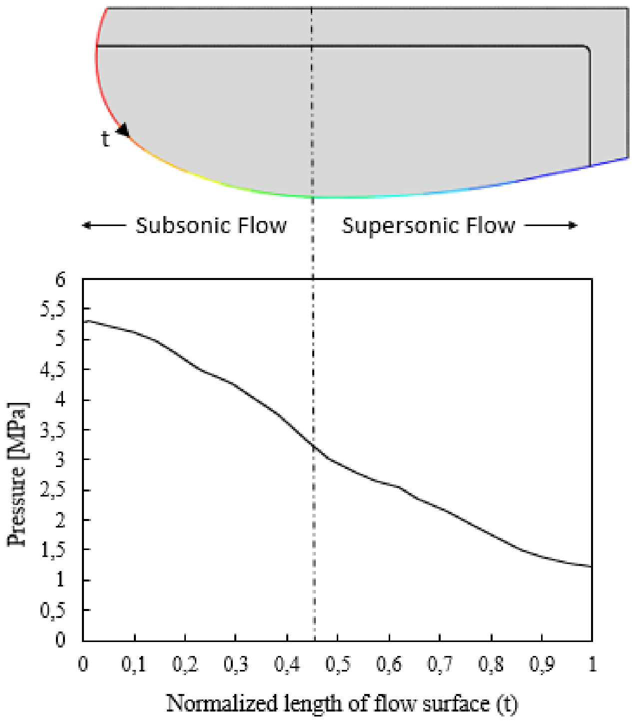

Figure 4.3 Pressure distribution through normalized length of flow surface through “t”.

In addition to pressure distribution, heat fluxes on the flow surfaces were also determined for wall temperature values ramping from 300 K to 3300 K. These heat flux values became input values for the transient heat transfer analysis, to obtain the temperature gradient as a function of position and time.

4.1.2. Finite Element Transient Heat Transfer Analysis

4.1.2.1. Methodology

The transient thermal conduction within the nozzle was solved using ANSYS Parametric Design Language (APDL). The simulation starts with a uniform distribution of room temperature over the whole domain. The flow surface, which is the inner surface of the throat is subjected to time and position-dependent heat flux. On the other hand, the outer surface of the isolator jacket is assumed to be adiabatic. Both silica phenolic and the surrounding structural parts (outside the model domain) have very low thermal conductivity, making this adiabatic assumption a reasonable approximation. Thermal contact resistances were neglected between the throat and isolator jacket based on the same argument.

The heat flux on the flow surface of the throat varies with time and position, due to the increase in the wall temperature. This variation was modeled by a transient heat flux boundary condition over the throat surface. At every time step and for each element, the heat flux is recalculated according to the CFD results, which provides heat flux as a function of wall temperature and time. As CFD data is available for 5 different wall temperatures, interpolation was performed for intermediate values. As the heat flux governed by convection and conduction monotonically and smoothly decreases with increasing temperature, this approach provided a good approximation of the real conditions.

4.1.2.2. Geometry and Modeling

The model consists of 25,000 two-dimensional quad elements. Temperature dependence of thermal conductivity and specific heat of graphite were taken into account in the analysis. Table 4.2 and Table 4.3 list these properties, which are based on experimental measurements performed on specimens of the same graphite and silica phenolic

The simulation was performed for 14 seconds. As will be discussed in the results of the structural analysis, failure occurs in all cases considered within this time frame.

Table 4.2. *Thermal properties of graphite as a function of temperature.*

T [K]	**Specific Heat [J/kgK]**	**Thermal Conductivity [W/mK]**
300	600	70
575	1250	60
675	1350	55
1000	1800	47
1500	2200	41

Table 4.3. *Thermal properties of Silica Phenolic as a function of temperature, table taken from* [9].

T [K]	**Specific Heat [J/kgK]**	**Thermal Conductivity [W/mK]**
300	1005	0.52
575		0.58
675		0.86
875	1256	1.15
1075		1.73

The element type was used as plane 55, 2-D thermal solid elements which is used for heat transfer solutions in APDL [42]. The element shape is demonstrated in Figure 4.4. The meshed geometry for the heat transfer analysis is shown in Figure 4.5. Mesh structure was kept fine to obtain a smooth temperature variation through parts.

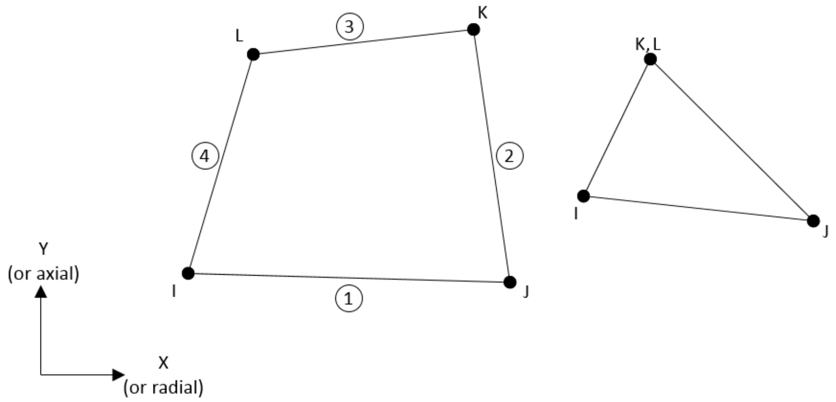

Figure 4.4. Plane 55 element used in transient heat transfer analysis in APDL, figure taken from [42].

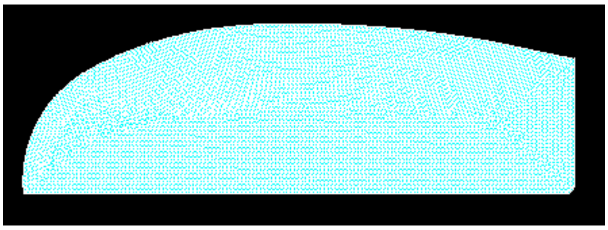

Figure 4.5. Meshed geometry for heat transfer analysis.

4.1.2.3. Results and Discussion

Figure 4.6, shows constant-temperature contours in the throat part at times of 1 s, 5 s, 10 s, and 14 s. As time elapses, heat propagates through the depth of throat. At the same time, surface temperature increases continuously. Since silica phenolic is a good insulator, there are still some regions that stay close to the initial temperature, at 14 seconds. This is an important factor that increases the thermal stresses in the system.

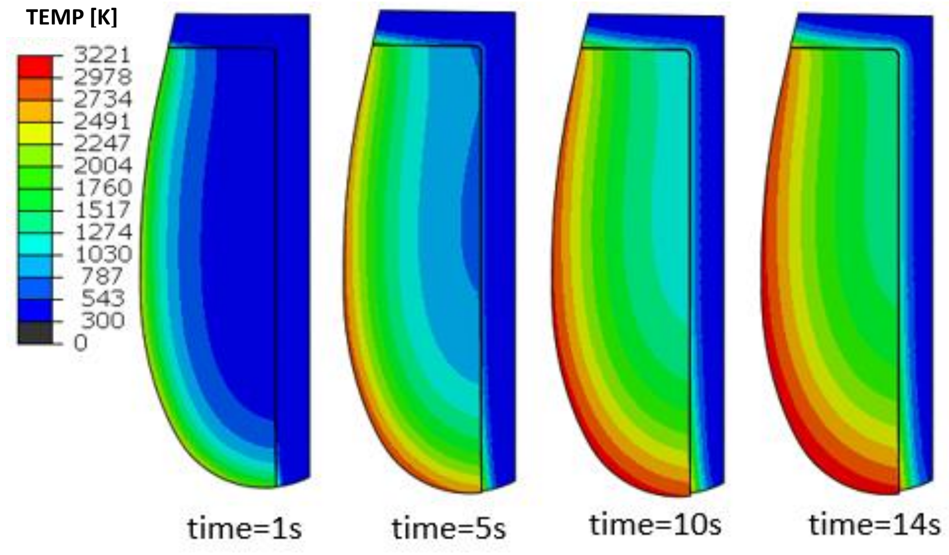

Figure 4.6. Temperature contours for a) 1 second b) 5 seconds c) 10 seconds d)14 seconds.

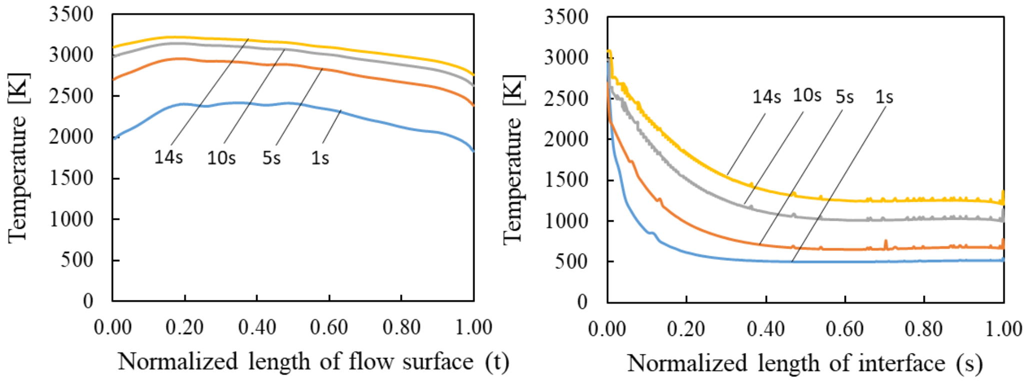

Figure 4.7. Temperature on surface t and surface s for time frames of 1 second, 5 seconds, 10 seconds, and 14 seconds.

Figure 4.7 shows temperature difference between inner and outer surfaces with respect to normalized distances. In Figure 4.7, the temperature variation along t and s surfaces are plotted for different times. Figure 4.7a, shows the surface temperature variation taken in the inner surface (t path) and Figure 4.7b, shows temperature variation taken in the outer surface (s path) of graphite throat. In Figure 4.7, the axes variables are normalized by their actual lengths. Figure 4.6, shows temperature gradient through nozzle, and Figure 4.7 shows temperature difference between inner and outer surface with respect to normalized distances.

Both inner surface and outer surface temperatures rise as time elapses. Furthermore, the temperature differences between each solution decrease with time as the heat flux from the flow to the wall decreases with increasing wall temperature. Besides the variation through the depth of throat, temperature values also decrease along t and s surfaces. Although the temperature gradient decreases with time, the difference is still high enough to cause considerable thermal stresses.

4.2. XFEM Analysis of Crack Initiation and Propagation

4.2.1.1. Methodology

A generic nozzle geometry was selected for the analysis. The geometry was kept simple for enabling a clear interpretation of the results, but it included all the main features of an actual nozzle for being able to obtain a realistic analysis of the problem. The generic nozzle model consists of two parts, the throat and isolator jacket, as shown in Figure 4.8. The throat is made of isotropic Mersen-2020 and the isolator jacket is made of silica phenolic composed of silica fiber (SiO_2) and phenolic resin. Silica phenolic is an ablative material with high thermal insulation, low thermal conductivity and low cost [43]. This two-material assembly is a very common design where graphite provides the high-temperature strength and silica phenolic provides the thermal insulation that keeps the remaining sensitive parts of the rocket isolated from elevated temperatures.

4.2.1.2. Geometry and Modeling

The minimum diameter of the throat ($R_{in,min}$) is 27.75 mm, and the outer diameter (R_{out}) is 47.75 mm. The assembly has a length (L) of 65 mm. $R_{in}(x)$ and $R_{in,min}$ are a critical design parameters that affect thrust force, velocity of the flow at the inlet and the exit, and mass flow rate [44]. In this work, the geometry of the nozzle defined by R_{in} (x) is optimized for the best combination of high thrust, flow stability and combustion efficiency. The optimization was performed through extensive CFD iterations. The details of this process is beyond the scope of the present work and is covered by extensive studies in the literature [45]. On the other hand R_{out} does not directly affect the flow behavior and it is optimized for structural integrity and low weight. In Figure 4.8 radial coordinates (x,r) are defined because of the axisymmetry of the problem. Also, local coordinates t and s are defined, which represent the flow surface (inner surface of throat) and outer surface of throat in Figure 4.8, respectively. In the initial design of the rocket nozzle, there exists a single part of throat insert as bulk material and around it, silica phenolic material was placed as insulator material.

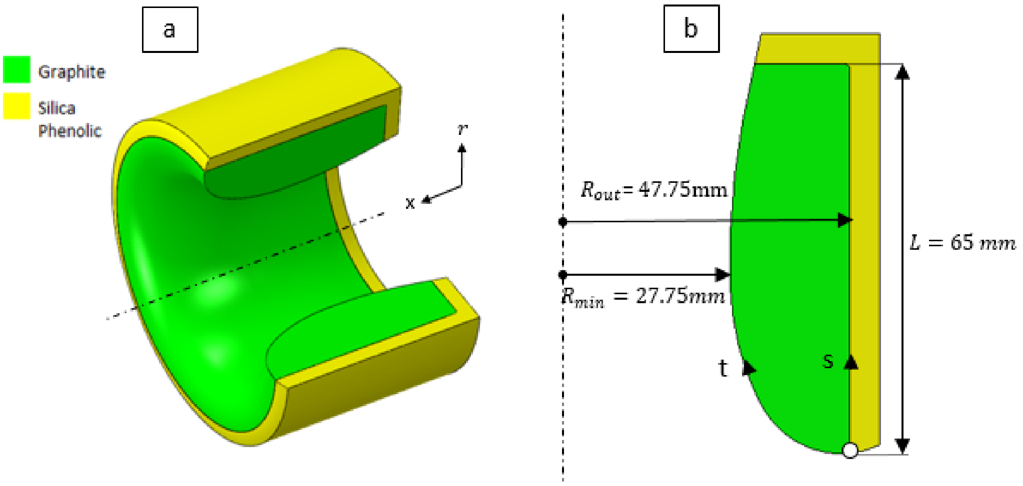

Figure 4.8. a) Isometric and b) axisymmetric view of rocket nozzle throat in thermomechanical finite element model.

The material model of graphite was explained in section 3.3.1.3 previously. In addition to the previous material model, in thermo-mechanical analyses, temperature effect was implemented in USDFLD subroutine. In [26], the elastic behavior of a fine grain ATJ graphite with rising temperature is presented. Graphite gets stiffer as temperature increases, especially after 1200 K. The behavior of elastic modulus of ATJ graphite with rising temperature is illustrated in Figure 4.9. In our study, it is assumed that the stiffening ratio of ATJ graphite with temperature is the same as Mersen-2020. The stiffening ratio is determined by dividing the corresponding elastic modulus at that temperature with an elastic modulus at room temperature. Then elastic modulus values of Mersen-2020 are multiplied with that corresponding stiffening ratio at present temperature. The motivation to use this assumption for Mersen-2020 is the similar elastic modulus behavior between ATJ graphite and Mersen-2020.

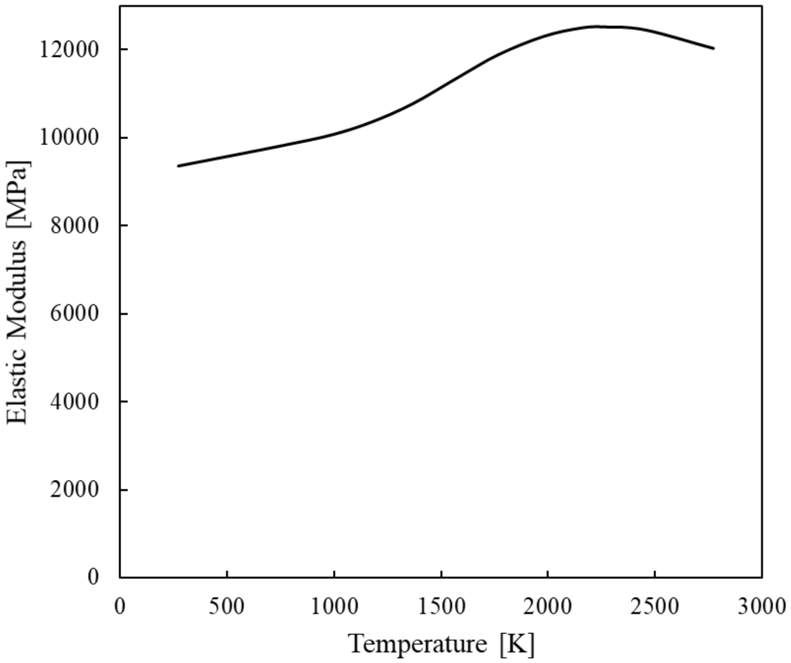

Figure 4.9. Illustration of elastic modulus change of ATJ graphite with rising temperature, figure taken from [26].

ABAQUS commercial finite element code was used for structural analysis with XFEM being used to model crack initiation and propagation.

Figure 4.10 shows the boundary conditions of the model. The isolator-throat assembly is fixed from outside by the supporting structural components of the nozzle. The inner surface of the throat is subjected to an axially varying pressure load, causing stresses within the structure. A second and more dominant source of mechanical stress is the temperature gradients and associated thermal expansions, modeled by the built-in capability of ABAQUS.

In reality, the pressure load reaches steady-state very quickly, whereas temperature evolves throughout the time frame considered, resulting in a gradual increase in thermal stresses. Based on these facts, the pressure load is ramped relatively quickly, such that 90% of the pressure load is reached within about 1 second. An even faster ramp or an abrupt step is avoided to prevent convergence issues. When it comes to thermal stresses, the temperature data from thermal conduction analysis were utilized. Mapping of the temperature data which are available for all time steps, provided incremental inputs to the Finite Element simulation.

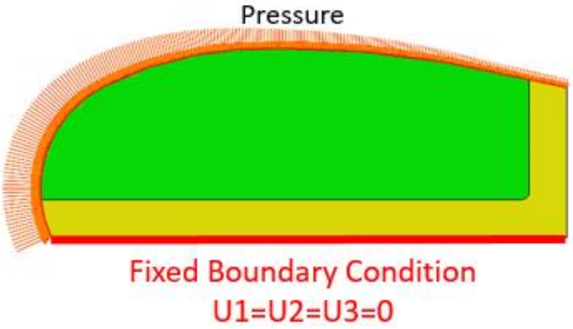

Figure 4.10. Schematic view of the boundary conditions of the model. The arrows indicate the magnitude of pressure over the nozzle surface.

Figure 4.11 shows the geometry of the axisymmetric model together with the mesh structure. The model consists of about 65000 linear axisymmetric CAX4 solid quad elements. Variations in mesh size were kept at a minimum to prevent inaccurate stress gradients. The region shown with the black frame was particularly meshed finely due to a stress concentration spot.

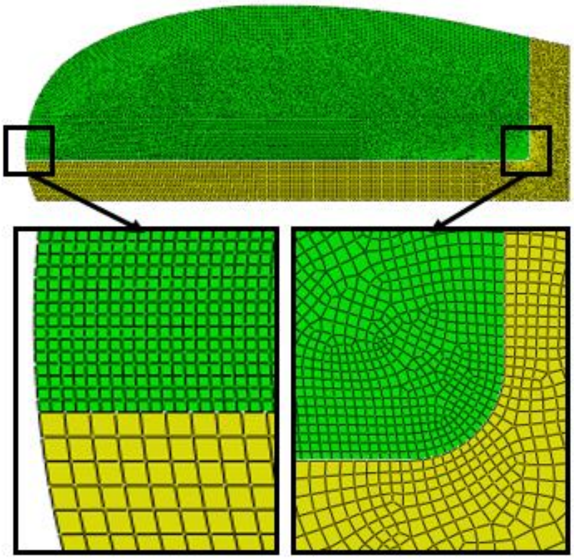

Figure 4.11. Schematic view of the axisymmetric model showing the details of the mesh.

Mesh dependency is a critical parameter for convergence and accuracy of results. The same model was analyzed with different node and element numbers without changing any other parameter to set the mesh size. In Figure 4.12, reaction force at fixed boundary against number of nodes graph is presented to decide mesh size more confidently. According to the figure, when the number of elements is higher than 60000 elements, the solution is independent of mesh size.

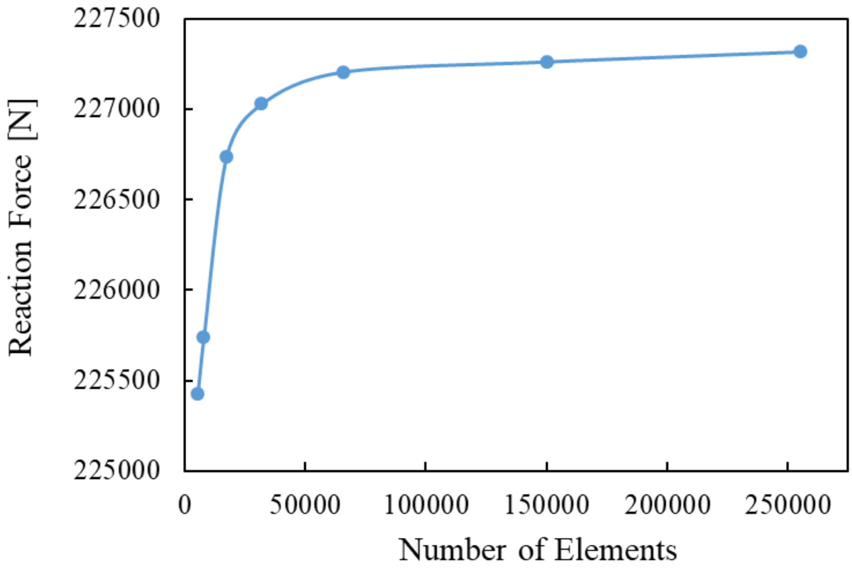

Figure 4.12. Mesh convergence graph of thermomechanical model.

In rocket applications, the throat part is connected with isolator by an adhesive material but its durability against high temperatures is low. By taking this issue into consideration, the joint between the throat and isolator jacket was modeled with a bonded connection (glued interface) and contact connection to observe the effect of interface definition. The illustration of “bonded interface” and “contact interface” models are presented in Figure 4.13.

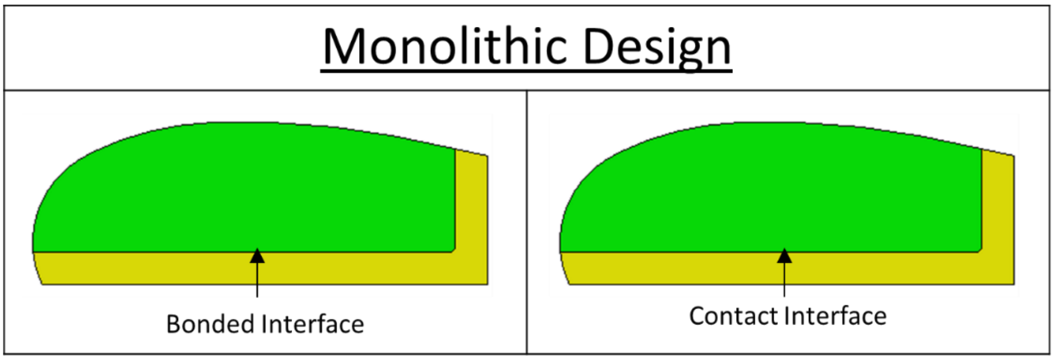

Figure 4.13 Illustration of monolithic design model according to interface definition between throat and isolator jacket.

The contact definition between the instances is established by taking consideration of interaction properties such as tolerance of penetration of elements or friction coefficient. In the model, “penalty” friction formulation which allows little penetration of master nodes was used among interacting surfaces to enhance convergence. The contact stiffness was assumed to be linear. The friction coefficient was determined by an experiment conducted by Liu et.al [16]. They investigated the sensitivity of the coefficient of friction between carbon-based materials and phenolic materials in solid rocket motor nozzles. In a part of the study, they prepared a finite element model and gave reference results for variation of friction coefficient against contact pressure, Von-Misses stress and displacement. Moreover, they had an experiment to measure the friction coefficient against temperature in two cases: with glue and without glue. In the study, it is mentioned that glue is vaporized when the temperature reaches about 250°C. In our case, two data were merged and a friction coefficient graph obtained against temperature. It is given in the Figure 4.14.

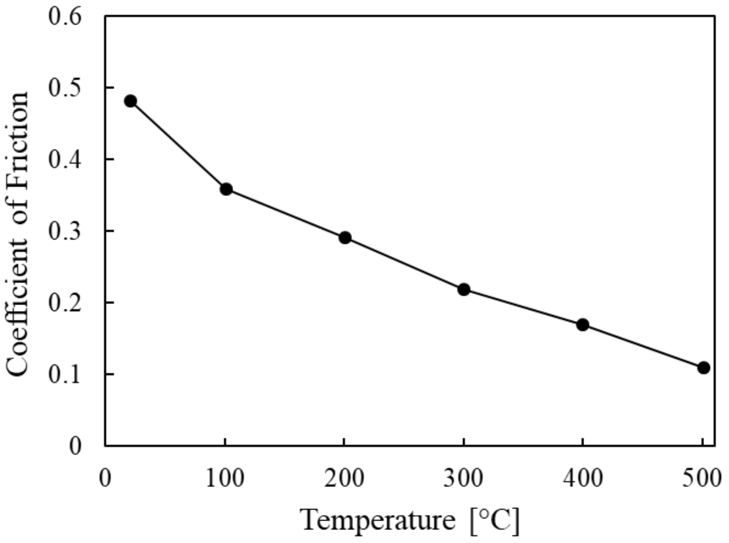

Figure 4.14. Friction coefficient comparison against temperature, figure taken from [16].

4.3. Results and Discussions

Thermomechanical model solution gives the results for combustion conditions of preselected solid rocket motor nozzle. Analysis procedure for the simulation of combustion were given in Chapter 4. The results are provided for t = 5 s, since thermal loads are high enough to cause a crack on throat part within this time frame.

Thermal gradient through the depth of throat varies. This variation causes a non-uniform thermal expansion, which results in rising of thermal stresses over the throat part, especially on the flow surface. Figure 4.15, shows radial displacement of throat starting from flow surface through the depth of throat. Moreover, distributed pressure on the flow surface causes the rising of compressive stresses on the throat. However, pressure loads are not as effective as much as thermal loads on the throat.

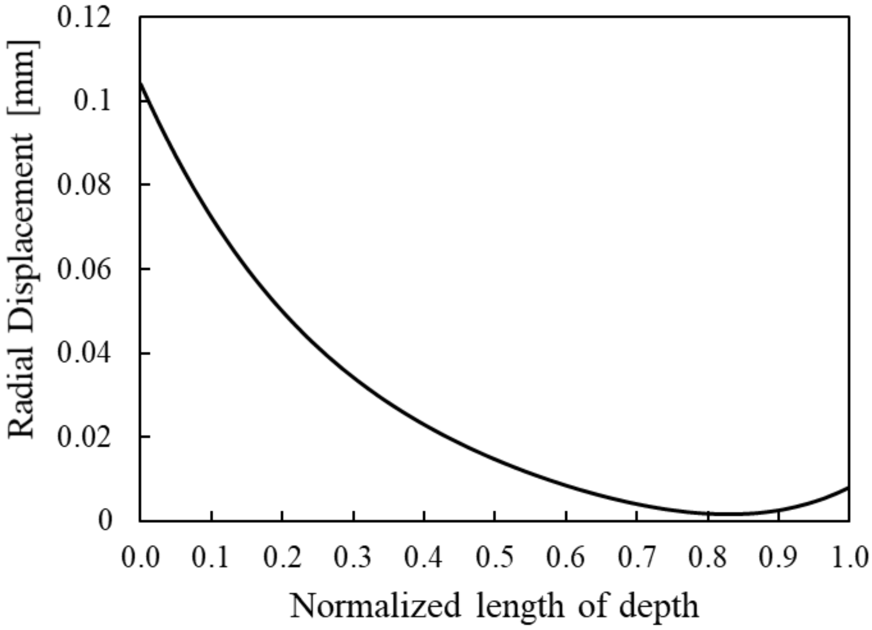

Figure 4.15. Illustration of thermal expansion of throat in radial direction along normalized length of depth.

4.3.1. Analysis of the Monolithic Design

In the following sections, two monolithic designs are compared according to failure occurrence on the part. However, one of the monolithic design models had convergence issues due to discontinuity of the model and could not have a hundred percent solution. Hence, a comparison will be made for minimum solution ratio among single-part throat models. Then, complete solutions will be given for fully converged solutions.

4.3.1.1. Monolithic Design: Case I - Bonded Interface

The principal stress distribution view over throat and isolator jacket besides, detailed crack view of throat near flow surface for contact joint model are provided in Figure 4.16 with a deformed view. Three main cracks initiate and propagate within the throat due to high confinement pressure sourced by pressure on flow surface and thermal expansion of high-temperature regions near the flow surface. The cracks were propagated parallel to the flow surface to both sides till it kinks from a surface or stays still without changing its direction. This occurs when Mohr-Coulomb failure index overs unity. In literature, these type of cracks is called shear cracks or mode-II cracks [46]. Confining pressure on crack surfaces causes to decrease of tensile stresses and leads to shear mode crack growth in the direction of maximum shear stress. Tensile stresses occur in a very small region at the crack tip. Usage of the Mohr-Coulomb criterion enabled the parallel crack occurrence in a shear plane near the flow surface of the throat. The shear stress plane elongates on a very close region to flow surface where compressive stresses are highly dominant and diminish towards end throat. In the same region, parallel cracks kinks towards to surface and the cracked part is separated. According to [47] large compressive stresses appear in early stages of heating since steady thermal stresses are quite lower than transient thermal stresses as in the early stage of firing in a nozzle. In the analysis, cracks emerge in the early stage of firing where the temperature did not reach its maximum value.

The analysis model has completed 70% of the full solution and it has already fracture from the flow surface and almost fractured from the bottom of the flow surface. This cracking will lead to disruptions on the flow surface which causes to disturbing of flow aerodynamics.

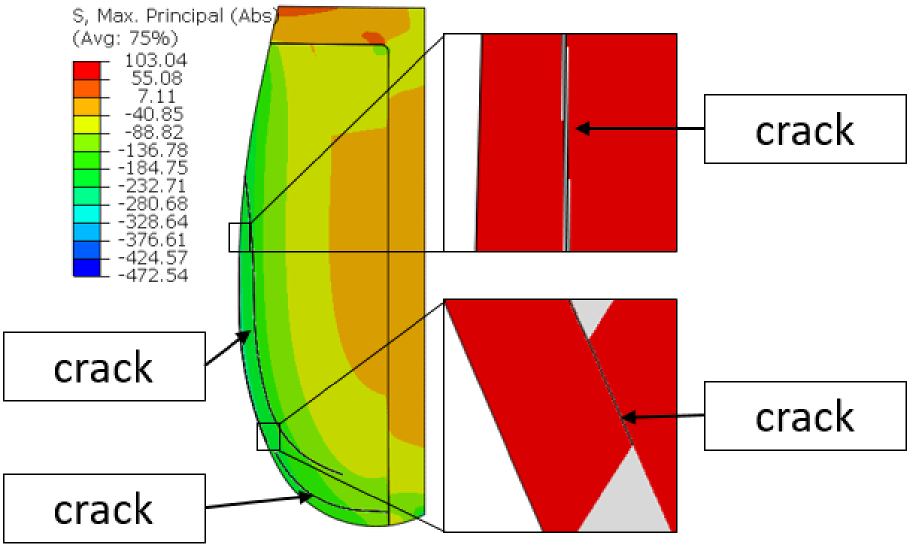

Figure 4.16. Contour view of principal stress distribution and detail crack view of bonded joint model from different regions on throat part.

4.3.1.2. Monolithic Design: Case II - Contact Interface

Figure 4.17, shows the principal stress distribution and detailed view of cracks in the monolithic design analysis model with contact definition. Contact interface model has completed a fully converged solution. For the sake of model comparison, solutions of 70% and 100% of fully converged solution is given separately.

On a region near flow surface, three parallel cracks initiate and propagate in both sides by keeping its parallelism then kinks through surface as in bonded interface model. Flow surface has been corrupted hence it will fail in providing predetermined thrust load due to disturbed flow. Length of cracks, their position and paths are similar with bonded interface model. Hence, it can be concluded that vaporization of glue on interface between throat and isolator jacket does not affect failure mechanism in monolithic design.

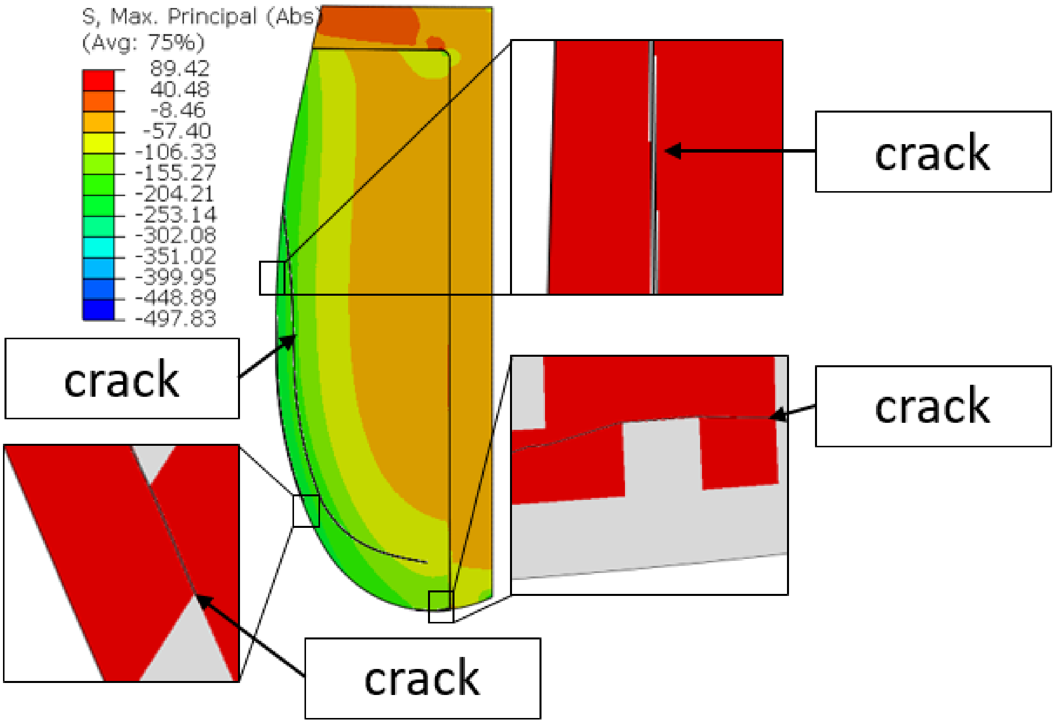

Figure 4.17. Contour view of principal stress distribution and detail crack view of contact joint model from different regions on throat part (70% of fully converged solution).

Figure 4.18, shows principal stress distribution and detailed crack view of contact interface model fully converged solution. At the end of full loading, it is seen that cracks are reached to interface between throat and isolator jacket. In this way, a big part of throat breaks off so it results with failure of rocket nozzle. To sum up the failure mechanism in one-part throat model, cracks initiate a region where close to flow surface and propagate in mode II as parallel to flow surface. The effective stresses are shear stresses as predicted in Mohr-Coulomb failure criterion. In one of cracks, it grew downward through interface between throat and isolator jacket. Finally, a considerably big piece of throat broke off and it probably causes to a catastrophic failure.

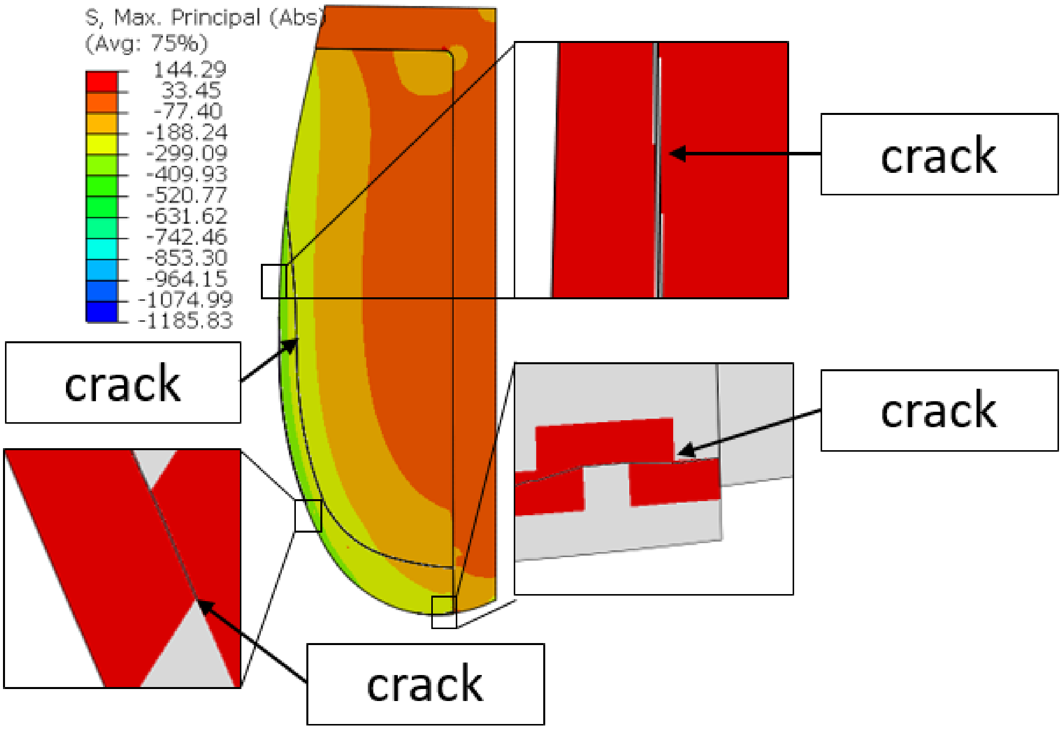

Figure 4.18. Contour view of principal stress distribution and detail crack view of contact interface model from different regions on throat part (fully converged solution).

In [46], failure on railways is demonstrated due to high contact load applied on rail surface during passing of train wheels. It occurred due to high confinement pressure on railway surfaces during contact with train wheel. This failure is similar to rocket nozzle surface cracks because high shear stresses emerge within throat and cause shear mode cracks which propagates through surface and cause failure. Figure 4.19 shows parallel crack occurrence near surface due to high confinement pressure and failure due to breaking of railway piece.

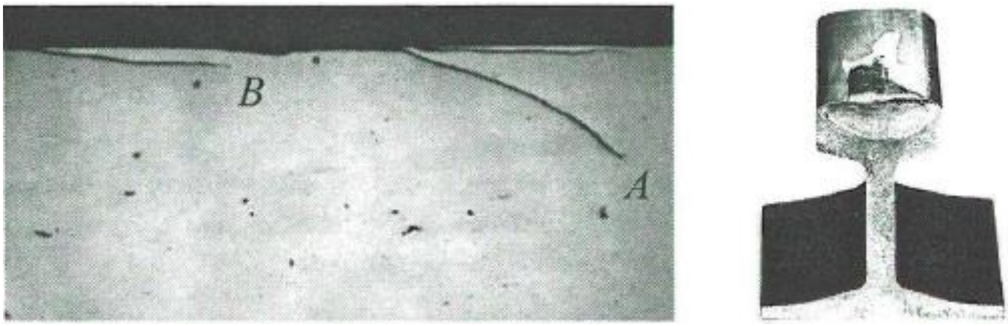

Figure 4.19. a) A crack propagates parallel to surface (B) and a crack propagates downward to railway (A). b) Catastrophic failure of railway due to break off a large piece of railway, figure taken from [46].

4.3.2. Partitioned Designs

4.3.2.1. Design-1 Overview

In a NASA report [2], it is mentioned that graphite nozzle throats were fractured due to excessive thermal loads during combustion of rocket nozzle. As a solution, nozzle inserts were separated into cylindrical washers whose cross sections are rectangles, as shown in Figure 4.20. Main idea was to minimize the initial length of the part in order to decrease thermal stresses due to thermal expansion.

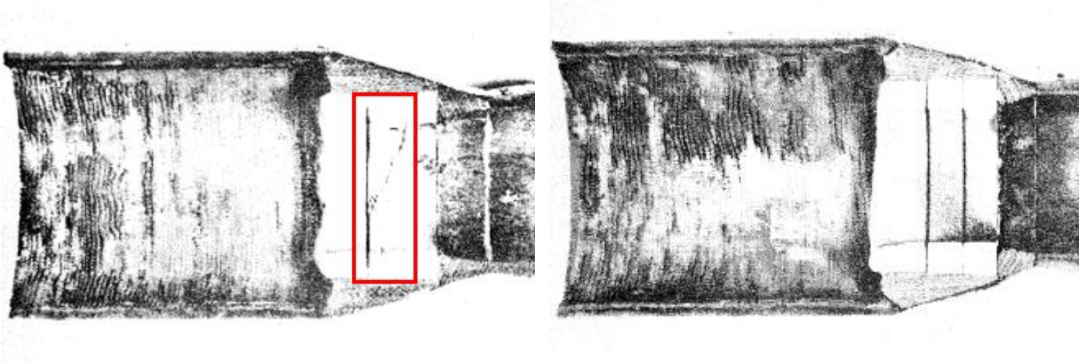

Figure 4.20. Nozzle with circumferential crack in graphite section and segmenting graphite throat into rings to prevent thermal cracks, figure taken from [2].

Partition of the throat reduced the thermal stresses and prevented occurrence of cracks on flow surfaces since axial elongation due to high temperature decreased with decreasing initial length. On the other hand, the gap between washers is an issue to be dealt with. If the gap is too narrow, then parts will have contact with each other and apply pressure on contact interface. This can cause initiation of cracks on contact interface. Otherwise, if gap is too wide, then flow leaks to gap between throat parts and cause to overheating of segments. In the study of [43], it is stated that maximum gap width should be less than 0.25 mm to prevent leaking.

In order to investigate straight partition effect in thesis study, throat was segmented into three parts and analyzed under same conditions with one-part throat model. Moreover, to observe the effect of gap size, two designs were modeled. In the first design, there was no gap among throat segments. In the second design, throat segments were divided with 0.2 mm gap size. The illustration of design-1 throat model is shown in Figure 4.21.

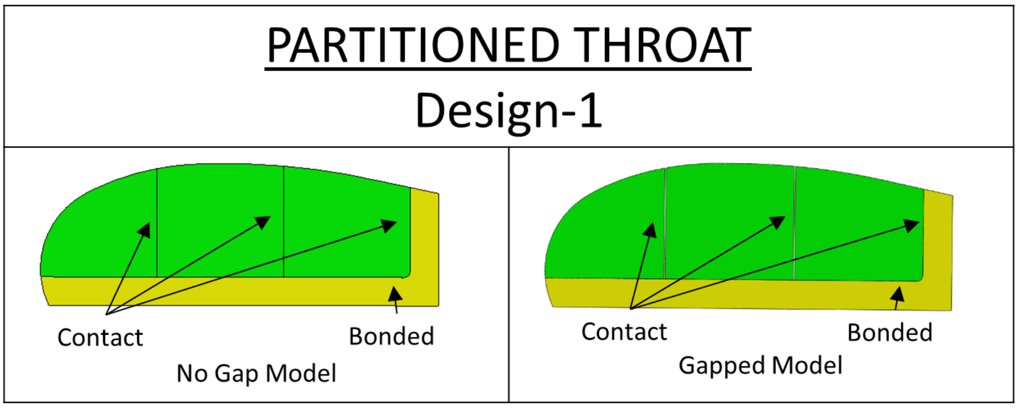

Figure 4.21 Illustration of design-1 throat model according to gap size between segments of throat parts

4.3.2.2. Design-1 with No Gap

Figure 4.22 shows principal stress distribution and detail crack view on straight-partitioned throat part. The model has a fully converged solution and the stress levels decreased when compared to one-part throat model. According to analysis results, a long mode II crack initiated a region very close to flow surface and propagated as parallel. Crack initiated from contact interface between middle and front segments of throat and enhanced as shear crack to both sides. One tip kinked from flow surface a region where near to back segment. The other tip propagated downward in a path that is parallel to flow surface and it reached to interface between throat and isolator jacket. Although width of crack is small, a long piece broke off from flow surface and it would cause to disturbance of flow. Moreover, there are two small cracks on back segment of throat. One is on the flow surface which was initiated from contact interface between middle and back segments of throat, the other one is on the interface between throat and isolator which again initiated from contact interface between middle and back segments.

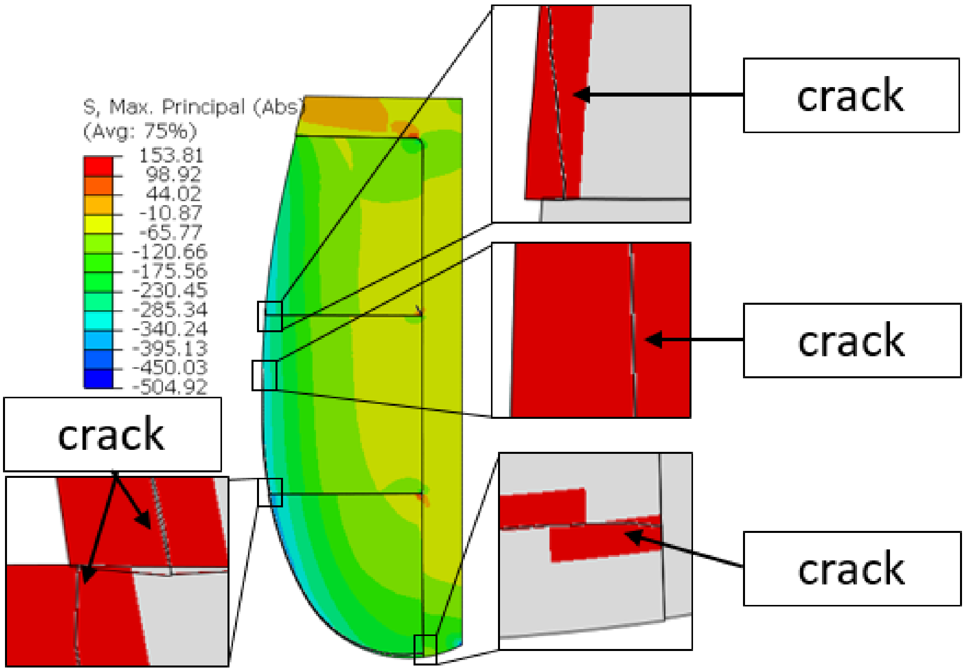

Figure 4.22. Principal stress distribution and detailed crack view of design-1 with no gap.

Although, a flake flew away from flow surface, damage in straight partitioned model with no gap is a progress in preventing fracture in rocket nozzle throat when compared to damage in monolithic design. Firstly, there is no a large piece which breaks of from throat. Secondly, stress levels decreased to half of monolithic design stress level. On the other hand, stress distribution over throat did not change considerably due to lack of gaps between segments. The stress relief occurred due to sliding of throat segments on each other and initial length of throat is divided into three.

4.3.2.3. Design-1 with Gap

In Figure 4.23, principal stress contours and detailed view of cracks are shown for design-1 model with gap. Two of cracks initiated from contact interfaces between front and middle segments of throat. One of them propagated as parallel to flow surface on middle segment as mode II crack and it kinked to flow surface and left a flank which might cause to disturbing of flow on middle segment aerodynamic surface. Other one enhanced as parallel to flow surface on front segment initially, then it changed its direction downwards. At the end it reached to interface on outer surface of throat and it would cause a big piece to break off from segment. Furthermore, at the entrance of front segment, a shear crack caused a flake on flow surface.

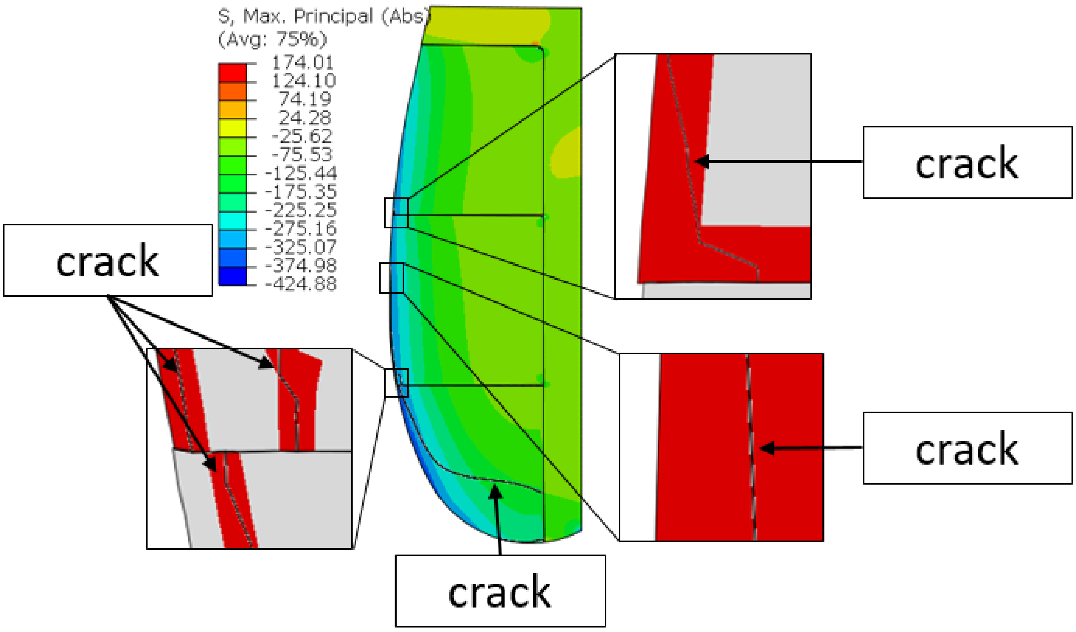

Figure 4.23. Principal stress distribution and detailed crack view of straight-partitioned model with gap.

4.3.3. Design-2 Overview

Another partitioning design strategy to decrease thermal stresses over throat is Z-partitioned throat. In this model, throat was segmented into four parts with two parallel lines in radial direction and one horizontal line which is perpendicular to parallel lines. In order to investigate gap effect, two models were created. In the first one, there is no gap between segments of throat. On the other hand, in the second one there is a 0.2 mm gap between segments. Interface between segments of throat, besides, vertical interface between back segment and isolator jacket have a contact definition, and interface between throat and isolator jacket has bonded contact definition. Figure 4.24, illustrates design-2 model according to gap size between segments of throat.

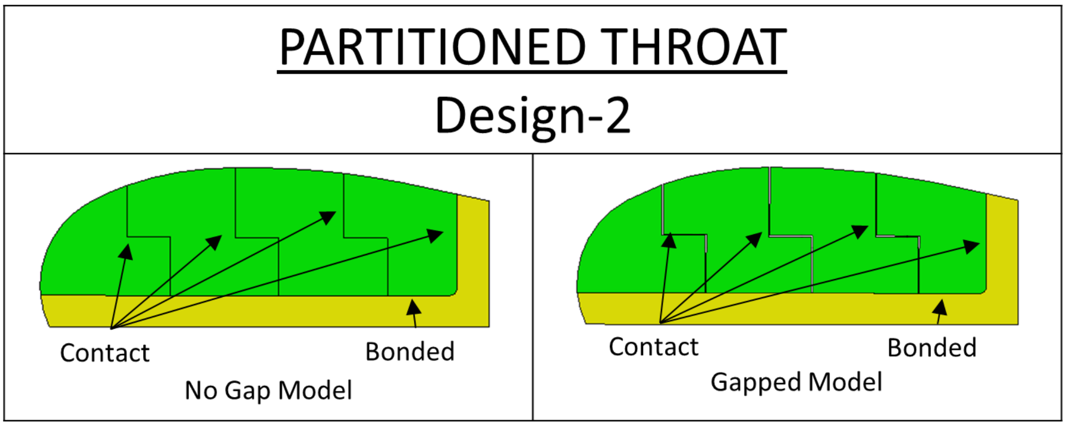

Figure 4.24. Illustration of design-2 throat model according to gap size between segments of throat parts.

4.3.3.1. Design-2: No Gap

Figure 4.25, shows principal stress distribution and detail crack view of throat part for design-2 with no gap. Four main cracks initiated within front and middle segments of throat. The first crack is a shear mode crack and it propagated as parallel to flow surface. It initiated from contact interface between front and middle segment of throat and propagated in both sides till kinking to flow surface from both sides. The crack is driven by shear stresses emerging due to high confinement pressure on flow surface. The second crack is on the middle segment of throat. It initiated from contact interface between front and middle segment of throat as shear mode crack and propagated through back segment of throat at kinked to flow surface by breaking off a large piece of throat. The third crack is on the front segment of throat at the entrance of the nozzle. Crack initiated a region close to flow surface and enhanced downward to interface between throat and isolator. When crack reached interface, a flake occurred on flow surface. This also would disrupt the aerodynamic surface of flow. The forth cracks are wing cracks as shown in blue rectangle frame and they initiated from contact interface between front and middle segment of throat. One of them propagated upwards and other one propagated downwards. Wing cracks are secondary cracks at the tip of shear cracks under tensile stresses. Under high confinement pressure loads, cracks cannot create a king extending under mode I, but if main crack surfaces slide on each other, tensile stress regions emerge at crack tips [47]. Then secondary cracks initiated from main crack with an angle and change cracks direction. In Figure 4.25, contact interface between front and middle segments in rectangle frame behaved like a shear crack.

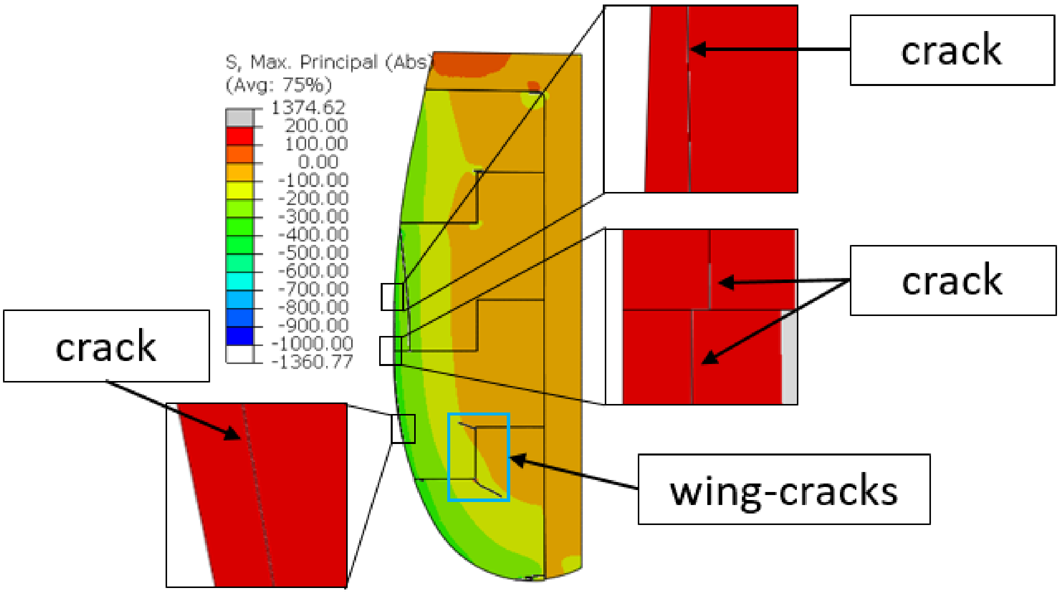

Figure 4.25. Principal stress distribution and detailed crack view of design-2 model with no gap.

Among the four cracks, only wing cracks stayed within the part and did not cause to failure. Other three cracks would cause to damage on aerodynamic flow surface so as disturbance of flow. Furthermore, maximum stress levels are almost 3 times of straight partitioned crack and 1.3 times of one-part throat design.

4.3.3.2. Design-2: with Gap

Figure 4.26, shows principal stress distribution and detail crack view of throat part for design-2 models with gap. Three main cracks initiated within throat part. The first crack initiated on middle segment of nozzle initiated from contact interface between front segment and middle segment of throat. It propagated as parallel to flow surface through next segment of throat. At the end of mode II crack, branches of cracks occurred. The second crack initiated on front segment of throat from contact interface between front and middle segment of throat. It followed a circular path and reached to contact interface between front and middle segments. The third crack initiated on back segment of throat towards depth of throat and it stayed within the part.

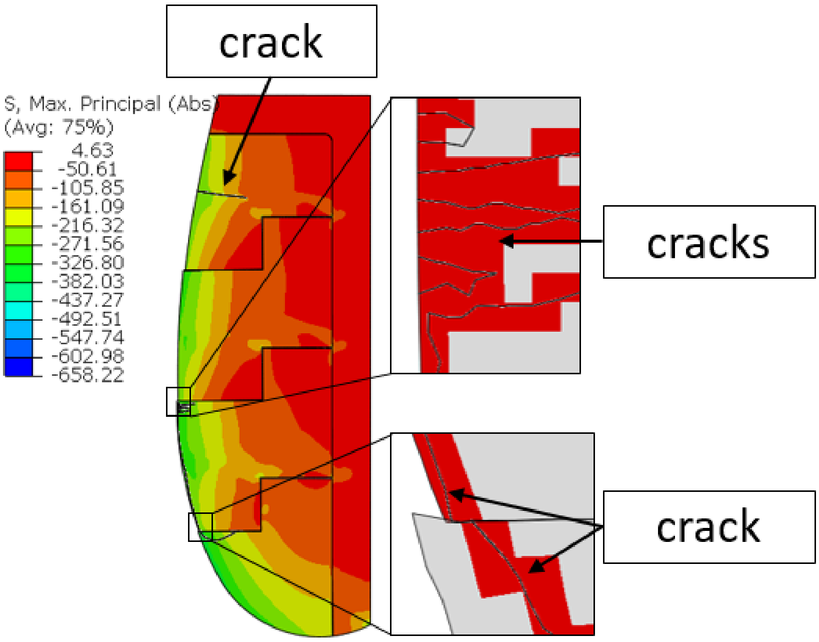

Figure 4.26. Principal stress distribution and detailed crack view of design-2 model with gap.

The cracks like second and third are not as harmful as cracks creating flakes on flow surface. As mentioned before keeping flow surface integrity is the primary goal of a designer to achieve predetermined thrust force.

In all design flake occurrence on flow surface could not be prevented due to high compressive stresses on surface. In very short time, compressive stresses reach to strength limit in all design configurations. However, the length of flake decreased with partitions in comparison with monolithic design. Moreover, shortest flake length has been seen in design-2 with gap model. Based on crack behavior, increasing segment number in throat will decrease the length of flake more.

CHAPTER 5

CONCLUSIONS AND FUTURE WORK

5.1. Conclusions

This thesis demonstrated a three-step numerical modeling of a rocket motor nozzle. This approach reduced computational cost and provided reasonable results. The obtained results in this study will be helpful to design more durable nozzles with against the harsh operating environments.

In the investigation of the fracture behavior of graphite, modeling the material is of great high importance to determine the general behavior of the nozzle throat. For this purpose, thermal and structural material characterization experiments were conducted. These experiments also provided a clearer understanding of the material behavior. The bimodular behavior of graphite was quantified, which is known to change the stress state during the finite element solution. In addition to bi-modularity, elastic modulus was modeled to be dependent on strain and temperature, for further improving the accuracy.

Consideration of manufacturing and assembly conditions provided more reliable results for the fracture behavior of graphite. The existence of a gap between contacting parts created a difference in the results. On the other hand, using bonded interfaces vs. contact interfaces among isolator part and throat had almost no influence on fracture behavior of model as initiation of cracks start near the flow surface of the throat due to the high compressive stresses.

Mohr-Coulomb fracture criterion was implemented to analyze shear mode cracks, which could not be detected with maximum principal stress criterion. However, using solely the Mohr-Coulomb criterion may cause the overlooking of opening mode cracks. For a better investigation, using both criteria were considered, which provided useful information about the type of cracks that can emerge.

Using partition strategies helped reduce stresses and diminish crack lengths and sizes compared to the monolithic design. Although partitioning did not prevent the occurrence of parallel cracks on the flow surface, it delayed the occurrence and decreased their extent. The main issue in partitioned models was that the cracks initiated due to the contact forces between segmented parts upon thermal expansion. Increasing gap size might prevent the contacting of throat segments, but at the same time it might lead to a flow leak which would be catastrophic for the nozzle.

In a rocket nozzle throat, shear mode cracks can cause damage to the flow surface of the throat and the desired thrust cannot be achieved due to the resulting irregular flow. The main reason for the occurrence of shear mode II cracks was the high confinement pressure due to the high thermal gradient. Therefore, choosing a material with higher compressive strength or higher material conductivity can increase the durability against nozzle operational conditions.

5.2. Future Work

In this study, crack growth mechanisms for a monolithic throat design and two partitioned throat designs were studied. In future work, these studies should be extended to additional partitioning strategies to further delay the crack initiation and propagation. In addition to the partitioning geometry, optimum gap size is another parameter that requires further investigation and optimization.

As the presented study has established a systematic framework for the analysis of nozzle failure, the same analysis can be directly extended to other materials commonly used in nozzles. Such studies will provide further insight into the advantages and disadvantages of each material.

Although the presence of cracks is known through the observation of the rocket nozzles after operation, there exists very limited knowledge about the exact thermomechanical conditions during the operation. An experimental setup to simulate the throat behavior under operational loads and temperatures would be a very useful approach for a better understanding of the fracture mechanisms involved.

CHAPTER 6

REFERENCES

[1] J. C. Thomas, J. M. Stahl, A. J. Tykol, F. A. Rodriguez, and E. L. Petersen, “Hybrid Rocket Studies Using HTPB / Paraffin Fuel Blends in Gaseous Oxygen Flow,” in *7th European Conference for Aeronautics and Space Sciences(EUCASS)*, 2015, pp. 1–13.

[2] *Solid Rocket Motor Nozzles*, no. 8115. Washington, D.C.: NASA, 1975.

[3] J. R. Johnston, R. A. Signorelli, and J. C. Freche, “Performance of Rocket Nozzle Materials With Several Solid Propellants,” 1966.

[4] P. Lapp and B. Quesada, “Analysis of solid rocket motor nozzle,” in *AI AA/SAE/ASM E/ASE E 28th Joint Propulsion Conference and Exhibit*, 1992.

[5] *Modeling Fracture and Failure with Abaqus*, Dassault Systèmes, 2012.

[6] A. R. Gomaa and H. Huang, “Thermo-structural Analysis of Steel-Composite Wall Nozzle,” *Int. J. Model. Optim.*, vol. 6, no. 5, pp. 261–267, 2016.

[7] Y. Wang, Q. Wang, H. Chen, J. Sun, and L. He, “Comparative study on crack initiation and propagation of glass under thermal loading,” *Materials (Basel).*, vol. 9, no. 10, 2016.

[8] W. Yu and D. Crane, “Finite Element Simulation of Solid Rocket Booster Separation Motors During Motor Firing,” Cape Canaveral, Florida, 2014.

[9] L. Sun *et al.*, “Crack cause analysis of a graphite nozzle throat insert,” *Acta Astronaut.*, vol. 137, no. April, pp. 70–77, 2017.

[10] D. Liu, B. Gludovatz, H. S. Barnard, M. Kuball, and R. O. Ritchie, “Damage tolerance of nuclear graphite at elevated temperatures,” *Nat. Commun.*, vol. 8, no. May, pp. 1–9, 2017.

[11] P. C. Gope, S. P. Sharma, and A.K. Srivastava, “Prediction of crack initiation direction for inclined crack under biaxial loading by finite element method,” *J. Solid Mech.*, vol. 2, no. 3, pp. 257–266, 2010.

[12] R. C. Mehta, K. Suresh, and R. N. Iyer, “Thermal stress analysis of a solid rocket motor nozzle throat insert using finite element method,” *Indian J. Eng. Mater. Sci.*, vol. 5, no. October, pp. 271–277, 1998.

[13] J. H. Kim *et al.*, “Evaluation of thermal shock strengths for graphite materials using a laser irradiation method,” *Mater. Sci. Eng. A*, vol. 387–389, no. 1-2 SPEC. ISS., pp. 385–389, 2004.

[14] R. R. Kumar, G. Vinod, S. Renjith, G. Rajeev, M. K. Jana, and R. Harikrishnan, “Thermo-structural analysis of composite structures,” *Mater. Sci. Eng. A*, vol. 412, no. 1–2, pp. 66–70, 2005.

[15] G. Sivakumar and V. B. Maji, “Simulation of crack propagation in rocks by XFEM,” in *Recent Advances in Rock Engineering (RARE 2016) Simulation*, 2016, no. Rare, pp. 291–296.

[16] Q. Liu, Z. Sheng, H. Shi, H. Chen, and J. Gu, “Investigation on friction coefficient between Solid Rocket Motor nozzle throat components,” in *ICRMS’2011 - Safety First, Reliability Primary: Proceedings of 2011 9th International Conference on Reliability, Maintainability and Safety*, 2011, pp. 288–292.

[17] S. Phongthanapanich and P. Dechaumphai, “Adaptive Delaunay triangulation with object-oriented programming for crack propagation analysis,” *Finite Elem. Anal. Des.*, vol. 40, no. 1, pp. 1753–1771, 2004.

[18] B. M. Strauss and W. H. Cullen, *Fractography in Failure Analysis*. Philadelphia: American Society for Testing and Materials, 1978.

[19] S. Nambu and M. Enoki, “Strength and Toughness of Graphite Materials for Solid Rocket Motor,” *Mater. Sci. Forum*, vol. 449–452, pp. 709–712, 2009.

[20] A. Fernández-Canteli, L. Castañón, B. Nieto, M. Lozano, T. Holušová, and S. Seitl, “Determining fracture energy parameters of concrete from the modified compact tension test,” *Frat. ed Integrita Strutt.*, vol. 30, pp. 383–393, 2014.

[21] T. Burchell, D. Erdmann III, R. R. Lowden, J. Hunter, and C. Hannel, “The Fracture Toughness of Nuclear Graphite Grades,” Oak Ridge, 2016.

[22] A. Bhushan and S. K. Panda, “Experimental and computational correlation of fracture parameters KIc, JIc, and GIc for unimodular and bimodular graphite components,” *J. Nucl. Mater.*, vol. 503, pp. 205–225, 2018.

[23] B. Gross and J. E. Srawley, “Nasa technical note stress intensity factors by boundary collocation for single edge notch specimens subject to splitting forces,” Cleveland, Ohio, 1966.

[24] R. Saito, Y. Kondo, Y. Koike, K. Okamoto, T. Suzumura, and T. Abe, “Noble high thermal conductivity, low thermal expansion Cu-Cu2O composite base plate technology for power module application,” *IEEE Int. Symp. Power Semicond. Devices ICs*, pp. 51–54, 2001.

[25] “Standard Test Method for Compressive Strength of Carbon and Graphite,” *ASTM B. Stand.*, pp. 1–3, 2015.

[26] U. C. C. Inc., *The Industrial graphite Engineering Handbook*. Parma, OH: High Tech High Temp.

[27] L. Green, “High Temperature Compression Tests on Atomic Energy American,” Downey, California, 1952.

[28] “ASTM E111-04: Standard Test Method for Young ’ s Modulus, Tangent Modulus, and Chord Modulus,” vol. 04, no. Reapproved, pp. 4–10, 2010.

[29] “Standard Test Method for Determination of Fracture Toughness of Graphite at Ambient Temperature,” *ASTM B. Stand.*, vol. 11, no. Reapproved 2015, pp. 1–9, 2011.

[30] J. Barsom and S. Rolfe, *Fracture and Fatigue Control in Structures: Applications of Fracture Mechanics, Third Edition*. 1999.

[31] C. T. Sun and Z.-H. Jin, “Energy Release Rate,” in *Fracture Mechanics*, vol. 0, C. T. Sun and Z.-H. Jin, Eds. Academic Press, 2012, pp. 77–103.

[32] S. T. Kyaw, I. A. Jones, and T. H. Hyde, “Simulation of failure of air plasma sprayed thermal barrier coating due to interfacial and bulk cracks using surface-based cohesive interaction and extended finite element method,” *J. Strain Anal. Eng. Des.*, vol. 51, no. 2, pp. 132–143, 2016.

[33] Belytschko, T., Black, T. “Elastic crack growth in finite elements with minimal remeshing.” *International Journal for Numerical Methods in Engineering*, Vol. 45, No. 5, 1999, pp. 601-620, 1999.

[34] J. M. Melenk and I. Babuška, “The partition of unity finite element method: Basic theory and applications,” *Comput. Methods Appl. Mech. Eng.*, vol. 139, no. 1–4, pp. 289–314, 1996.

[35] T. Belytschko, N. Moës, and J. Dolbow, “A finite element method for crack growth without remeshing,” *Int. J. Numer. Methods Eng.*, vol. 46, no. 1, pp. 131–150, 1999.

[36] ABAQUS Inc, *Analysis User’s Manual*, vol. I. Providence, RI: Dassault Systèmes, 2011.

[37] ABAQUS Inc, *User Subroutines Reference Guide*. Providence, RI: Dassault Systèmes, 2013.

[38] *Benchmarks Manual*. Providence, RI: Dassault Systèmes Simulia, 2012.

[39] F. Erdogan and G. C. Sih, “On the crack extension in plates under plane loading and transverse shear,” *J. Fluids Eng. Trans. ASME*, vol. 85, no. 4, pp. 519–525, 1963.

[40] Dönmez, S., Private Comunications

[41] F. Palacios *et al.*, “Stanford University Unstructured (SU2): Analysis and Design Technology for Turbulent Flows,” *52nd Aerosp. Sci. Meet.*, no. January, pp. 1–33, 2014.

[42] Kohnke, P. C., *ANSYS Theory Reference: Release 5.6*. ANSYS Incorporatedi 1999.

[43] L. Sun *et al.*, “Thermo-structural response caused by structure gap and gap design for solid rocket motor nozzles,” *Energies*, vol. 9, no. 6, 2016.

[44] S. Shi, J. Liang, F. Yi, and G. Fang, “Modeling of one-dimensional thermal response of silica-phenolic composites with volume ablation,” *J. Compos. Mater.*, vol. 47, no. 18, pp. 2219–2235, 2013.

[45] M. M. Hussaini and J. J. Korte, “Investigation of Low-Reynolds-Number Rocket Nozzle Design Using PNS-Based Optimization Procedure,” 1996.

[46] P. Isaksson, “On Crack Growth under Compressive Stresses On Crack Growth under Compressive Stresses,” Lulea University of Technology, 2001.

[47] N. P. Cannon, E. M. Schulson, T. R. Smith, and H. J. Frost, “Wing cracks a n d brittle compressive fracture,” vol. 38, no. 10, pp. 1955–1962, 1990.